Passive Acoustic Mapping For Cavitation-Mediated Drug Delivery Monitoring

Cameron Smith

Magdalen College

University of Oxford

Supervisor: Professor Constantin-C. Coussios

Thesis submitted for the degree of

Doctor of Philosophy

October 2021

Acknowledgements

This DPhil project would not be possible without the support and guidance of many people.

I gratefully acknowledge the Engineering and Physical Sciences Research Council (EPSRC) for funding me and this work.

I would like to thank my supervisor Professor Constantin Coussios, for giving me the opportunity to work in such a fantastic, prestigious laboratory. He is an excellent presenter and a passionate scientist, I am grateful for everything I have learned from him and for all the support and guidance he has given me over the years.

I would also like to thank Professor Eleanor Stride, Professor Robin Cleveland, and Professor Robert Carlisle, for always having their doors open to me and for their useful discussions and advice.

It has been a great honour to have had the opportunity to work with and alongside such a wide array of incredible people and scientists from such a diverse range of fields over the course of my time in the Biomedical Ultrasonics, Biotherapy, and Biopharmaceuticals Laboratory (BUBBL). I am very grateful to the whole of the BUBBL group for their help and kindness.

I would especially like to thank Dr. Luca Bau for all the help and guidance he has given me over the years, constantly encouraging me to be a better scientist. I'd also like to thank Alex Martin for always being an excellent soundboard for ideas, and who's humour always helped me over the highs and lows of the DPhil.

I would like to thank Dr. Christophoros Mannaris, Dr. Prateek Katti, Dr. Megan Jackson, and Sheena Wallington, for allowing me to utilise a vast dataset which took such a huge amount of time and effort to produce.

Additionally, I would like to thank Jim Fisk and David Salisbury in the workshop for assisting in the design, and the construction, of a wide range of equipment, always with good humour.

I have my parents to thank for always trying to raise me to be an inquisitive independent thinker. Their endless encouragement and support have made me who I am today.

Finally I am grateful to my wife Emily for her constant love and encouragement. Her humour and charm ever present to restore my sense of perspective.

Statement of Contributions

I gratefully acknowledge the following who contributed to this doctoral research.

Chapter 1

- Modifications to the PAM derivation were conducted in collaboration with Dr Luca Bau.
- The remainder of this section are entirely my own work except where explicitly cited otherwise.

Chapter 2

- Original data collection for the survival and gene expression studies were conducted by Dr Prateek Katti, Dr Christophoros Mannaris, Sheena Wallington, and Prof. Robert Carlisle for use as part of a separate study.
- Original data collection for the drug delivery study was conducted by Dr Megan Jackson and Dr Christophoros Mannaris for use as part of a separate study.
- Data amalgamation, sorting, cavitation data processing, and reprocessing study design was entirely my own work.
- Survival analysis was conducted in collaboration between myself and Dr Luca Bau.
- Statistical analysis of Nanostring data was conducted in collaboration with Dr Luca Bau.
- Manual exclusion was conducted by Dr Christophoros Mannaris while kept blind by myself, using software written by myself.
- Automated exclusion algorithm was created in collaboration between myself and Dr Luca Bau.

Chapter 3

- The results described in this section are entirely my own work.

Chapter 4

- The results described in this section are entirely my own work.

Chapter 5

- The results described in this section are entirely my own work.

Abstract

Advances in biomedical science have led to the development and clinical translation of novel potent anti-cancer agents, particularly antibodies and oncolytic viruses. However, many fail to translate to mainstream clinical use - not because they are incapable of triggering the desired biological response, but because they are unable to reach their target locations in the required concentrations to be effective. Bubbles excited by an acoustic field, also known as acoustic cavitation, have been used to aid the delivery of these biologically active materials.

Passive Acoustic Mapping (PAM) has recently been developed as a method of monitoring ultrasound-mediated drug delivery. However, while PAM has been used extensively in determining the location of cavitation activity, far less work has been done utilising PAM to quantify the spatially and temporally varying intensity of cavitation activity and relate that to a biological effect, with much of the previous work being conducted in the context of histotripsy.

This thesis has three main aims: demonstrating that PAM can be used quantitatively to allow for accurate monitoring of biological effects relating to the safety and efficacy of drug delivery in solid tumours; showing the utility of direct measurements of the cavitation activity by exploring how the relationship between cavitation and bioeffect is independent of how the cavitation is generated; and developing a novel form of the PAM algorithm that is capable of generating a universally reproducible measurement of cavitation energy.

In pursuit of the first aim a large *in vivo* dataset is utilised, and it is demonstrated that PAM is capable of quantitatively relating a metric of cavitation energy density called cavitation dose with the enhancement of drug delivery, up-regulation of genes associated with immune response, and improved survival outcomes in the context of cavitation enhanced drug delivery. In pursuit of the second aim it is shown that the cavitation dose metric can also be used to monitor cellular safety in the context of haemolysis, with the relationship between cavitation dose and haemolysis being found to be independent of the pressure, pulse length, and cavitation agent type and concentration used. Finally for the final aim a novel form of the PAM algorithm is developed, which is capable of generating universally reproducible measurements of cavitation energy with adequate spatial resolution, at a low computational cost.

Overall the work conducted as part of this thesis provides evidence that a set-up independent, energy-preserving metric of cavitation dose is possible, and that this

metric can be shown to be potentially predictive of both treatment safety and efficacy in the context of ultrasound-enhanced drug delivery and immunomodulation. It is hoped that this approach will inspire future researchers to investigate its applicability across the ever-growing range of therapeutic ultrasound applications ranging from transdermal drug delivery to opening the blood brain barrier.

Contents

"In the present paper we shall give an account of a preliminary survey of what appears to be a wide field for investigation, opened up by the study of the very surprising and remarkable effects obtained with sound-waves of high frequency and great intensity"

— Robert W. Wood and Alfred L. Loomis 1927
(Wood and Loomis 1927)

1

Introduction and Literature Review

Contents

1.1 Cancer

In 2017 over one in four deaths in England and Wales were due to cancer (UK 2018; National Statistics 2018). Cancer tumours form due to continual unregulated proliferation of the host's own cells. This loss of control of growth is the net result of accumulated abnormalities in multiple cell regulatory systems and reveal themselves in many abnormal types of cell behaviour (Cooper 2000). As cancerous cells grow uncontrollably, they spread so fast that the supply of nutrients is not able to keep up. This leads to tumours developing cores with little to no vascularization. Without blood vessels to support the cells they become dormant or die, leading to a core of dead or quiescent cells called a necrotic core (Cui 2006). As such regions deeper into the tumour are more hypoxic (Sorg et al. 2008), this hypoxia can lead to reduced drug effectiveness (Trédan et al. 2007).

Blood vessels within tumours grow abnormally compared to healthy vasculature. This can lead to the vessels becoming hyper-permeable "leaky" and tortuous (Dvorak et al. 1995; Azzi, Hebda, and Gavard 2013). This combined with the presence of very few to no functioning lymphatic vessels within the tumour (Leu et al. 2000) leads to a build-up in interstitial pressure, providing further barriers to the transport of oxygen, nutrients, and therapeutic agents to the tumour (Wu et al. 2014).

Tumours raise two unusual problems for standard drug therapy. Firstly, due to poor vascularisation, cancer cells are present at distances too far away from the nearest blood vessel for drugs to reliably reach them by diffusion alone (Jain 2009). Secondly, as cancer cells are a mutated form of the patient's own cells, creating a therapy that only affects cancer cells is incredibly challenging. Off target effects are the cause of many side effects in standard cancer therapies such as chemotherapy, often leading to a patient's refusal to undergo further treatment (Carey and Burish 1988; Palesh et al. 2018). These are both problems that can be overcome through the use of therapeutic ultrasound. Ultrasound when combined with cavitation agents can produce microstreaming which can drive drugs and other biological agents deeper into the tumour to improve their effectiveness (Carlisle et al. 2013). Ultrasound can also be highly localised to a target region, thereby giving spatial

specificity to otherwise non-targeted treatments (Stieger et al. 2007). As such, ultrasound therapy has the potential to improve the effectiveness of current cancer therapies. However, as ultrasound is a purely non-invasive technique, there can be difficulties in monitoring the therapy in real time. In an attempt to solve this problem, passive cavitation monitoring techniques were developed. These concepts are developed further in the following sections.

1.2 Ultrasound

Before discussing ultrasound therapy it is essential that the basics of linear acoustics are described. Perhaps the most fundamental concepts in acoustic theory are those of the acoustic wave, acoustic impedance, and attenuation. In this first section, these fundamental principles will be explored, as well as some of the consequences of these phenomena.

Sound can be defined as a wave of density perturbations that are small in amplitude in a compressible fluid, propagating away from an acoustic source (Landau and Lifshitz 1959). One of the most important properties of sound is perhaps the time it takes for a particle within the wave to complete a single oscillation, or the frequency/pitch of the sound. From this frequency, sound is broken down into three main categories. The first is the range of frequencies that are detectable to human hearing (20-20,000 Hz); sound within this range is referred to as sonic. Frequencies below 20 Hz fall into the category of infrasonic waves, and sound above 20 kHz are ultrasonic waves.

A sound wave in a fluid travels as a longitudinal wave (Landau and Lifshitz 1959), however in solids it can also travel as a transverse or shear wave (Hamilton, Blackstock, et al. 1998). The traditional linear wave equation can be incredibly powerful in describing both simple and complex acoustic wave propagation, and so it is valuable to begin an exploration of acoustics with the derivation of the linear wave equation.

The wave equation

In order to derive the linear wave equation (Lighthill and Lighthill 2001; Landau and Lifshitz 1959) we shall begin with perhaps the two most important equations in fluid dynamics, the Navier-Stokes momentum equation (Stokes 1880) and the continuity equation (Euler 1755).

$$\rho\left(\frac{\partial \mathbf{u}}{\partial t}+\mathbf{u}\cdot\nabla\mathbf{u}\right)=-\nabla p+\mu\nabla^2\mathbf{u}+\frac{1}{3}\mu\nabla(\nabla\cdot\mathbf{u})+\rho\mathbf{g} \tag{1.1}$$

$$\frac{\partial \rho}{\partial t}+\nabla\cdot(\rho\mathbf{u})=0 \tag{1.2}$$

We will assume that the medium is such that the viscosity and effect of gravity is negligible

$$\rho\left(\frac{\partial \mathbf{u}}{\partial t}+\mathbf{u}\cdot\nabla\mathbf{u}\right)=-\nabla p \tag{1.3}$$

We will also assume that the density, pressure, and particle velocity consist of a quiescent ambient quantity plus a perturbation that is assumed small. These perturbed quantities are the "acoustic" quantities.

density, pressure, and particle velocity are first order and that there is no bulk motion of the fluid:

$$p_{tot}=p_0+p \tag{1.4}$$

$$\rho=\rho_0+\rho' \tag{1.5}$$

$$\mathbf{u}=0+\mathbf{u}' \tag{1.6}$$

Which when combined with the continuity and Navier-Stokes equations gives us

$$\frac{\partial \rho'}{\partial t}+\mathbf{u}\cdot\nabla\rho'+\rho_0\nabla\cdot\mathbf{u}+\rho'\nabla\cdot\mathbf{u}=0 \tag{1.7}$$

$$\rho_0\left(\frac{\partial \mathbf{u}}{\partial t}+\mathbf{u}\cdot\nabla\mathbf{u}\right)+\rho'\left(\frac{\partial \mathbf{u}}{\partial t}+\mathbf{u}\cdot\nabla\mathbf{u}\right)=-\nabla p \tag{1.8}$$

These equations can then be simplified by assuming them to be first order (thereby assuming $\mathbf{u} << c$, $\rho' << \rho_0$, and $p << p_0$) these equations become

$$\frac{\partial \rho'}{\partial t}+\rho_0\nabla\cdot\mathbf{u}=0 \tag{1.9}$$

$$\rho_0 \frac{\partial \mathbf{u}}{\partial t} + \nabla p = 0 \tag{1.10}$$

By taking the partial derivative with respect to time of equation (1.9) and the divergence of equation (1.10) we end up with

$$\frac{\partial^2 \rho'}{\partial t^2} + \rho_0 \frac{\partial \nabla \cdot \mathbf{u}}{\partial t} = 0 \tag{1.11}$$

$$\rho_0 \nabla \cdot \left(\frac{\partial \mathbf{u}}{\partial t} \right) + \nabla^2 p = 0 \tag{1.12}$$

which can be combined to give

$$\nabla^2 p - \frac{\partial^2 \rho'}{\partial t^2} = 0 \tag{1.13}$$

In order to solve this equation we need a third relation. In order to obtain this we will look at the equation of state and state that the pressure is some function of entropy and density, and take the first order Taylor series expansion assuming $s = s_0 + s$

$$p_{tot} = p(\rho, s) = p_0 + \left(\frac{\partial p}{\partial \rho} \right)_{s,0} \rho' + \left(\frac{\partial p}{\partial s} \right)_{\rho,0} \breve{s} \tag{1.14}$$

We will now assume that the medium is lossless and adiabatic, giving

$$p_{tot} = p_0 + \left(\frac{\partial p}{\partial \rho} \right)_{s,0} \rho' \tag{1.15}$$

which when combined with equation (1.4) gives

$$p + p_0 = p_0 + \left(\frac{\partial p}{\partial \rho} \right)_{s,0} \rho' \tag{1.16}$$

$$p = \left(\frac{\partial p}{\partial \rho} \right)_{s,0} \rho' \tag{1.17}$$

by definition

$$\left(\frac{\partial p}{\partial \rho} \right)_{s,0} = c_0^2 \tag{1.18}$$

where c_0 corresponds to the speed of sound in the medium, this gives

$$p = c_0^2 \rho' \tag{1.19}$$

This can then be combined with equation (1.13) to give the wave equation

$$\nabla^2 p - \frac{1}{c_0^2} \frac{\partial^2 p}{\partial t^2} = 0 \tag{1.20}$$

Solving this equation for the special case of a plane wave gives the general solution comprising of a forwards propagating wave $h(t-x/c_0)$ and a backwards propagating wave $g(t+x/c_0)$

$$p = h(t - x/c_0) + g(t + x/c_0)\,. \tag{1.21}$$

it can be seen for a single frequency (f) wave, with wavelength λ and wavenumber ($k = 2\pi/\lambda$)propagating only in the forward direction we can have the solution

$$p = P_0 e^{j(\omega t - kx)} \tag{1.22}$$

which can be interpreted that if some oscillation is created at some plane creating an acoustic pressure amplitude P_0 then what results is a sinusoidal wave that oscillates over both time with an angular frequency ($\omega = 2\pi f$) and space with some distance ($\lambda = c_0/f$,$k = 2\pi/\lambda$).

Attenuation

Due to a variety of causes such as viscosity, acoustic scatterers, and relaxation, acoustic waves will often decrease in amplitude as they move through a medium. These effects are collectively referred to as attenuation. Attenuation can broadly be incorporated into the wave equation through the introduction of an imaginary term to the wavenumber

$$k = \beta - \alpha j \tag{1.23}$$

Which when substituted into the time harmonic solution to the wave equation (1.22) gives

$$p = P_0 e^{-\alpha x} e^{j(\omega t - \beta x)} = P_0 e^{-\alpha x} e^{j\omega(t - x/c_{ph})} \tag{1.24}$$

where c_{ph} is the phase speed of the wave given by

$$c_{ph} = \omega/\beta \tag{1.25}$$

Attenuation can be highly dependant on the frequency of the acoustic wave (table 1.1), with the frequency dependence of tissue in the frequency range used relevant to the applications described in this thesis corresponding to a $f^{1.1}$ dependence.

Table 1.1: Attenuation mechanisms and their frequency dependence (Blackstock n.d.) where f represents the frequency of the wave and f_r represents the relaxation frequency of the media

Mechanism	Frequency dependence of α
Viscosity	f^2
Heat conduction	f^2
Relaxation	$f^2/(f^2 + f_r^2)$
Boundary-layer effects	$\sqrt{f}$

1.3 Therapeutic ultrasound

Ultrasound has many advantages when utilized as a medical therapy. It is a truly non-invasive modality, not requiring any incisions through the skin of any kind to deliver its treatment, while also having the benefit of being entirely non-damaging in low doses (Williams et al. 1991; ter Haar 2002; Child et al. 1990). Ultrasound has been shown to be useful for a huge variety of therapies, exploiting either thermal or mechanical mechanisms.

When an ultrasound wave propagates through tissue, it becomes attenuated, in part due to scattering of the incident field, and in part due to viscous absorption. The absorptive component of attenuation effectively enables conversion of the mechanical energy carried by the ultrasound wave into heat, which can be exploited for therapy. Mild heating (hyperthermia) is capable of improving drug delivery to the heated tissues (Corry et al. 1982). Hyperthermia increases blood flow (Jain and Ward-Hartley 1984) and improves vascular permeability (Kong, Braun, and Dewhirst 2001), thereby allowing for improved distribution and effectiveness of the delivered drugs.

More intense heating can kill tissue, by a process known as thermal ablation. Thermal ablation is able to non-invasively destroy cancer tissue (Wu et al. 2004), reduce the risk of metastases (Kennedy 2005), and potentially create an antigen source to improve antitumour immunity (Den Brok et al. 2004), Ultrasound induced thermal ablation has even recently reached the stage of human clinical trials (Zhang and Wang 2010; Zhou, Syed Arbab, and Xu 2011).

There are also many non-thermal therapies that have been developed using ultrasound, from transdermal delivery of drugs (Bhatnagar et al. 2016) to improved penetration and distribution of biological agents (Arvanitis et al. 2011) to opening of the blood brain barrier (Hynynen et al. 2001). In non-thermal therapies the percentage of the time the ultrasound is applied for (also known as the duty cycle) is often kept low, doing so decreases the average acoustic intensity over time thereby ensuring a negligible build-up in temperature. Many of these therapies are predominantly caused by one mechanism, acoustic cavitation. In the following section, the bioeffects caused by cavitation will be put aside to allow for a thorough description of the physical nature of cavitation, the bioeffects caused by cavitation will then be explored in section 1.9.

1.4 Acoustic cavitation

In this work acoustic cavitation is defined as the response of a gas and/or vapour cavity to acoustic excitation. Historically there have been two possible methods for categorisation of acoustic cavitation activity. Firstly, a cavitation event can be categorised as being either stable or transient. In the case of stable cavitation a bubble oscillates around some equilibrium size (Neppiras 1980b). A key feature of stable cavitation is that after oscillating the bubble has broadly the same gas content as it did before cavitation occurred. As such, a bubble can continue to undergo stable cavitation for a prolonged period, oscillating for many cycles of acoustic pressure without being destroyed. In transient cavitation on the other hand, the gas within a bubble is either dissolved into the liquid or fragments into several smaller bubbles, causing cavitation activity to cease. Bubbles undergoing stable cavitation are capable of attracting and repelling each other through the secondary Bjerknes force (Bjerknes 1906; Bjerknes 1909; Mettin et al. 1997), potentially forming clusters of microbubbles which themselves exhibit a host of different properties to conventional microbubbles (Lazarus et al. 2017). The second method is by further categorising cavitation into inertial or non-inertial cavitation. In the following sections we define these terms and describe how cavitation is initiated in a practical setting.

1.4.1 Cavitation agents and nucleation

If a medium is exposed to a high enough pressure bubbles can be forced to form. This is known as cavitation nucleation and is split into two types. In homogenous cavitation nucleation, nucleation occurs spontaneously when the thermal energy is sufficient to vaporize a region of the liquid (Church 2002). In the case of heterogeneous cavitation nucleation, impurities within the medium provide the opportunity for gas bodies to stabilise and then grow, thereby making nucleation more probable (Maxwell et al. 2013). The pressures required for homogenous cavitation nucleation are far greater than those which have been found to be sufficient to form bubbles in vivo (Harvey et al. 1944). Heterogeneous cavitation nucleation is therefore the far more probable cause of cavitation nucleation in the body. However, cavitation nucleation in tissue still requires the application of high acoustic pressures, as such in order to enable predictable and sustained generation of cavitation activity at lower acoustic pressures for therapeutic applications, it is common practice to introduce artificial cavitation nuclei.

SonoVue and Definity are both commonly used commercial cavitation agents (Grayburn 2002). These cavitation agents are designed to be injected into the blood stream, thereby providing a contrast enhancing effect for ultrasound imaging. Both SonoVue and Definity belong to a category of cavitation agent commonly referred to as microbubbles. Microbubbles are gas spheres inside a liquid with a typical size of a few microns. Microbubbles often have shells between the gas and liquid phases to enhance the stability of the bubble. In the case of SonoVue and Definity these shells are comprised of phospholipids around a gaseous core comprising of Sulphur Hexafluoride and Perfluoropropane for SonoVue and Definity respectively (Grayburn 2002). The size of these microbubbles both lie in the range of $1 - 10\,\mu m$ with SonoVue having an average diameter of $2.5\,\mu m$ and Definity with a diameter of $1.5\,\mu m$ (Grayburn 2002). These diameters are chosen carefully, in order to ensure that the linear resonance of the bubble is close to 3.5 MHz, the most commonly used frequency for diagnostic ultrasound imaging.

1.4.2 Non-inertial cavitation

Non-inertial cavitation is a general term referring to all linear and non-linear oscillations exhibited by a bubble whose behaviour is dominated by the compressibility of the gas within. Microbubbles are highly non-linear oscillators (Lazarus et al. 2017; Plesset and Prosperetti 1977; Neppiras 1980a). When a bubble non-inertially oscillates in response to an ultrasound pulse of a single frequency, it begins to oscillate at integer multiples of the driving frequency. These are known as harmonic oscillations.

Non-inertial cavitation can also lead to the generation of emitted subharmonic signals. Subharmonic emission is what occurs when the signals emitted contain frequencies that are integer divisors of the driving frequency. This effect is mainly caused by three types of bubble behaviour. Firstly it is important to note that microbubbles inherently have a natural frequency at which they oscillate at the greatest magnitude (Leighton n.d.; Apfel and Holland 1991). This natural frequency is the result of a combination of the bubbles size, surface tension, and the properties of the gas contained within them, with smaller bubbles having a higher natural frequency. If a bubble is driven with a pressure wave whose frequency is a multiple of the bubble's natural frequency, the bubble can be found to oscillate at its natural frequency (Lauterborn 1976), this will be detected as a subharmonic signal. The second method is the theory that subharmonic waves propagate along the surface of the bubble, known as Faraday waves (Faraday 1831; Neppiras 1969), though the rapid fall-off in velocity potential of such modes would mean that this mechanism generates subharmonics detectable only very close to the bubble (Leighton n.d.).

Ultraharmonics are signals that are both integer multiples and integer divisors of the driving frequency. They occur when both effects causing subharmonic emission and effects causing harmonic emission occur simultaneously (Lauterborn 1976).

1.4.3 Inertial cavitation

Inertial cavitation occurs when the collapse of the bubble is driven primarily by the inertia of the surrounding inrushing fluid; the compressibility of the gas in

the bubble has minimal effect (Neppiras 1980b; Church and Carstensen 2001). Three criteria are commonly used to determine whether a bubble is undergoing inertial cavitation: (i) the bubble expands to at least 2.3 times its equilibrium radius (Blake 1948); (ii) the speed of the bubble wall exceeds the speed of sound during the collapse phase (Church 2002); (iii) the temperature at the core of the bubble exceeds 5,000 K (Apfel and Holland 1991). It is important to note that the collapse of the bubble during inertial cavitation does not necessarily lead to the destruction of the bubble. A bubble can undergo inertial cavitation repeatedly without changing its gas content, resulting in what is known as stable inertial cavitation (Church and Carstensen 2001). If a bubble collapses inertially in the presence of a boundary the collapse can occur asymmetrically. Sometimes the liquid rushes through the middle of the bubble, causing a liquid jet at the boundary surface (Benjamin and Ellis 1966), this process is known as jetting.

Inertial cavitation is capable of producing extreme pressures and temperatures within the local region of the bubble collapse (Apfel and Holland 1991). Given the inherent non-linearity of bubble dynamics, the onset of inertial cavitation is associated with a threshold acoustic driving pressure amplitude below which the bubble response is non-inertial (dominated by the compressibility of the gas) and above which the bubble collapse phase is dominated by the inertia of the surrounding fluid. This is called the inertial cavitation threshold pressure. This threshold is dependent upon the properties of the cavitation agent (Guo et al. 2013) and also the applied frequency of the sound wave, with lower frequencies leading to lower cavitation thresholds (Apfel and Holland 1991).

Inertial cavitation occurs over a very short timescale on the order of nanoseconds, during which a shockwave is emitted radially outwards from the bubble. The collapse is therefore associated with broadband acoustic emissions in the frequency domain, which are a unique indicator of inertial cavitation (Holt and Crum 1992). Furthermore, this transfer of acoustic energy from the fundamental frequency to a broad range of frequencies results in increased levels of attenuation, which is

capable of producing intense heating in a localised area (Holt and Roy 2001; Farny, Glynn Holt, and Roy 2010; Coussios et al. 2007).

Inertial cavitation is also capable of producing subharmonic emission if a bubble is unable to entirely collapse within a single period of oscillation. A bubble may begin its collapse and be interrupted by a rarefactional phase in the incoming sound wave, before finally collapsing entirely during the next compressional cycle. This can lead to the generation of signals occurring at integer divisors of the incoming acoustic wave, leading to the generation of subharmonics (Neppiras 1980a).

1.4.4 Microstreaming

Microstreaming is a result of stable cavitation behaviour that can be inertially or non-inertially driven. The repeated oscillations of a gas bubble cause the generation of streaming flows in an area around the bubble. These streams are capable of driving convection currents and producing shear stresses in a localised area (Tho, Manasseh, and Ioo 2007; Pereno et al. 2018). Velocities produced by microstreaming vary with the distance from the cavitating microbubble, with the highest recorded on the order of 1 mm/s (Pereno et al. 2018). The average wall shear stress produced by microstreaming is estimated to be on the order of 1 mPa (Pereno et al. 2018; Collis et al. 2010).

1.5 Cavitation Modelling

1.5.1 Non-linear bubble dynamics

Cavitation modelling is valuable both as a means of further understanding bubble dynamics but also to simulate cavitation data (as used in chapter 4). A common method for modelling the non-linear bubble dynamics is through the use of the Rayleigh-Plesset equation. In order to derive the Rayleigh-Plesset equation (Leighton n.d.) we shall begin once again with the Navier-Stokes momentum equation (Stokes 1880) and the continuity equation (Euler 1755).

$$\rho\left(\frac{\partial \mathbf{u}}{\partial t} + \mathbf{u}\cdot\nabla\mathbf{u}\right) = -\nabla p + \mu\nabla^2\mathbf{u} + \frac{1}{3}\mu\nabla(\nabla\cdot\mathbf{u}) + \rho\mathbf{g} \tag{1.26}$$

$$\frac{\partial \rho}{\partial t} + \nabla \cdot (\rho \mathbf{u}) = 0 \tag{1.27}$$

We will assume that the medium is incompressible and that the effect of gravity is negligible, thus simplifying the continuity equation to

$$\nabla \cdot \mathbf{u} = 0 \tag{1.28}$$

and the Navier-Stokes equation to

$$\rho \left(\frac{\partial \mathbf{u}}{\partial t} + \mathbf{u} \cdot \nabla \mathbf{u} \right) = -\nabla p + \mu \nabla^2 \mathbf{u} \tag{1.29}$$

If we assume spherical symmetry, this becomes

$$\rho \left(\frac{\partial u}{\partial t} + u \frac{\partial u}{\partial r} \right) = -\frac{\partial p}{\partial r} + \mu \nabla^2 u \tag{1.30}$$

Due to conservation of mass, the mass flux of the fluid in the radial direction must equal the mass flux caused at the bubble wall

$$\rho 4\pi r^2 u = \rho 4\pi R^2 \dot{R} \tag{1.31}$$

Where

$$\dot{R} = \frac{\partial R}{\partial t} \tag{1.32}$$

which can be rearranged to give

$$u = \frac{R^2}{r^2} \dot{R} \tag{1.33}$$

Which when plugged into equation (1.30) gives

$$\rho \left(\frac{2R\dot{R}^2}{r^2} + \frac{R^2}{r^2} \ddot{R} - \frac{2R^4}{r^5} \dot{R}^2 \right) = -\frac{\partial p}{\partial r} + 0 \tag{1.34}$$

Which can be rearranged to give the pressure at the bubble wall

$$\begin{aligned} p_L - p_\infty &= \int_R^\infty \rho \left(\frac{2R\dot{R}^2}{r^2} + \frac{R^2}{r^2} \ddot{R} - \frac{2R^4}{r^5} \dot{R}^2 \right) dr \\ &= \left[\rho \left(-\frac{2R\dot{R}^2}{r} - \frac{R^2}{r} \ddot{R} + \frac{R^4}{2r^4} \dot{R}^2 \right) \right]_R^\infty \\ &= \rho \left(R\ddot{R} + \frac{3}{2} \dot{R}^2 \right) \end{aligned} \tag{1.35}$$

This pressure at the bubble wall is less than the pressure inside the bubble (p_i) due to the presence of surface tension (σ). For a sphere at equilibrium

$$\pi R^2(p_i - p_L) = 2\pi R\sigma \tag{1.36}$$

Giving

$$p_L = p_i - \frac{2\sigma}{R} \tag{1.37}$$

If the sphere is not at equilibrium however it is also necessary to take into account the viscosity of the fluid. In spherical coordinates for an incompressible fluid the radial pressure (p_r) is related to the radial fluid velocity (u_r) by (Leighton n.d.; Lighthill and Lighthill 2001)

$$p_r = -p(r) + 2\eta\frac{\partial u}{\partial r} \tag{1.38}$$

Where η is the viscosity of the fluid. This radial pressure balances the liquid pressure at the bubble wall, thus

$$p_r = -p_L \tag{1.39}$$

This combined with equation (1.33) gives

$$p_L = p(r) + 4\eta\frac{R^2\dot{R}}{r^3} \tag{1.40}$$

Which when evaluated at the bubble wall $r = R$ this becomes

$$p(R) = p_L - 4\eta\frac{\dot{R}}{R} \tag{1.41}$$

This can be combined with equation (1.37) to give

$$p(R) = p_i - \frac{2\sigma}{R} - 4\eta\frac{\dot{R}}{R} \tag{1.42}$$

This pressure inside the bubble (p_i) is then comprised of the pressure of the gas (p_g) and the pressure caused by the vapour (p_v)

$$p_i = p_g + p_v \tag{1.43}$$

To estimate the p_g the assumption is commonly made that the gas follows a polytropic law of compression with a polytropic exponent κ ((Plesset and Prosperetti 1977))

$$p_g V(R)^{\kappa} = \text{constant} \tag{1.44}$$

At equilibrium p_L is equal to the hydrostatic pressure p_0, as such at equilibrium

$$p_g = p_0 + \frac{2\sigma}{R_0} - p_v \tag{1.45}$$

which gives us the general equation for p_g as

$$p_g = \left(p_0 + \frac{2\sigma}{R_0} - p_v\right)\left(\frac{R_0}{R}\right)^{3\kappa} \tag{1.46}$$

Which finally when combined with equations (1.42), (1.43), and (1.35) and setting $p_\infty = p_0 + p_f(t)$ where $p_a(t)$ is the pressure field driven far from the bubble gives an equation which Lauterborn (Lauterborn 1976) suggested should be referred to as the RPNNP equation to refer to the the main five workers who contributed to its formulation Rayleigh (Rayleigh 1917), Plesset (Plesset 1949), Noltingk (Noltingk and Neppiras 1950), Neppiras (Neppiras and Noltingk 1951), and Poritsky (Poritsky 1951), but is more commonly known as the Rayleigh-Plesset equation

$$R\ddot{R} + \frac{3}{2}\dot{R}^2 = \frac{1}{\rho}\left(\left(p_0 + \frac{2\sigma}{R_0} - p_v\right)\left(\frac{R_0}{R}\right)^{3\kappa} + p_v - \frac{2\sigma}{R} - \frac{4\eta\dot{R}}{R} - p_0 - p_f(t)\right) \tag{1.47}$$

1.5.2 Modelling radiated pressure

The Rayleigh-Plesset equation's assumption of incompressible fluid around the bubble can lead to large errors in the parameter ranges of interest to this text, which predominantly focus to 5 % duty cycle pulses of 0.5 MHz waves generating pressures around 1.75 MPa, as such we will further consider the Keller-Miksis equation (Keller and Miksis 1980; Johansen, Song, and Prentice 2017)

$$\left(1 - \frac{\dot{R}}{c}\right)R\ddot{R} + \left(\frac{3}{2} - \frac{\dot{R}}{2c}\right)\dot{R}^2 = \frac{1}{\rho}\left(1 + \frac{\dot{R}}{c}\right)p_w + \frac{R}{\rho c}\frac{dp_w}{dt} \tag{1.48}$$

where p_w is the pressure at the bubble wall given by

$$p_w = \left(p_0 + \frac{2\sigma}{R_0}\right)\left(\frac{R_0}{R}\right)^{3\kappa} - \frac{2\sigma}{R} - \frac{4\eta\dot{R}}{R} - p_0 - p_f(t) \tag{1.49}$$

The radiated pressure (p_{rad}) is given by

$$p_{rad} = \rho \frac{R^2 \ddot{R} + 2R\dot{R}^2}{r_l} \tag{1.50}$$

where r_l is the distance from the bubble center to the acoustic sensor. This will be utilized when conducting simulations in chapter 4.

The Keller-Miksis equation has proven to give a level of accuracy that allows it to broadly agree with acoustic measurements taken experimentally at parameter ranges similar to those of interest in this work (Collin and Coussios 2011; Johansen, Song, and Prentice 2017), while additionally being computationally simpler than some more accurate equations modelling bubble dynamics such as those of Gilmore (Gilmore 1952) or Marmottant (Marmottant et al. 2005), which are beyond the scope of this work.

1.6 Passive Cavitation Detection

As cavitation can be the cause of many useful biological effects, it is logical to consider the possibility that by monitoring the cavitation activity taking place, one would be able to monitor these biological effects. This idea led to the passive cavitation detector (PCD) (Madanshetty, Roy, and Apfel 1991). These are typically broadband ultrasound transducers, which are not used in the generation of a biological effect. Instead their function is to receive signals from some region of interest to monitor the ultrasound therapy. Broadband transducers are used as different cavitation behaviour can generate different types of acoustic signals; these differences are often clearest in the frequency domain.

Not only can these PCDs detect voltage levels to measure relative pressure amplitudes but their reception sensitivity can be calibrated to create absolute pressure measurements (Collin and Coussios 2011; Rich and Mast 2015b; Rich and Mast 2015a). These absolute pressure estimates are capable of measuring acoustic emissions generated by cavitation *in vitro*.

While PCDs enable detection of cavitation activity and may also enable its localization along the PCD transducer axis, they are unable to localize cavitation

activity anywhere outside that region. Additionally, PCDs are unable to determine the spatial distribution of acoustic sources within their region of measurement. To solve these problems, passive acoustic mapping (PAM) was developed.

1.7 Passive Acoustic Mapping

Passive Acoustic Mapping (PAM) is an acoustic imaging technique which uses an array of ultrasound transducers to receive signals from an area of interest which is being stimulated by another ultrasound source. There are several different versions of the PAM algorithm, which will be described in the following sub-sections.

1.7.1 Time Exposure Acoustics PAM

Time Exposure Acoustics (TEA) PAM is the original (Gyöngy and Coussios 2010b; Gyöngy et al. 2008) and simplest version of the PAM algorithm. Images detailing the acoustic energy within a region of interest are reconstructed by looking at the relative delays in time between a signal being received on one transducer and that same signal being received on all the others (Norton 2000). We shall now derive the TEA-PAM algorithm.

Ultimately we are attempting to relate the pressure we can measure using our array of ultrasound transducers ($p(\mathbf{x}_i, t)$) to the acoustic power density at some position of interest ($\Psi(\mathbf{x}', t)$). We will begin with the Navier-Stokes momentum equation and the continuity equation. In this derivation, t shall be used to represent time, $\mathbf{x}_i$ to represent a position in space at element (i) in three dimensional Cartesian space (x_i,y_i,z_i), $\mathbf{x}'$ to represent a position in space at the position of interest, i.e. the location at which we are attempting to estimate the power, in three dimensional Cartesian space (x,y,z), μ to represent the viscosity, $\mathbf{u}(\mathbf{x}_i, t)$ to represent the velocity of the fluid, ρ to represent the density of the fluid, and $\mathbf{g}$ to represent the acceleration due to gravity.

$$\rho\left(\frac{\partial \mathbf{u}}{\partial t} + \mathbf{u}\cdot\nabla\mathbf{u}\right) = -\nabla p + \mu\nabla^2\mathbf{u} + \frac{1}{3}\mu\nabla(\nabla\cdot\mathbf{u}) + \rho\mathbf{g} \tag{1.51}$$

$$\frac{\partial \rho}{\partial t} + \nabla\cdot(\rho\mathbf{u}) = 0 \tag{1.52}$$

It is assumed that the water is incompressible and has a constant density $\rho = \rho_w$. The continuity equation then becomes

$$\nabla \cdot \mathbf{u} = 0\,. \tag{1.53}$$

This, along with the assumption that the effects of gravity and viscosity on the velocity are negligible compared to the effect of pressure, simplifies the Navier-Stokes equation to

$$\rho_w \frac{\partial \mathbf{u}}{\partial t} = -\nabla p\,. \tag{1.54}$$

This gives us a description of the pressure at a location in terms of the fluid velocity at that location. If we assume this velocity is due to the flow of mass out of a theoretical sphere $\dot{m}(t)$, due to an acoustic source located at $\mathbf{x}_k$ and who's radius (r_k) stretches from this acoustic source we get

$$r_k = \sqrt{(x - x_k)^2 + (y - y_k)^2 + (z - z_k)^2} \tag{1.55}$$

This flow of mass out of our theoretical sphere is assumed to be constant across the surface of our sphere, as the pressure wave originating at the source is assumed to have angular symmetry. This means that the fluid velocity out of the sphere surface is the average mass flow across the surface area of the sphere.

$$u = \frac{\dot{m}}{4\pi r_k^2 \rho_w} \tag{1.56}$$

By substituting equation (1.56) into equation (1.54) and using our previous assumption that the flow out of our theoretical sphere is spherically symmetric. We get

$$\frac{\partial \dot{m}}{\partial t}\frac{1}{4\pi r^2} = -\frac{\partial p}{\partial r}\,, \tag{1.57}$$

which can then be integrated with respect to r between 0 and r_k to give

$$\frac{\partial \dot{m}}{\partial t}\frac{1}{4\pi r_k} = p\,. \tag{1.58}$$

The constant of integration is encapsulated in p which is the pressure relative to the equilibrium fluid pressure.

The flow of mass through our theoretical sphere is caused by movement of fluid at the acoustic source. In order to understand how, we must look at the wave equation (with c being the speed of sound in water)

$$c^2\nabla^2 p = \frac{\partial^2 p}{\partial t^2} \tag{1.59}$$

which for a spherically propagating field has the general solution

$$r_k p(r_k, t) = h(t - r_k/c) + g(t + r_k/c) \tag{1.60}$$

where h and g represent the forward and backward propagating waves respectively. In our case we are only concerned with waves propagating in the forwards direction and so we shall set $g = 0$. This gives

$$h(t - r_k/c)\frac{1}{r_k} = p \tag{1.61}$$

which we see is the same form as equation (1.58). The mass flow at the surface ($\dot{m}(t)$) is simply the mass flow at the acoustic source (represented by $\dot{q}(t)$ with a time delay due to the distance the wave has to travel. This gives

$$\frac{\partial \dot{m}(t)}{\partial t} = \frac{\partial \dot{q}(t - r_k/c)}{\partial t} = \ddot{q}(t - r_k/c)\,, \tag{1.62}$$

which can be substituted into equation (1.58) to give

$$\frac{\ddot{q}(t - r_k/c)}{4\pi r_k} = p(t)\,. \tag{1.63}$$

The acoustic power (ψ) can be calculated from the acoustic energy (E) as follows

$$\psi = \frac{dE}{dt} \tag{1.64}$$

where the energy given to a particle in a fluid is the force on that particle F multiplied by the displacement of that particle $\boldsymbol{\xi}$ due to that force in that instant

$$dE = \mathbf{F} \cdot d\boldsymbol{\xi} \tag{1.65}$$

which when combined with equation (1.64) becomes

$$\psi = \frac{\mathbf{F} \cdot d\boldsymbol{\xi}}{dt} = \mathbf{F} \cdot \mathbf{u}\,. \tag{1.66}$$

The only force acting in this instance is pressure and the flow is spherically symmetric giving

$$\psi = Apu \tag{1.67}$$

where A is the area over which the pressure is acting.

u can be defined relative to $\ddot{q}$ by combining equations (1.54) and (1.63) to give

$$\rho_w \frac{\partial u}{\partial t} = -\nabla \left(\frac{\ddot{q}(t - r_k/c)}{4\pi r_k} \right) \tag{1.68}$$

which when combined with the spherically symmetric flow assumption gives

$$\rho_w \frac{\partial u}{\partial t} = -\frac{\partial}{\partial r_k} \left(\frac{\ddot{q}(t - r_k/c)}{4\pi r_k} \right) = \frac{\ddot{q}(t - r_k/c)}{4\pi r_k^2} + \frac{\dddot{q}(t - r/c)}{4\pi r_k c} \tag{1.69}$$

where

$$\dddot{q}(t - r_k/c) = \frac{\partial \ddot{q}(t - r_k/c)}{\partial t} \,. \tag{1.70}$$

Equation (1.69) can be integrated and rearranged (assuming the initial velocity is zero to remove the constant of integration) to give

$$u = \frac{1}{4\pi \rho_w c r_k} \left(\ddot{q}(t - r/c) + \frac{c}{r_k} \dot{q}(t - r/c) \right) \,. \tag{1.71}$$

In the case where the source generates a flow with a constant frequency f and amplitude $\dot{q}_0$

$$\dot{q}(t - r/c) = \dot{q}_0 e^{j2\pi f(t - r_k/c)} \tag{1.72}$$

$$\ddot{q}(t - r/c) = 2\pi f j \dot{q}_0 e^{j2\pi f(t - r_k/c)} = 2\pi f j \dot{q}(t - r/c) \tag{1.73}$$

Thereby making the ratio of the magnitude of the first and second terms in equation (1.71)

$$\frac{c}{2\pi f r_k} \tag{1.74}$$

which in a standard scenario in which PAM is used within this work: conducted in tissues in which the speed of sound is approximately $c \approx 1500$, using a ultrasound

monitoring probe ($f \approx 5 \times 10^6$), at a distance in the range of 30-100 mm ($r_k \approx 70 \times 10^{-3}$) makes the ratio

$$\frac{c}{2\pi f r_k} << 1\,. \tag{1.75}$$

As such the second term in equation (1.71 can be ignored as for our purposes its value is negligible. This is the equivalent of making a plane wave assumption. This gives a simplified equation for u

$$u = \frac{1}{4\pi\rho_w c r_k}\ddot{q}(t - r/c) \tag{1.76}$$

which when combined with equation (1.67) using $A = 4\pi r_k^2$ and equation (1.63) to give

$$\psi_k(t) = \frac{\ddot{q}(t - r_k/c)^2}{4\pi\rho_w c} \tag{1.77}$$

Now we have determined the acoustic power originating from a single source, we would like to relate the pressure recorded at the acoustic sensor caused by the K point sources (p_{ik} to the power density distribution over a region of interest.

The true power density Ψ_T arises from a distribution of K point sources each with their own associated powers ψ_k and locations x_k

$$\Psi_T(\mathbf{x}', t) = \sum_{k=1}^{K} \psi_k \delta(\mathbf{x}' - \mathbf{x}_k) \tag{1.78}$$

where δ refers to the dirac delta function.

However, in reality when detecting this power density (Ψ_T) the measured power density will be affected by the point spread function of the detector $PSF(\mathbf{x}' - x)$, as such the measurable power density $\Psi(\mathbf{x}', t)$ becomes

$$\Psi(\mathbf{x}', t) = \int_{-\infty}^{\infty} \sum_{k=1}^{K} \psi_k(t)\delta(\mathbf{x} - \mathbf{x}_k)PSF(\mathbf{x}' - \mathbf{x})d\mathbf{x} = \sum_{k=1}^{K} \psi_k(t)PSF(\mathbf{x}' - \mathbf{x}_k) \tag{1.79}$$

which we can combine with equations 1.77 and 1.63 to give an equation relating the power density distribution to the pressure recorded at an acoustic sensor i (p_{ik}) at a radial position r_{ik}

$$\Psi_i(\mathbf{x}', t) = \frac{4\pi}{\rho_w c} \sum_{k=1}^{K} r_{ik}^2 p_{ik}^2 (t + r_{ik}/c) PSF(\mathbf{x}' - \mathbf{x}_k) \tag{1.80}$$

Now we come to creating an estimate for the power density distribution ($\tilde{\Psi}(\mathbf{x}', t)$) using these equations and the signals we detect using our array of acoustic pressure sensors s_i which are comprised of the combination of p_k and some white noise (v_i). The conversion between these pressures and the voltage received is determined by a constant ($\alpha_{if\mathbf{x}'_k}$) which is determined by the conversion from pressure to voltage for the element (i) at a specific frequency (f) and with a certain directional sensitivity as determined by the location of the acoustic source ($\mathbf{x}'_k$).

$$s_i(f) = v_i(f) + \sum_{k=1}^{K} \alpha_{if\mathbf{x}'_k} p_{ik}(f) \tag{1.81}$$

and can also be expressed in the time domain as

$$s_i(t) = v_i(t) + \sum_{k=1}^{K} \alpha_{i\mathbf{x}'_k} p_{ik}(t) \tag{1.82}$$

If implemented in the time domain the frequency components of the signal must be pre-estimated to reduce $\alpha_{if\mathbf{x}'}$ to $\alpha_{i\mathbf{x}'}$.

The estimation for the power density distribution is given by Gyöngy and Coussios 2010a as

$$\tilde{\psi}(\mathbf{x}', t) = \frac{4\pi}{\rho_w c} \sum_{i=1}^{N} \frac{w_i r_i^2(\mathbf{x}') s_i^2(t + r_i(\mathbf{x}')/c)}{\alpha_{if\mathbf{x}'}} \tag{1.83}$$

where w_i is the weighting given to that particular element out of N elements, in the TEA-PAM case $w_i = 1/N$.

Which can be obtained by taking the single source case of equation (1.82), combining it with equation (1.77), generalising it as true for all points in space for any number of acoustic sources, then treating each element as an independent estimate of the power density distribution.

This gives an average power ($\bar{\tilde{\psi}}$) over a time step (T) of

$$\bar{\tilde{\psi}}(\mathbf{x}') = \frac{1}{T} \int_{t_0}^{t_0+T} \tilde{\psi}(\mathbf{x}', t) dt \tag{1.84}$$

Equation (1.83) provides a similar form to combining equations (1.82) and (1.80), except that it is missing the PSF term. While this is of no consequence in the ability of TEA-PAM to localise cavitation activity, it changes the units of PAM to be in terms of power (ψ) rather than power density (Ψ), it also introduces a scaling factor error equal to the maximum amplitude of $PSF(x)$ as discussed further in chapter 4. For the remainder of this work PAM will be calculated using the equations as described in their original papers but will instead be given units of power density, thereby assuming that the PSF has no numerical consequence to remain consistent with the original formulations of the algorithms.

Equation (1.83) and (1.84) can be combined and converted into matrix form for easy computation

$$\mathbf{s}(\mathbf{x}', t) = \begin{bmatrix} s_1(t + r_1(\mathbf{x}')/c)/\alpha_{i\mathbf{x}'} \\ \vdots \\ s_N(t + r_N(\mathbf{x}')/c)/\alpha_{i\mathbf{x}'} \end{bmatrix} \tag{1.85}$$

$$\mathbf{R}_s(\mathbf{x}') = \int_{t_0}^{t_0+T} \mathbf{s}(\mathbf{x}', t)\mathbf{s}(\mathbf{x}', t)^+ dt \tag{1.86}$$

where + denotes "conjugate transpose"

$$\mathbf{D}(\mathbf{x}') = \text{diag}[r_1(\mathbf{x}'), ..., r_N(\mathbf{x}')] \tag{1.87}$$

$$\mathbf{w} = \begin{bmatrix} w_1 \\ \vdots \\ w_N \end{bmatrix} \tag{1.88}$$

$$\tilde{\tilde{\Psi}}(\mathbf{x}') = \frac{4\pi}{\rho_0 cT} \mathbf{w}^+ \mathbf{D}(\mathbf{x}')\mathbf{R}_s(\mathbf{x}')\mathbf{D}(\mathbf{x}')\mathbf{w}\,. \tag{1.89}$$

The time delays as shown in equation 1.85 can be implemented either in the time domain or in the frequency domain (Haworth et al. 2017). Doing so has predominantly three advantages. Firstly, an improvement in computation time can be achieved (Haworth et al. 2017), secondly it allows for convenient application of filters in the frequency domain, and thirdly it allows for a frequency dependant application of the $\alpha_{if\mathbf{x}'}$ term. If implemented in the time domain the frequency components of the signal must be pre-estimated to reduce $\alpha_{if\mathbf{x}'}$ to $\alpha_{i\mathbf{x}'}$ which can produce errors in energy estimation.

When implemented in the frequency domain equations 1.85 and 1.86 become:

$$\mathbf{s}(\mathbf{x}', f) = \begin{bmatrix} s_1(f)e^{j2\pi f r_1(\mathbf{x}')/c}/\alpha_{if\mathbf{x}'} \\ \vdots \\ s_N(f)e^{j2\pi f r_N(\mathbf{x}')/c}/\alpha_{if\mathbf{x}'} \end{bmatrix} \tag{1.90}$$

$$\mathbf{R}_s(\mathbf{x}') = \int_{f_1}^{f_2} \mathbf{s}(\mathbf{x}', f)\mathbf{s}(\mathbf{x}', f)^+ df \tag{1.91}$$

where the range f_1 to f_2 corresponds to the frequency band of interest.

The spatial resolution of TEA-PAM varies depending on the array aperture (D), the normal distance between the acoustic source and the array (z) and the wavelength (λ) of the source. The resolution is given by (Gyöngy and Coussios 2010a) to be

$$\Delta x_{-3\,dB} = 0.89(z/D)\lambda \tag{1.92}$$

$$\Delta z_{-3\,dB} = 6.95(z/D)^2\lambda \tag{1.93}$$

For a typical set-up an array similar to an L7-4 ($D = 38$ mm, $\lambda = 0.3$ mm) is used at a distance of $z = 70$ mm. This gives $\Delta x_{-3\,dB} = 0.5$ mm and $\Delta z_{-3\,dB} = 7.1$ mm. As can be seen, the axial resolution of TEA-PAM is on the order of half of a large mouse tumour, this combined with the large tail artefacts visible in TEA which can lead to associating cavitation where it in fact did not occur, thereby limiting TEA-PAM's use for monitoring therapies. For this reason, PAM was further developed to utilise the Robust Capon Beamforming (RCB) algorithm, a data adaptive beamforming method (Stoica, Wang, and Li 2003) with an improved spatial resolution (Coviello et al. 2015).

1.7.2 Capon Beamforming PAM

In Capon Beamforming (CB) PAM (J. Capon 1969; Lacoss 1971; Coviello et al. 2015) we choose different values of the weighting coefficients in an attempt to minimise the contribution of noise to our power estimate, as well as minimising the contributions caused by signals outside of the location of interest, all without distorting the signal that comes from the location of interest. This weighting coefficient is independently calculated for each spatial location, and is constant over the frequency band of interest. To do this, we start with our equation for the relationship between the

received signal and the pressure, equation (1.82), with equation (1.63) and assume that each of our acoustic elements are measurements of the same signal amplitude with some phase delay (ϕ_i) due to the angle the signal approaches the linear array.

$$\tilde{\hat{q}}(\mathbf{x}', f) = \sum_{i=1}^{N} w_i \hat{\hat{q}}(\mathbf{x}', f) e^{j\phi_i} = \hat{\hat{q}}(\mathbf{x}', f) \sum_{i=1}^{N} w_i e^{j\phi_i} \tag{1.94}$$

where

$$\hat{\hat{q}}(\mathbf{x}', f) = \frac{4\pi r_i(\mathbf{x}') s_i(t) e^{2\pi f r_i(\mathbf{x}')/c)}}{\alpha_{if\mathbf{x}'}} \tag{1.95}$$

or in matrix form

$$\tilde{\hat{q}}(\mathbf{x}', f) = \hat{\hat{q}}(\mathbf{x}', f) \mathbf{w}^{+} \mathbf{a} \tag{1.96}$$

Where

$$\mathbf{a} = \begin{bmatrix} e^{j\phi_1} \\ \vdots \\ e^{j\phi_N} \end{bmatrix} . \tag{1.97}$$

Ideally our estimation of the flow rate would be the same as the true flow rate $\tilde{\hat{q}} = \dot{q}$. This requires the constraint

$$\mathbf{w}^{+} \mathbf{a} = 1 . \tag{1.98}$$

In order to choose the optimum weights we seek to minimise the power subject to the constraint we just derived. This is done as the power we predict is in fact the sum of the power contributions from three sources. Firstly the power coming from acoustic sources located within the pixel we are trying to observe, which is the component we are attempting to isolate with our beamforming algorithm. Secondly the power coming from acoustic sources located outside of the pixel we are trying to observe, which we are attempting minimise. Lastly the power coming as white noise generated from a combination of sources including electrical noise, which we are also trying to minimise. As long as our constraint identified in equation (1.98) is met the power from the pixel of interest will have unity gain. This is untrue of the other sources of power, as such by choosing weighting coefficients that minimise the power, the unwanted signals are decreased without affecting the signal gain.

$$\min_{\mathbf{w}} \tilde{\tilde{\Psi}} \text{ subject to } \mathbf{w}^{+} \mathbf{a} = 1 \tag{1.99}$$

This minimisation can be done through the use of Lagrange multipliers (Lagrange 1761)

$$\mathcal{L} = \tilde{\tilde{\Psi}} - \lambda(\mathbf{w}^{+}\mathbf{a} - 1) = \mathbf{w}^{+}\mathbf{R}\mathbf{w} - \lambda(\mathbf{w}^{+}\mathbf{a} - 1) \tag{1.100}$$

where

$$\mathbf{R} = \frac{4\pi}{\rho_0 c}\mathbf{D}(\mathbf{x}')\mathbf{R}_s(\mathbf{x}')\mathbf{D}(\mathbf{x}')\,. \tag{1.101}$$

Using Lagrange multipliers the minimum of the power can be found at the stationary point for $\mathcal{L}$ with respect to λ and $\mathbf{w}$

$$\frac{\partial \mathcal{L}}{\partial \lambda} = -(\mathbf{w}^{+}\mathbf{a} - 1) = 0 \tag{1.102}$$

$$\frac{\partial \mathcal{L}}{\partial \mathbf{w}} = \mathbf{w}^{+}\mathbf{R} - \lambda\mathbf{a}^{+} = 0 \tag{1.103}$$

which gives

$$\mathbf{w}^{+} = \lambda\mathbf{a}^{+}\mathbf{R}^{-1} \tag{1.104}$$

which can then be substituted into equation (1.102) to give

$$\mathbf{w}^{+}\mathbf{a} = 1 = \lambda\mathbf{a}^{+}\mathbf{R}^{-1}\mathbf{a}^{+} \tag{1.105}$$

$$\lambda = \frac{1}{\mathbf{a}^{+}\mathbf{R}^{-1}\mathbf{a}} \tag{1.106}$$

which is then substituted into equation (1.104) to give

$$\mathbf{w}^{+} = \frac{\mathbf{a}^{+}\mathbf{R}^{-1}}{\mathbf{a}^{+}\mathbf{R}^{-1}\mathbf{a}} \tag{1.107}$$

as such the optimum weights can be found to be

$$\mathbf{w} = \frac{\mathbf{R}^{-1}\mathbf{a}}{\mathbf{a}^{+}\mathbf{R}^{-1}\mathbf{a}}\,. \tag{1.108}$$

1.7.3 Robust Capon Beamforming PAM

Capon beamforming has a major limitation when applied to real world signals. That it is assumed that we have perfect knowledge of the location of our region of interest relative to our array, and thus the value of our steering vector ($\mathbf{a} = \bar{\mathbf{a}}$), where $\bar{\mathbf{a}}$ is the assumed value of the steering vector. In reality however this is

rarely the case, there is always some uncertainty and this can manifest itself as the capon beamformer producing unreasonable estimates of the signals from acoustic sources (Coviello et al. 2015). In order to solve this problem the Robust Capon Beamformer (RCB) was developed (Stoica, Wang, and Li 2003)

Our derivation for the RCB-PAM algorithm will begin with the reformulation of the Capon beamformer algorithm as described in (Marzetta 1983). In which it was noted that equations (1.89), (1.101), and (1.108) Could be combined to create a power estimate that is not in terms of the weighting coefficients ($\mathbf{w}$), but instead of terms of the steering vector, which is independently calculated for each spatial location, and is constant over the frequency band of interest.

$$\tilde{\tilde{\Psi}} = \frac{(R^{-1}a)^{+}RR^{-1}a}{(a^{+}R^{-1}a)^{+}(a^{+}R^{-1}a)} = \frac{(a^{+}R^{-1}a)^{+}}{(a^{+}R^{-1}a)^{+}(a^{+}R^{-1}a)} = \frac{1}{a^{+}R^{-1}a} \tag{1.109}$$

Now we note that the signal covariance matrix (R) is comprised of the spectral density matrix for a linear array ($\Psi\mathbf{a}\mathbf{a}^{+}$) and the noise covariance matrix ($\mathbf{Q}$) which comprises of the white noise within the signal as well as the signal from all sources not within the location of interest (Marzetta 1983).

$$\mathbf{R} = \Psi\mathbf{a}\mathbf{a}^{+} + \mathbf{Q} \tag{1.110}$$

Which can be rearranged to give

$$\mathbf{Q} = \mathbf{R} - \Psi\mathbf{a}\mathbf{a}^{+} \tag{1.111}$$

then we claim that when $\tilde{\tilde{\Psi}}$ attains it's upper bound ($\tilde{\tilde{\Psi}}_{MAX}$) then $\mathbf{Q}$ is singular.

Therefore for some nonzero vector $\mathbf{d}$

$$(\mathbf{R} - \tilde{\tilde{\Psi}}_{MAX})\mathbf{d} = 0\mathbf{d} = 0 \tag{1.112}$$

giving

$$\mathbf{R}^{-1}\mathbf{a}\mathbf{a}^{+}\mathbf{d} = \frac{1}{\tilde{\tilde{\Psi}}_{MAX}}\mathbf{d}\,. \tag{1.113}$$

The vector $\mathbf{d}$ is an eigenvector of the matrix ($\mathbf{R}^{-1}\mathbf{a}\mathbf{a}^{+}$). There is only one nonzero eigenvalue of this matrix and has the corresponding eigenvector

$$\mathbf{d} = \mathbf{R}^{-1}\mathbf{a} \tag{1.114}$$

which when substituted into equation (1.113) gives

$$\tilde{\bar{\Psi}} = \frac{1}{\mathbf{a}^{+}\mathbf{R}^{-1}\mathbf{a}} \tag{1.115}$$

which is identical to the estimate given by the capon beamformer (1.109).

This means that the optimum power estimate is the upper bound on the range of solutions for an ill-posed maximum likelihood problem. With this in mind, the robust capon beamformer can be defined as adjusting the steering vector $\mathbf{a}$ to maximise the pressure estimate within some region of uncertainty of the steering vector

$$\min_{\mathbf{a}} \mathbf{a}^{+}\mathbf{R}(\mathbf{r}')^{-1}\mathbf{a} \,\text{subject to}\, \|\mathbf{a}-\bar{\mathbf{a}}\|^2 \leq \epsilon \tag{1.116}$$

which is equivalent to the following optimisation problem as it is more commonly posed

$$\min_{\mathbf{a}} \mathbf{a}^{+}\mathbf{R}(\mathbf{r}')^{-1}\mathbf{a} \,\text{subject to}\, \|\mathbf{a}-\bar{\mathbf{a}}\|^2 \leq \epsilon \tag{1.117}$$

in which we assume that

$$||\bar{\mathbf{a}}||^2 > \epsilon \tag{1.118}$$

to exclude the trivial solution $\mathbf{a} = \mathbf{0}$.

As the solution to equation (1.117) will always occur at the boundary of the constraint set, the problem can be simplified to

$$\min_{\mathbf{a}} \mathbf{a}^{+}\mathbf{R}(\mathbf{r}')^{-1}\mathbf{a} \,\text{subject to}\, \|\mathbf{a}-\bar{\mathbf{a}}\|^2 = \epsilon \tag{1.119}$$

Which can be solved using Lagrange multipliers

$$\mathcal{L} = \mathbf{a}^{+}\mathbf{R}^{-1}\mathbf{a} + \lambda(\|\mathbf{a}-\bar{\mathbf{a}}\|^2 - \epsilon) \tag{1.120}$$

$$\frac{\partial \mathcal{L}}{\partial \lambda} = \|\mathbf{a}-\bar{\mathbf{a}}\|^2 = 0 \tag{1.121}$$

$$\frac{\partial \mathcal{L}}{\partial \mathbf{a}} = \mathbf{R}^{-1}\mathbf{a} + \lambda(\mathbf{a}-\bar{\mathbf{a}}) = 0 \tag{1.122}$$

which can be rearranged to give

$$\mathbf{a} = \left(\frac{R^{-1}}{\lambda} + \mathbf{I}\right)^{-1} \bar{\mathbf{a}} = \bar{\mathbf{a}} - (\mathbf{I} + \lambda\mathbf{R})^{-1}\,\bar{\mathbf{a}} \tag{1.123}$$

where $\mathbf{I}$ is the identity matrix. This is then substituted into equation (1.121) giving

$$\epsilon = \|(\mathbf{I} + \lambda\mathbf{R})^{-1}\bar{\mathbf{a}}\|^2 \,. \tag{1.124}$$

The $M \times M$ covariance matrix is then split into its eigenvalues and eigenvectors

$$\mathbf{R} = \mathbf{U}\boldsymbol{\Gamma}\mathbf{U}^{+} \tag{1.125}$$

where

$$\boldsymbol{\Gamma} = \begin{bmatrix} \gamma_1 & 0 & \dots & 0 \\ 0 & \ddots & \ddots & \vdots \\ \vdots & \ddots & \ddots & 0 \\ 0 & \dots & 0 & \gamma_M \end{bmatrix} . \tag{1.126}$$

and a new vector is defined

$$\mathbf{z} = \mathbf{U}^{+}\bar{\mathbf{a}} \,. \tag{1.127}$$

These can now be combined with equation (1.124) to give an equation that can be used to find a unique value of lambda by (for example) Newton's method.

$$\epsilon = \sum_{m=1}^{M} \frac{|z_m|^2}{(1 + \lambda\gamma_m)^2} \tag{1.128}$$

Once a value of λ is ascertained, this can be used in equation (1.123) to get a value for the beam steering vector $\mathbf{a}$ which can then finally be used in equation (1.109) to get the estimate for the average power at that location.

1.8 Additional beamforming algorithms

In this review, focus is placed on passive beamforming algorithms that are capable of both localizing and quantifying the energy of acoustic sources that can be reasonably computed in or near real time with a dual-array set-up. Regrettably, this means not fully exploring a large number of other algorithms, some of which are briefly discussed in the remainder of this section.

1.8.1 Robust Beamforming by Linear Programming

The Robust Beamforming by Linear Programming (RLPB) algorithm is a data-adaptive beamforming algorithm that aims to improve interference suppression and mitigate calibration errors by utilizing higher-order statistics and making no prior assumption on the statistical distribution of the acoustical signals (Jiang et al. 2014; Lyka et al. 2018). This separates it from many other data-adaptive algorithms such as RCB which assumes that the recorded signals follow a Gaussian distribution, which is not necessarily true in the case of cavitation signals. By taking into account higher-order statistics the RLPB algorithm is capable of enhanced localization of cavitation signals than RCB or TEA (Lyka et al. 2018). However, the absence of unity (or near unity) gain restriction can lead to incorrect energy estimation, and taking account of the higher-order statistics leads to a significantly more computationally complex algorithm (in one reported case a 400 fold increase in computation time was observed (Lyka et al. 2018)).

1.8.2 Angular Spectrum

The computational speed of PAM has been shown to be capable of being significantly enhanced with what is known as the angular spectrum method (AS-PAM) (Arvanitis et al. 2017), which utilizes temporal and spatial frequency domain beamforming to generate 3D PAM maps in a highly computationally efficient way. With this algorithm, corrections can be applied for aberration correction in transcranial monitoring (Schoen and Arvanitis 2019), and stratified media (Schoen and Arvanitis 2020). The algorithm can be also used for real time control of the levels of cavitation generated (Patel, Schoen Jr, and Arvanitis 2018).

The angular spectrum passive acoustic mapping (AS-PAM) method substitutes the Helmholtz equation for the 2D fourier integral to relate the intensity of an acoustic field I between two different planes with a transfer function. As such the acoustic field on one plane ($z0$) can be used to estimate the field in other planes (z_1) parallel to it (equation 1.129). This allows the AS-PAM algorithm to determine the acoustic field on a line-by-line basis (for 2D reconstruction), or

a plane-by-plane basis (for 3D reconstruction), unlike other forms of the PAM algorithm that perform these calculations on a point-by-point basis. This can dramatically reduce the computation time compared to the other forms of the PAM algorithm described in this review.

$$I(x', y', z_1) = \sum_{\forall \omega} \left| FFT^{-1} \left(S_{z_0}(\omega) \cdot e^{i(z_1 - z_0)\sqrt{\left(\frac{\omega^2}{c^2}\right) - k_x^2 - k_y^2}} \right) \right| \tag{1.129}$$

Where S_{z_0} is the frequency domain representation (2D FFT) of the signal received by the array in the z_0 plane, and k is the wave number.

However, as the images in AS-PAM are generated via propagation of the received signals one of the consequences are that the energy estimates generated are affected by the focussing gain of the receiving array, which is spatially and frequency dependent as well as being unique for each specific array configuration. This can lead to errors in the energy estimates generated by AS-PAM. While theoretically these artefacts could be estimated by an appropriate simulation and corrected for, in practice for this to be accurately applied the frequency content of acoustic signals being imaged would need to be known before beamforming, which is problematic for real-time applications. In some applications the frequency content could be assumed before-hand with potentially acceptable levels of accuracy but it would remain a source of error. It is worth noting that while this artefact is a source of errors in regards to energy estimation its affect on energy localisation is negligible even if left uncorrected.

Now that the physical nature of cavitation and its detection mechanisms have been described, the bioeffects that cavitation can cause can now be explored in detail.

1.9 Cavitation bioeffects

Cavitation can produce beneficial bioeffects through a variety of mechanisms. In this review particular emphasis will be placed on bioeffects that occur during cavitation enhanced drug delivery therapies. The convection currents created by microstreaming patterns are capable of extravasating drugs and other biological

agents deeper into tissue than can be reached by simple diffusion (Carlisle et al. 2013; Bazan-Peregrino et al. 2012; Bazan-Peregrino et al. 2013; Arvanitis et al. 2011; Dimcevski et al. 2016). The shear stresses and jetting generated are also thought to be a potential mechanism in permeabilising cell membranes in a process known as sonoporation, forming temporary pores (Fan et al. 2012) allowing for improved distribution of biological agents into regions otherwise inaccessible such as through the blood brain barrier (Hersh et al. 2016). Cavitation is also capable of enhancing thrombolysis (Datta et al. 2006), destroying kidney stones (Chaussy et al. 2017), or homogenising cancerous tissue (also known as mechanical ablation) (Roberts et al. 2006). Cavitation is also capable of greatly enhancing local heating (Hynynen 1991; Clarke and Ter Haar 1997).

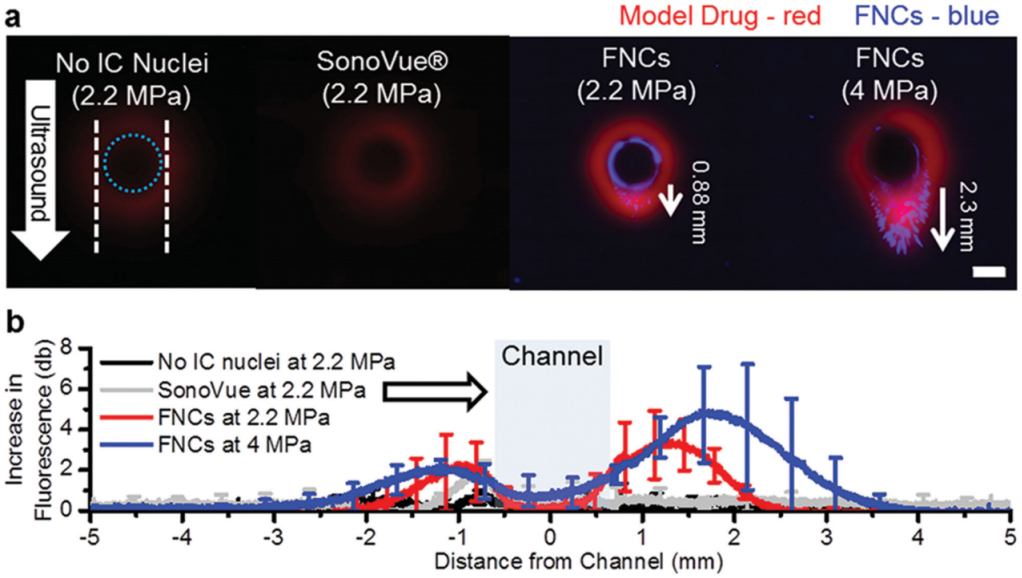

Figure 1.1: Nanocup penetration in a tissue model. a) Representative fluorescent images of the tissue model sliced radially to the channel after exposure to ultrasound for 5 minutes at 2.2 and 4.4 MPa. The white dotted lines indicate the edges of the ultrasound focus, and the dotted blue line represents the edge of the flow vessel. A white arrow demarcates the direction of ultrasound. In the images, the model drug (TRITCD) is labelled in red and the nanocups are labelled in blue (FNCs). The scale bar represents 1 mm, and is valid for all images. b) Average increase in fluorescence intensity profile plots of no cavitation nuclei, SonoVue, and nanocups at both 2.2 MPa and 4 MPa taken down the centre line and in the direction of ultrasound are shown for each test condition. The white arrow indicates the direction of ultrasound and the blue box represents the flow channel. TRITCD without cavitation nuclei and without ultrasound exposure was used as the reference value. For clarity, only 20 to 25 points are shown with standard deviations (Kwan et al. 2015b). (used with permission)

Of particular focus in this report is the ability of cavitation to enhance drug delivery. Both microbubbles (Dimcevski et al. 2016), and nanocups (Kwan et al. 2015b) have been used as cavitation nuclei to enhance the delivery of a wide variety of biological agents. Oncolytic viruses (Myers et al. 2016), liposomes containing drugs (Graham et al. 2014), and Antibodies (Khaibullina et al. 2008) have all been shown to have improved delivery when combined with ultrasound and cavitation agents. Ultrasound-enhanced extravasation distances have been shown to be as high as 2.3 mm for oncolytic viruses *in vitro* (Bazan-Peregrino et al. 2013; Kwan et al. 2015b) (figure 1.1), with a tenfold increase in therapeutic efficacy (Bazan-Peregrino et al. 2012). Levels of extravasation in ultrasound-enhanced delivery are dependent upon the particle density (Mo et al. 2015; Lea-Banks et al. 2016), with oncolytic viruses bound to gold extravasating 4 to 6 mm *in vitro* (Mo et al. 2015), a three fold increase on their unbound counterparts. While these extravasation depths are likely not representative of the distances travelled *in vivo*, they are still indicative of the enhanced distribution achieved when utilising ultrasound and cavitation agents.

Centre frequency (MHz)	Peak negative pressure (kPa)	Pulse length (cycles)	Pulse repetition frequency (Hz)	Duty cycle (%)	Exposure duration (s)	Source
0.5	360-2400	3250	10	6.5	300	(Bazan-Peregrino et al. 2012)
0.5	1500	-	0.5	-	120	(Kwan et al. 2015b)
2	4000	-	-	-	300	(Kwan et al. 2015b)
1.9	270	4	1425	0.3	1890	(Dimcevski et al. 2016)
0.5	1500	5000	0.5	0.5	840	(Myers et al. 2016)
0.5	0-1250	833-3320	10	1.7-6.6	10	(Mo et al. 2015)
0.5	0-3500	12.5-50,000	5-100	10-2000	10	(Arvanitis et al. 2011)
0.5	0-1200	25-50,000	0.05-3.3	0.33-50	1.6-240	(Choi et al. 2014)

Table 1.2: Summary of the ultrasound parameters used in a variety of ultrasound mediated drug delivery studies.

A wide variety of ultrasound parameters have been used to achieve enhanced drug delivery both *in vitro* and *in vivo*. However parameters that frequently have been shown to be effective are therapeutic pulses on the order of 0.5 MHz centre frequency, 0 to 2 MPa peak negative pressure, 0.5 to 100 ms pulse lengths, 0.5 to 50 Hz PRF, for a total duration of 10 to 300 seconds (Table 1.2).

These bioeffects can be indirectly monitored by using cavitation detection techniques. PCDs can predict safe and effective opening of the blood brain barrier (Arvanitis et al. 2012; O'Reilly and Hynynen 2012; Tsai et al. 2016). PAM has been used to co-localise cavitation behaviour and drug delivery *in vivo*, provide a qualitative estimate of the extent of drug delivery (Choi et al. 2014), and act as a measure of the persistence of cavitation within a target volume (Kwan et al. 2015b). PAM can be expanded to 3D to monitor blood brain barrier opening through the use of hemispherical arrays (Jones, O'Reilly, and Hynynen 2013; Crake et al. 2018). However, PAM has yet to be used to quantitatively monitor cellular safety, or as a quantitative measure for the efficacy of extravasation.

While cavitation can produce these beneficial bioeffects it can have a range of important safety concerns. The large quantities of power involved during bubble collapse in inertial cavitation is capable of causing damage to the surrounding endothelial layer (Miller 2007; Chen et al. 2010), this is done primarily by vessel distention (motion outwards against surrounding tissue), vessel invagination (motion inwards towards the lumen), and jetting, with invagination being a more prominent effect than distention (Chen et al. 2011a). Historically jetting was studied as the hammer of liquid pushing through the centre of the bubble was capable of causing damage to ship propellers (Blake and Gibson 1987). In the presence of a rigid flat surface jetting will occur towards the surface. Jetting is also known to occur within microvessels (Chen et al. 2011b) and is proposed as a mechanism for microbubble-enhanced vascular permeability and/or vascular damage (Caskey et al. 2007). Near a compliant flat boundary jetting can be toward or away from the boundary, depending on the mechanical properties of the boundary, bubble size and distance from the boundary (Brujan 2000; Chen et al. 2011b; Chen et al. 2011a).

The safety of cavitation based therapies has also been investigated by many groups in an attempt to identify a range of ultrasound parameters below which it is safe to operate. Table 1.3 contains a collation of parameters that were the lowest parameters used which generated cell damage above the noise floor in the respective

studies. As can be seen, the range between parameters suitable for cavitation-enhanced drug delivery without causing damage is narrow. This combined with the stochastic nature of cavitation shows the potential for techniques that could monitor the safety and efficacy of these treatments to allow for the reliable delivery of a known “cavitation dose" to strike an optimal compromise.

Centre frequency (MHz)	Peak negative pressure (kPa)	Pulse length (cycles)	Pulse repetition frequency (Hz)	Duty cycle (%)	Exposure duration (s)	Source
1.13	3350	500	5	0.2	60	(Hwang et al. 2005)
1.155	3350	19.5	500	0.8	30	(Chen et al. 2003a)
1.5	600	100	10	0.07	60	(Samiotaki et al. 2012)
1.17	1000	500	1	0.04	120	(Hwang et al. 2006)
2.25	1000	46	100	0.2	1	(Samuel et al. 2009)
1	2800	100	20	0.2	60	(Everbach et al. 1997)

Table 1.3: Summary of the lowest ultrasound parameters at which cell damage occurred in a variety of studies.

In an attempt to monitor the safety of cavitation based therapies PCDs have been used. The power density of broadband emission has been used to quantity the inertial cavitation dose (Chen et al. 2003a). This inertial cavitation dose has been shown to correlate with biological activity, such as haemolysis (Chen et al. 2003a; Everbach et al. 1997) and endothelial cell damage (Hwang et al. 2006; Hwang et al. 2005). These studies show the potential of passive cavitation detection techniques to monitor ultrasound therapies in real time.

Recently, PAM has also been proposed as a tool for identifying regions of liquefaction after histotripsy (Bader et al. 2017) in a tissue phantom. Following on from the commencement of the work presented in this thesis (Smith and Coussios 2019), further work has been done in this area. PAM has been shown to quantitatively correlate with haemolysis (Jahanpanah et al. 2019), and clot degredation using histotripsy pulses (Hendley et al. 2021), the results of the former showing agreement with the results presented in chapter 3 of this work. 3D PAM has been used to predict the volume of tissue damage during nonthermal brain ablation (Jones, McMahon, and Hynynen 2020).

1.10 Implications for the present work

Ultrasound induced cavitation has been shown to be the cause of a large number of beneficial and adverse bioeffects. RCB-PAM has proven to be effective at determining the location where cavitation has taken place both *in vitro* (Coviello et al. 2015) and *in vivo* (Choi et al. 2014; Crake et al. 2016). However, while PAM is capable of creating an estimate of the cavitation energy at acoustic source (Gray, Lyka, and Coussios 2018), and the strength of cavitation has been shown to correlate with biological effects (Hwang et al. 2006; Chen et al. 2003a), there have been no published attempts to date to correlate the magnitude and extent of the PAM signal detected during drug delivery to the extent of extravasation and to the degree of cellular or vascular damage in the context of cavitation enhanced drug delivery. In this project quantitative set-up independent measures of spatially localised cavitation dose will be related to the safety and efficacy of ultrasound-enhanced drug delivery with the aim of developing control algorithms to deliver optimised ultrasound therapies.

2

PAM Monitoring of Cavitation-Enhanced Immunotherapy

Contents

2.1 Introduction

This section represents an initial investigation as to whether spatio-temporal quantification of cavitation activity through PAM can provide a useful monitoring tool for cavitation-enhanced drug delivery, in particular exploring its ability to monitor the effectiveness of cavitation-enhanced antibody delivery for immunotherapy. In order to do this, this chapter utilises a large body of inherited data from three separate experimental studies, all of which fundamentally use the same experimental set-up. The first two of these studies were conducted by Dr Prateek Katti and Dr Christophoros Mannaris (Katti 2020) , augmented by their unpublished pilot data, and the third study was conducted by Dr Megan Jackson and Dr Christophoros Mannaris utilising previously unpublished data. The basic experimental set-up is therefore described as used in all of these experiments in the following section, as well as any differences between experimental methodologies. These studies were originally conducted exploring the enhanced efficacy caused by the presence or absence of a delivered ultrasound treatment. The data collation, PAM generation and processing, and the statistical analysis were conducted by myself with assistance from Dr Luca Bau as detailed in the Statement of Contributions section. The result of this is the availability of a large dataset with cavitation information from PAM with quantified survival, immune response, and drug delivery. Here we post-analyse this dataset to explore what PAM can tell us quantitatively. We explore whether a relationship can be found between the measured cavitation and a variety of metrics of treatment efficacy.

2.2 Experimental set-up

2.2.1 Animals

Survival and nanostring studies

UK Home Office guidelines and the UKCCCR Guidelines for the Welfare of Animals in Experimental Neoplasia were followed. CT-26 cells ($4x10^6$ cells in 100 μL RPMI 1640) were subcutaneously injected into the flanks of BALB/c female mice

(Charles River) using a 25-gauge needle. The mice were then randomized into treatment groups.

Drug delivery study

UK Home Office guidelines and the UKCCCR Guidelines for the Welfare of Animals in Experimental Neoplasia were followed. HT-29 cells (4x10^6 cells in 100 μL DMEM) were subcutaneously injected into both flanks of CD-1 nude female mice (Charles River) using a 25-gauge needle and then randomized into treatment groups.

2.2.2 Ultrasound set-up

In all studies a dual transducer set-up with two co-planar linear arrays was designed and built in-house (Figure 2.1). It served as the core hardware of inducing and recording cavitation events during the therapy. Two 0.5 MHz focussed transducers (H-107 D SN12; Sonic Concepts, Bothell, WA, USA) with active diameter 64 mm, focal length 62.6 mm, and 45 by 18-mm rectangular cut-out were used. The combined focus of the two transducers leads to a significantly reduced beam size with axial, lateral, and elevational dimensions of 6.0, 1.4, and 3.2 mm respectively. This reduced beam size allows for more precise treatment of the target volume. Cavitation was recorded using two perpendicular and co-planar L11-5v linear arrays (L11-5v, Verasonics, Kirkland, WA, USA) that were placed within the rectangular cutouts of the two 0.5 MHz transducers. Cavitation data was collected using a Verasonics Vantage Research Ultrasound System (Vantage 256, Verasonics, Kirkland, WA, USA), and were transferred to a computer for post-processing.

The survival study comprises of a combination of experimental data (Katti 2020), to which unpublished pilot data obtained by applying the same protocol with lower acoustic pressures were added to better sample the cavitation space. In the survival study all mice were treated twice, 5 days apart, with 50 μL of SonoTran Particles (SPs), a gas-stabilizing, cup-shaped sub-micron solid particles, which cavitate purely inertially and can support sustained cavitation activity for tens of minutes (Kwan et al. 2015b; Kwan et al. 2015a)(OxSonics Therapeutics, Oxford,

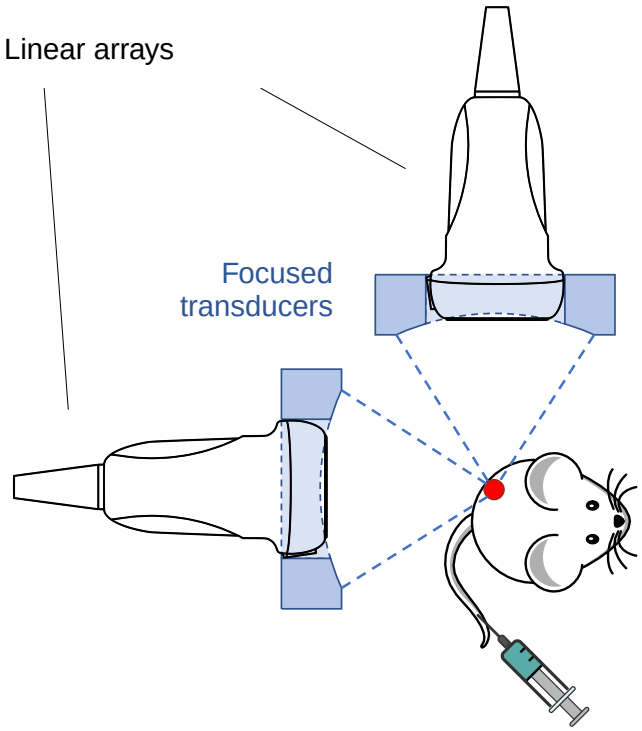

Figure 2.1: Experimental set-up of the single sample blood holder experiment. Two L11-5v linear arrays at 90 degrees to each other provide improved PAM resolution while a mouse receiving and IV injection of SPs and monoclonal antibodies is exposed to therapeutic ultrasound.

UK), at a concentration of 17.5 mg/ml and 50 μL of one of three monoclonal antibodies (rat IgGκ 2, rat antimouse anti-PDL1, rat antimouse anti-PD1), and immediately subjected to either ultrasound or a sham treatment. The ultrasound treatment comprised of 10 minutes of 0.5 MHz ultrasound pulses of 50,000 cycles with a 0.5 Hz pulse repetition frequency, leading to a 5 % duty cycle. A range of pressures from 1.5 to 2.25 MPa peak negative were used (table 2.1). Between each sonication pulse B-mode imaging was conducted. This provided real-time feedback on the alignment between the tumour and the focus. The user could then move the mouse (which was connected onto a 3-axis positioning system) keeping the ultrasound focus within the tumour, covering the entire tumour volume twice within the 10-minute treatment exposure.

In the case of the gene expression study only one treatment was conducted with

Table 2.1: Ultrasound parameters used

Parameter	Value
Centre frequency	0.5 MHz
Duration	10 minutes
PRF	0.5 Hz
Number of cycles	50,000
Duty cycle	5%
Pressure	1.5 - 2.25 MPa

only the IgG and anti-PDL1 groups, with the mice sacrificed either 24 hours or 5 days post treatment.

In the case of the drug delivery study only one treatment was conducted. Mice were split into one of three groups, one group received a 50 μL injection SPs at a concentration of 17.5 mg/ml, another group received 50 μL injection of SPs at a concentration of 8.75 mg/ml, and the third group received no SPs. All groups received an intravenous injection of 60 μL of Cetuximab antibody (0.3 mg). Mice were sacrificed immediately after US treatment and tumours were harvested, weighed, and frozen at -80 °C until further analysis.

2.2.3 Signal processing

The processing of the cavitation signals was conducted using the frequency-domain RCB-PAM algorithm as described in the previous chapter over a 15 mm square region of interest with a resolution of 0.4 mm square and using $\epsilon = 5$ in the range 3-10 MHz. Electrical impedance was used in place of the acoustic impedance in the PAM algorithm giving a final unit in terms of electrical power density rather than acoustic power density. Due to the use of co-planar linear arrays to generate the power density maps, the PAM algorithm can only have resolution within 2D space. As such an assumption has to be made regarding the cavitation distribution across the elevational dimension. In this work it is assumed that all of the cavitation occurred within the volume in which the elevational sensitivity of the element is

approximately equal to its maximum. As such the PAM map is the 2D projection of the 3D power density, thereby becoming a 2D power density.

In order to estimate the average cavitation energy experienced by the tumour a new metric was derived. The cavitation power density estimated by PAM (Equation 1.103) is integrated across the duration of the treatment and across the 2D volume measured within the PAM image to give the total cavitation energy. This is then divided by the total treatment volume (figure 2.2). This provides an estimate of the average energy experienced by the treatment volume, referred to hereafter as the "cavitation dose".

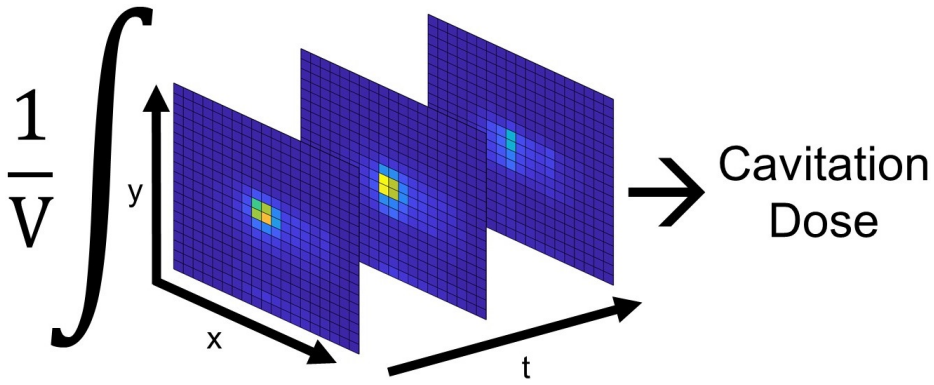

Figure 2.2: The cavitation dose for each treatment was calculated as the integral of the PAM power maps over the exposure duration and the measured volume within the eppendorf, comprising of the area of the cross section of the eppendorf and the elevational FWHM of the linear arrays. This was then normalized by the total treated volume (in this case the volume of the blood).

2.2.4 Statistical analysis

All statistical analysis as performed using R version 4.0.0. Correlations were calculated as Spearman's ρ and tested for significance using the AS 89 algorithm (*cor.test* function of the stats package, version 4.0.0). Differences in mean cavitation between different RECIST categories were tested using Welch's t test.

Hazard ratios were modelled using an additive Cox model (Cox 1972) (family cox.ph in the mgcv package, version 1.8-36) with cavitation dose and initial volumes modelled as penalized cubic regression splines with shrinkage (Wood 2017) with 4 knots evenly spaced throughout the (ordered) covariate values. Clustering of mice

by study (Katti 2020, pilot 1 or pilot 2) was accounted for by including study as a random intercept. Confidence intervals for the hazard ratio were calculated from the standard errors obtained from the Bayesian posterior variance-covariance matrix after adjusting for smoothness parameter selection. The analysis was performed separately for different treatment groups. All p values are two-sided and deemed significant at the 0.05 level.

2.2.5 Gene expression analysis

Raw Nanostring counts below the background threshold (geometric mean of negative controls) were set to the threshold and excluded from normalisation. Positive normalisation (using the geometric mean of positive controls) was applied to account for technical variation, followed by mRNA content normalisation with housekeeping genes selected using the geNorm algorithm (*Eef1g*, *Tubb5*, *Sf3a3*, *Sap130* for t=5d and *Rpl19*, *Abcf1*, *Eef1g*, *Hprt* for t=24hrs). Genes with raw counts below background in more than 20% of samples were filtered out and normalised counts were log2-transformed for downstream analysis. A linear model with the interaction of drug and timepoint, and the interaction of drug, timepoint and cavitation dose as covariates was fitted to the normalised data using limma-trend (limma package, version 3.46.0), and empirical Bayes moderated t-statistic was used for statistical tests of differential gene expression. Differentially expressed genes were defined as $p < 0.05$ and log2 fold change/nJ > 0.2 and these definitions were used in the Venn diagram. All p values were adjusted to control for the false discovery rate with the Benjamini-Hochberg method.

2.2.6 Drug delivery quantification

Levels of Cetuximab (ng/tumour) were quantified by ELISA. Tumours were kept on ice and homogenized in lysis buffer (catalogue number E3971, Promega) at a final concentration of 100 mg/ml. High binding 96-well plates (catalogue number 655061, Greiner Bio-One) were coated with 50 μL of Goat Anti-human IgG (catalogue number A9544, Sigma Aldrich) at the concentration of 1.2 $\mu g/mL$ and then

incubated overnight at 4 before use. The following day wells were washed three times with PBS-0.05 % Tween-20 (wash buffer) and blocked with 200 μL of 1 % Bovine Serum Albumin in PBS (blocking solution) for 1 hour at room temperature. Tumour homogenates were further diluted to 1.25 mg/ml in blocking solution, and a standard curve was prepared by spiking Cetuximab into an aliquot of untreated control tumour (2-fold serial dilutions starting from a concentration of 80 ng/ml). The plate was then washed three times and both samples and standards were then added to the wells (50 $\mu L/well$) and incubated at room temperature for 2 hours. After this time, another 3 washes were performed before incubation with 50 µL/well (1 $\mu g/mL$) of detection antibody (Anti-human IgG-HRP, catalogue number W4031, Promega) for 2 hours at room temperature. After a final wash, 100 μL of TMB substrate was used to develop the assay (incubation for 5-10 minutes at room temperature) and the reaction was then stopped with 1 M sulphuric acid. Optical densities were read at a wavelength of 450 nm using a Fluostar Omega plate reader (BMG Labtech) and drug concentrations calculated using MARS software (BMG labtech) with a 4-parameter logistic regression analysis. Cetuximab delivery was quantified as ng/mg of tumour.

2.3 Variability in delivered cavitation dose

The variability of cavitation dose within treatment protocols was assessed by looking at its range, which is arguably the most relevant measure of variation when each individual outcome matters. The cavitation dose was found to be highly variable between mice for all protocols, with a range of 0.45-4.75 nJ/mm^3 (median 2.5 nJ/mm^3, interquartile range (IQR) 1.9-3.3 nJ/mm^3) for the published treatments, 0.19-1.4 nJ/mm^3 (median 0.50 nJ/mm^3, IQR 0.38-0.76 nJ/mm^3) for pilot 1 and 0.12-4.5 nJ/mm^3 (median 0.88 nJ/mm^3, IQR 0.68-1.5 nJ/mm^3) for pilot 2 (figure 2.3). This demonstrates that although all the mice within the same groups were given the same cavitation treatment protocol, a large variation was present in the amount of cavitation energy received.

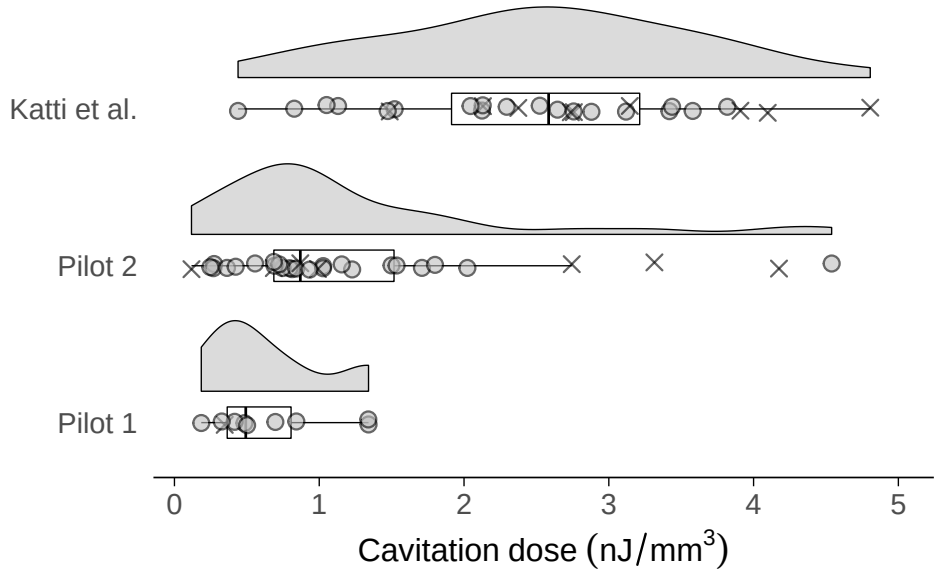

Figure 2.3: Distribution of cavitation doses split by treatment protocol. Box-plots show the median (middle line), lower and upper quartiles (box) and 1.5 times the interquartile range (whiskers) with crosses relating to censored mice and circles uncensored.

In order to better understand the sources of variation in the tumour outcomes, the spatial and temporal distribution of cavitation within individual subjects were examined. Inspection of the cavitation dose at each pulse within a treatment (figure 2.4) reveals a highly heterogeneous cavitation response both in space and in time.

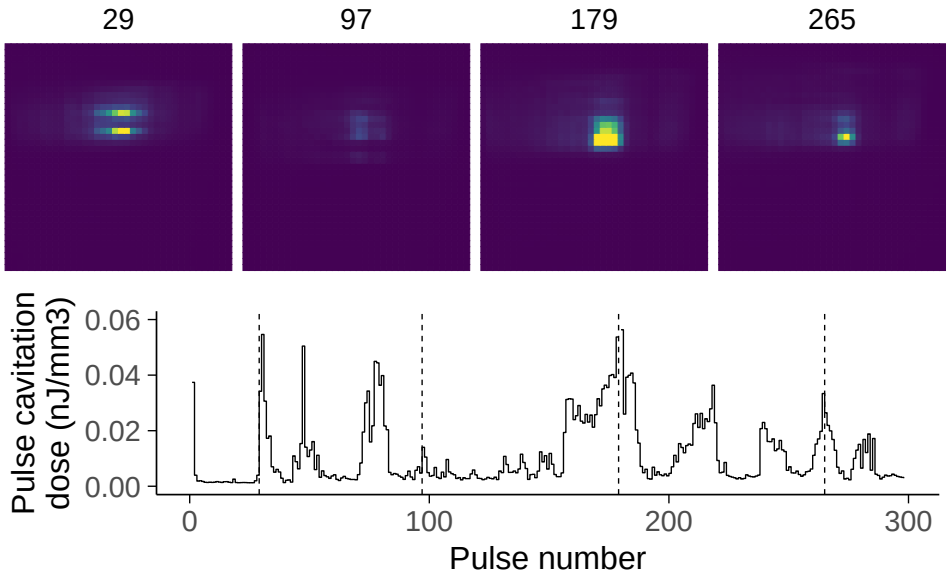

Figure 2.4: Cavitation dose of individual pulses over the treatment duration, insets show PAM maps normalised to the maximum power density over the treatment at representative time-points. PAM maps are over a 15 mm square.

2.4 Relating cavitation dose to tumour growth

The effect of cavitation dose on tumour growth is shown in figure 2.5, where a qualitative correlation between growth rate and cavitation dose (denoted by the color of the tumour growth curves) can be observed, with higher cavitation doses corresponding to slower growth curves. In order to focus on the differences between subjects that were given the same treatment, rather than on the effect of treatment protocol, mice that received no ultrasound were excluded from the analysis.

A moderate negative correlation between relative tumour volume at 7 days after the second treatment and cavitation dose was found in all treatment groups, with a Spearman's ρ of -0.71 ($p = 0.002$) for IgG, -0.51 ($p = 0.02$) for anti-PD1 and -0.64 ($p = 0.0002$) for anti-PDL1 (figure 2.6). This suggests that even at this early stage the effect of the treatments were influenced by the levels of cavitation received.

The mean cavitation dose received by mice that showed stable disease (SD) or partial response (PR) at this timepoint according to Response Evaluation Criteria in Solid Tumours (RECIST) (Eisenhauer et al. 2009) was higher in all treatment

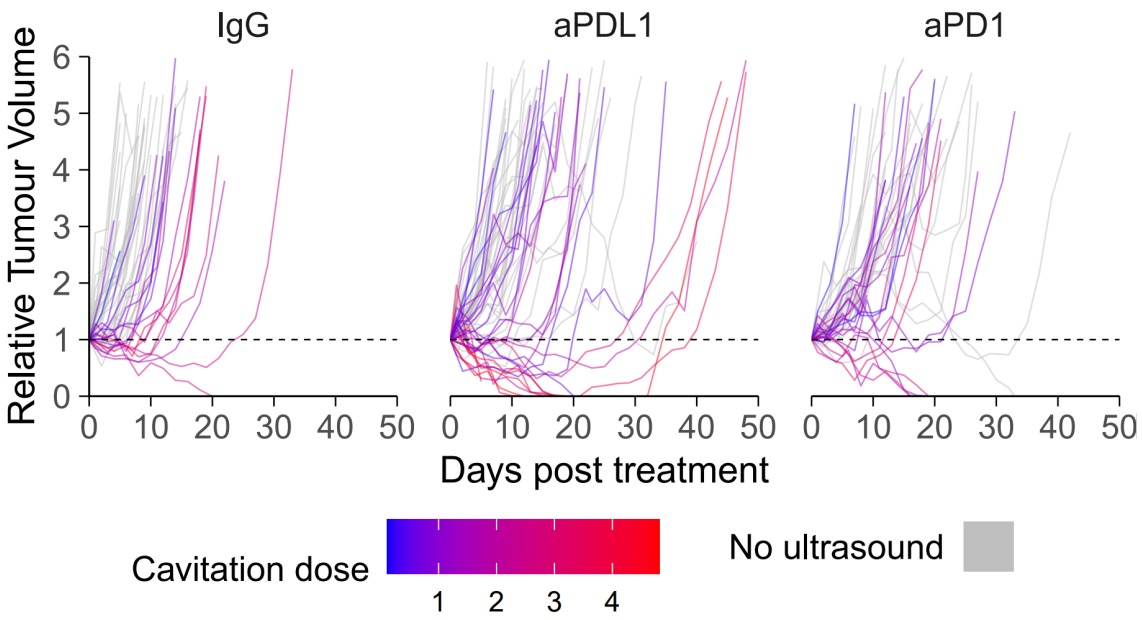

Figure 2.5: Tumour volume relative to volume at treatment for the three treatment groups. Grey lines represent mice that were not exposed to US, other lines are coloured by cavitation dose

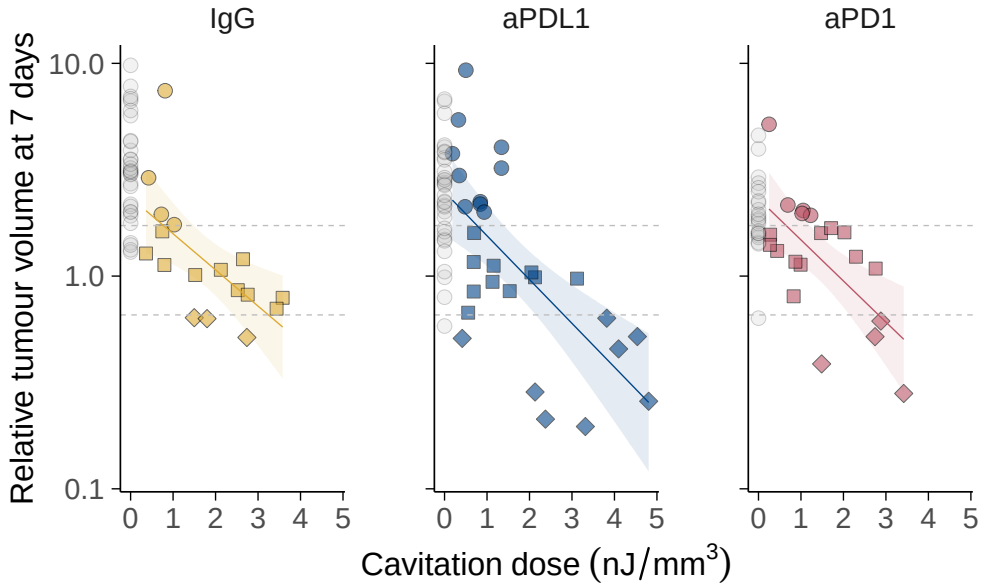

Figure 2.6: Relationship between relative tumour volumes 7 days post-treatment and cavitation dose. The dashed lines separate PD, SD and PR regions based on RECIST criteria. Grey points represent mice that were not exposed to ultrasound.

groups than that received by mice that showed progressive disease (PD), with a difference of 1.3 nJ/mm^3 (95% CI 0.63-2.0 nJ, p = 0.0009) in the IgG group, 0.78

nJ/mm^3 (95% CI 0.12-1.5, p = 0.02) in the anti-PD1 group and 1.5 nJ/mm^3 (95% CI 0.70-2.2, p = 0.0006) in the anti-PDL1 group (figure 2.7). All PD responses occurred in mice that received a cavitation dose of less than 1.4 nJ/mm^3 regardless of treatment group. This indicates that the treatment outcomes as determined by a standard clinical metric show a strong relationship with the cavitation dose received. It is especially interesting to note that this is true even in the case of the IgG group.

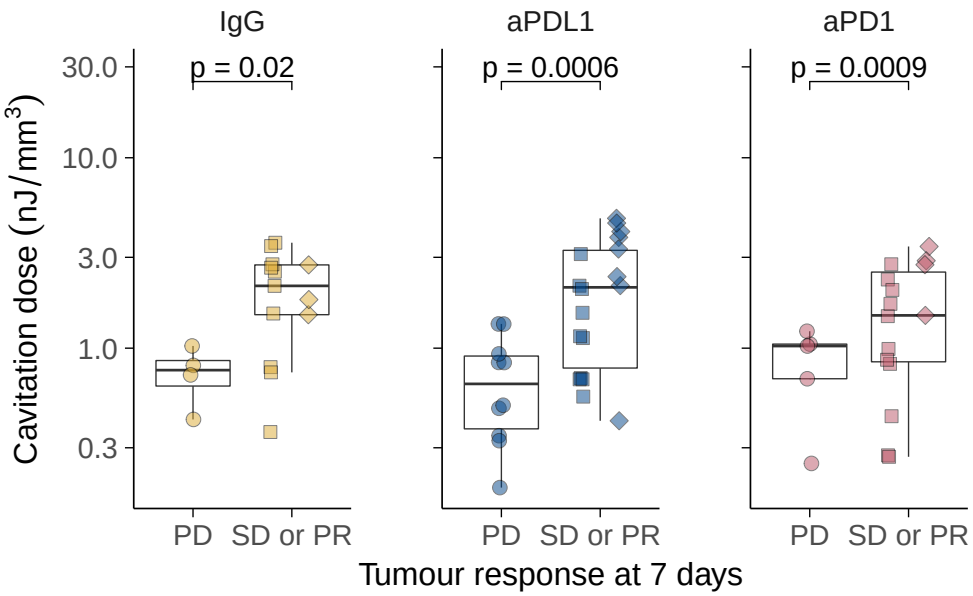

Figure 2.7: Cavitation dose received by mice showing different RECIST responses. Box-plots show the median (middle line), lower and upper quartiles (box) and 1.5 times the interquartile range (whiskers).

2.5 Relating cavitation dose to survival

2.5.1 Hazard ratio dependence on cavitation dose

The effect of cavitation dose on survival was analysed by fitting separate additive Cox models to the data, a standard method of analysing survival data which allow us to study the effect of cavitation on each treatment group with minimal assumptions. The effect of cavitation dose on log hazard was modelled with penalized cubic regression splines, to allow for the biologically plausible scenario of a non-linear effect such as a threshold effect or an effect reversal, while the correlation between

mice treated with the same protocol was accounted for using a frailty model. As death occurs when the tumour volume reaches a threshold of 1000 mm^3, the volume at treatment can be expected to affect time to death and was therefore included in the model as a linear predictor.

In the Cox model the instantaneous hazard rate corresponds to the probability that a patient dies in the interval t and $t + \Delta t$ as Δt tends to 0. The log of this hazard rate is modelled as a function of a baseline hazard and a linear combination of explanatory variables.

The hazard ratio, corresponding to the hazard rate relative to a representative low cavitation reference (chosen as the first quartile of the cavitation dose distribution) in each treatment group, shows a similar dependence on cavitation dose in the IgG and anti-PDL1 groups (figure 2.8). In both groups, the hazard ratio decreases as the cavitation dose increases in the 0-0.75 nJ/mm^3 range and, with stronger evidence, in the 0.75-2.5 nJ/mm^3 range. In the anti-PDL1 group, but not in the IgG group, evidence for the same dependence was found up to 3.8 nJ/mm^3. The confidence intervals for the anti-PD1 group are too wide across the entire measured range to draw any conclusions. This suggests that, in the case of IgG and anti-PDL1 cavitation has both a statistically and therapeutically significant effect on the enhanced survival of the mice.

In order to illustrate the effect of receiving different cavitation doses when given the same treatment, the adjusted hazard ratio estimates for each drug at zero or a representative high cavitation (chosen as the third quartile of the cavitation dose distribution) are shown in table 2.2 with their 95% confidence intervals. Cavitation dose was found to have very similar effects in the anti-PDL1 and IgG groups: compared to a mouse that receives a cavitation dose of 0.75 nJ/mm^3, the adjusted hazard ratio for a mouse that receives 2.5 nJ/mm^3 is 0.35 (95% CI 0.18-0.68) for the anti-PDL1 group and 0.24 (95% CI 0.10-0.57) for the IgG group (table 2.2).

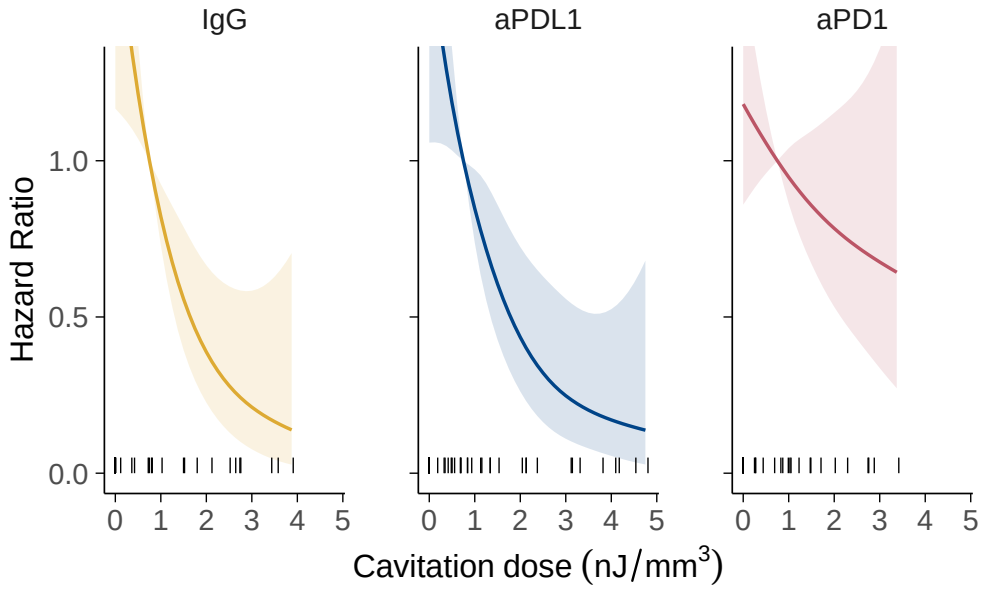

Figure 2.8: Hazard ratios relative to a cavitation dose of 0.75 nJ/mm^3, with 95% pointwise confidence intervals. Rug lines represent the cavitation doses received by individual subjects.

Treatment group	Cavitation dose (nJ/mm^3)	Adjusted hazard ratio	95% CI
IgG (n=50)	0	1.77	1.00-3.12
	0.75 (ref)	1.00	-
	2.5	0.24	0.10-0.57
anti-PDL1 (n=64)	0	1.67	1.07-2.62
	0.75 (ref)	1.00	-
	2.5	0.35	0.18-0.68
anti-PD1 (n=42)	0	1.16	0.87-1.56
	0.75 (ref)	1.00	-
	2.5	0.76	0.46-1.25

Table 2.2: Summary of adjusted hazard ratio's and 95% CI for each treatment group with a reference of 0.75 nJ/mm^3.

Although the effect of cavitation dose is comparable in the two groups, the different baseline hazards (figure 2.9) imply that, at a given cavitation dose, the hazard ratios of mice in different treatment groups relative to an untreated mouse (IgG group, no cavitation) are not equal.

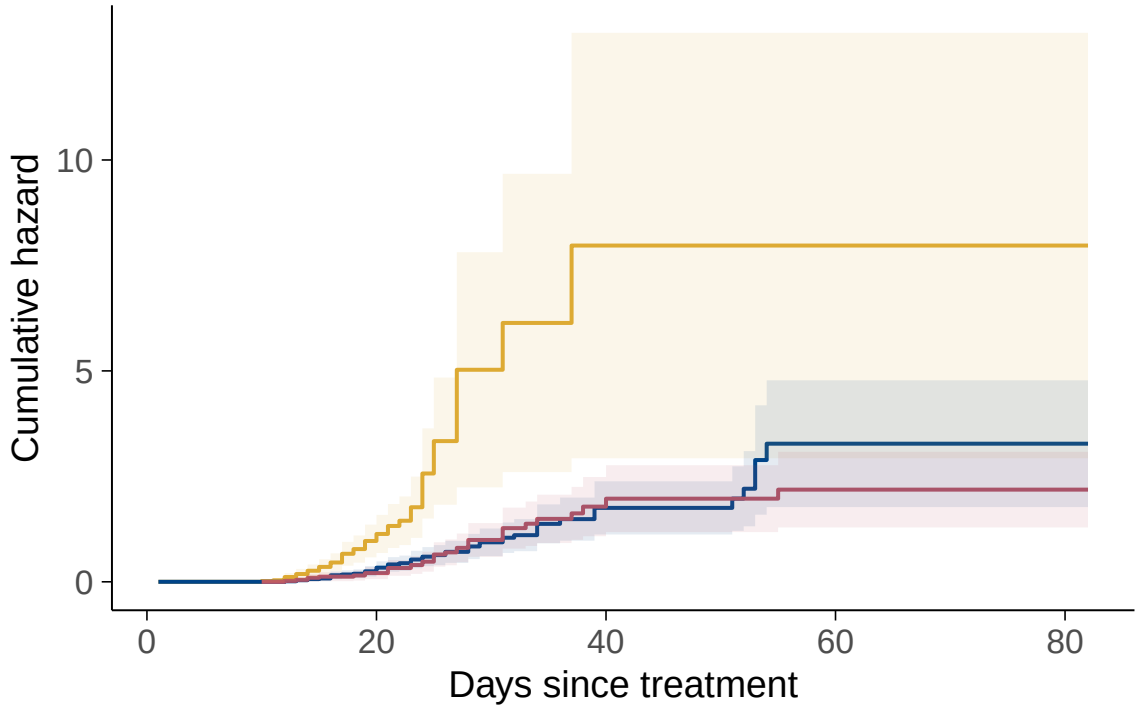

Figure 2.9: Cumulative baseline hazard of the three treatment groups over time.

2.5.2 Survival curve modelling

In order to check the validity of the Cox model, simulated data was produced whereby the mice received the same cavitation doses as the experimental cohort, these were then compared to the experimental Kaplan-Meier curves (figure 2.10). As can be seen, a good agreement can be found between the simulated and experimental results.

With the model validated, we can then explore what the effect on survival would be if all mice had received a controlled cavitation dose. A representative low (0.75 nJ/mm^3) and high (2.5 nJ/mm^3) cavitation dose correspond to a therapeutically relevant difference in survival in both the IgG and anti-PDL1 groups (figure 2.11). It is also important to note that the predicted median survival for a 0.75 nJ/mm^3 cavitation dose is not substantially longer than the experimental median survival of mice that did not receive ultrasound.

Two things are especially interesting to note in figure 2.11. The first is that there is only a small therapeutic difference between a mouse that received ultrasound treatment at a “low" level of cavitation, and a mouse that received no ultrasound

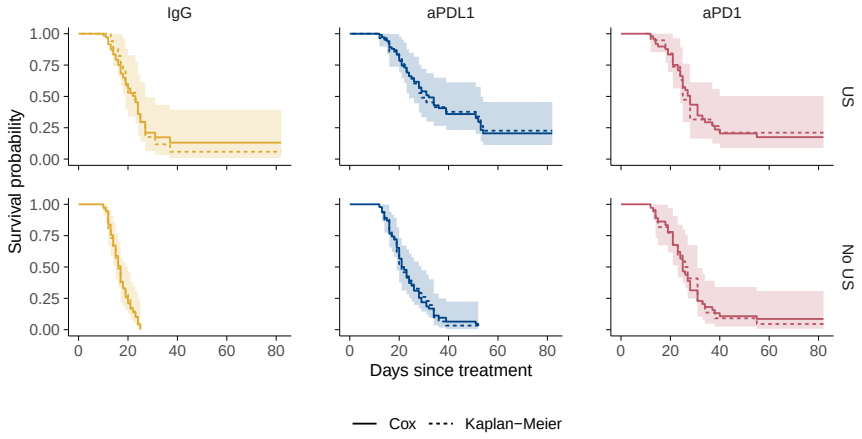

Figure 2.10: Kaplan-Meier curves showing experimental results against simulated Cox model curves in the case where the simulated mice receive the same cavitation doses as the experimental cohort.

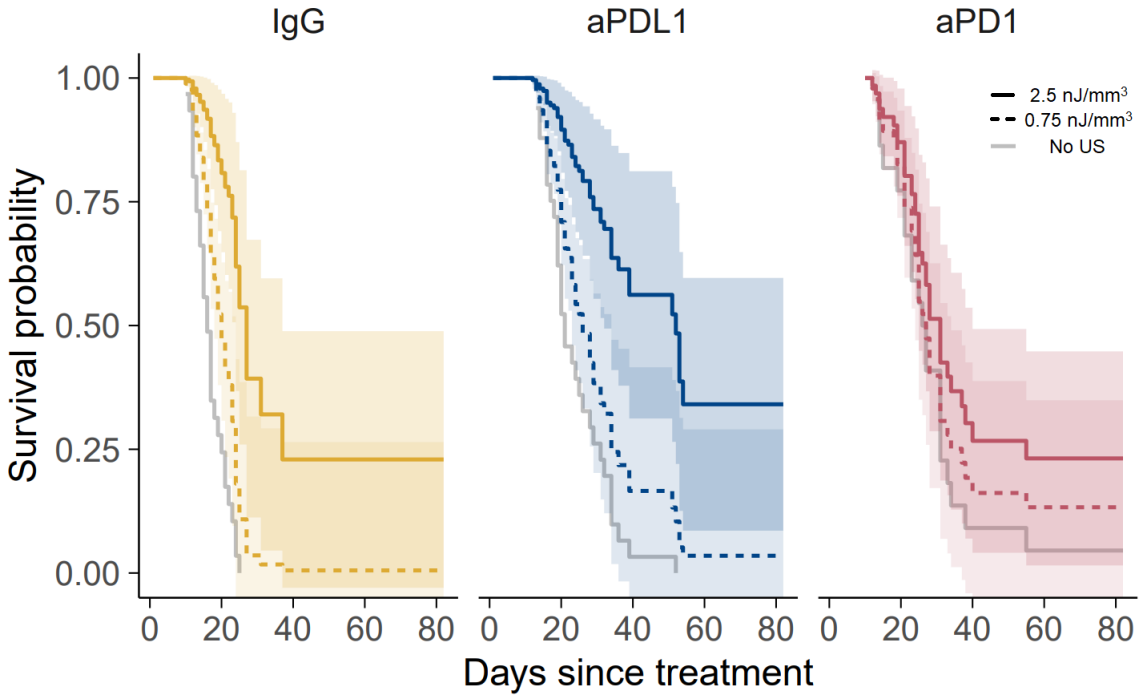

Figure 2.11: Kaplan-Meier curves showing experimental non US treated groups in grey against simulated Cox model curves showing simulated results in the case where all mice received either 0.75 or 2.5 nJ/mm^3.

treatment at all. Secondly, in the case of the IgG and anti-PDL1 treatment groups the effect of a “high" cavitation can be at least as significant as the effect caused by the presence or absence of an active drug. In the case of anti-PD1 no statistically significant effect of cavitation could be discerned.

2.6 Relating cavitation dose to immune response

The gene expression profile of tumours in mice treated with anti-PDL1 or IgG was analysed in the original work at 24 hours (n = 6 for both IgG and anti-PDL1) and 5 days after treatment (n = 11 for IgG, n = 12 for anti-PDL1) using a Nanostring panel of 770 cancer and immune related genes (Katti 2020) . The original analysis determined the differential gene expression between insonated and non-insonated tumours in different treatment groups. In an attempt to understand why the cavitation dependence of hazard ratio is similar in the anti-PDL1 and IgG groups, gene expression data was re-analysed using cavitation dose as a continuous predictor and estimated the dependence of gene expression on cavitation dose as the linear slope of log_2 counts, which corresponds to the log_2 fold change for a 1 nJ increase.

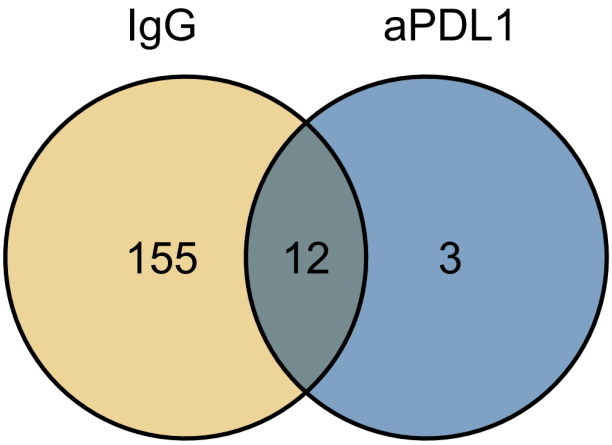

Figure 2.12: Venn diagram of differentially expressed genes in the IgG and anti-PDL1 groups.

At the 24 hours timepoint, 20 genes in the IgG group and 15 genes in the anti-PDL1 group were found to have a statistically significant dependence on cavitation dose greater than 0.8 log_2 fold change/(nJ/mm^3), corresponding to a 2-fold change between mice that received cavitation doses that differ by 1.25 nJ/mm^3. All but three of the cavitation-dependent genes in the anti-PDL1 group (*Cd69*, *Eomes* and *Il7*) are shared with the IgG group (figure 2.12). The slopes for a selection of genes are shown in figure 2.13 with their 95% confidence intervals, a selection of the distributions can be found in figure 2.14. In order to isolate the effect of

cavitation alone on the immune response to the treatment, we focused on the effect of cavitation in the IgG group. The genes most affected by cavitation, with an effect of up to 4.8 log_2 fold change/(nJ/mm^3), include chemokines (*Cxcl3*, *Cxcl2*, *Ccl3*, *Cxcl5*, *Ccl4*, *Cxcl1*, *Ppbp*), chemokine receptors (*Cxcr2*, *Ccrl2*), as well as other pro- and anti-inflammatory cytokines (*Il1b*, *Il6*, *Osm*, *S100a8*) and cytokine receptors (Il1r2, Il1rn). Other macrophage-related (*Arg1*, *Serpinb2*) and matricellular (*Thbs1*) genes were also found to be upregulated in a cavitation-dependent manner. The cavitation dependence was similar in the anti-PDL1 and IgG groups at 24 hours but diverged at 5 days: while gene expression in the IgG-treated tumours returned to the zero-cavitation baseline at all cavitation doses, it was only partially decreased in the anti-PDL1 tumours.

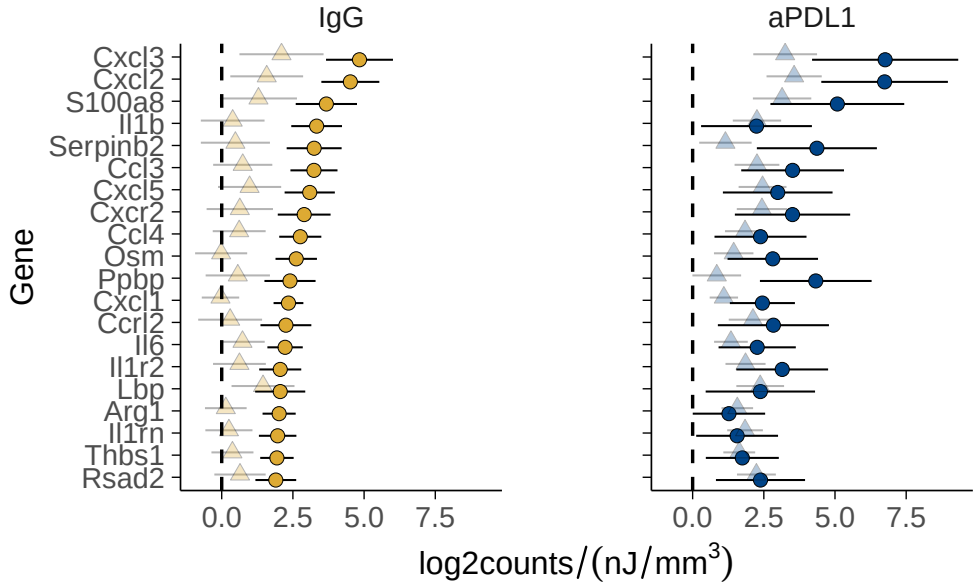

Figure 2.13: Effect of cavitation dose on differential gene expression at 24 hours (circles) and 5 days (diamonds) of the 20 genes that have the highest log2 fold change/(nJ/mm^3) in the IgG group at 24 hours.

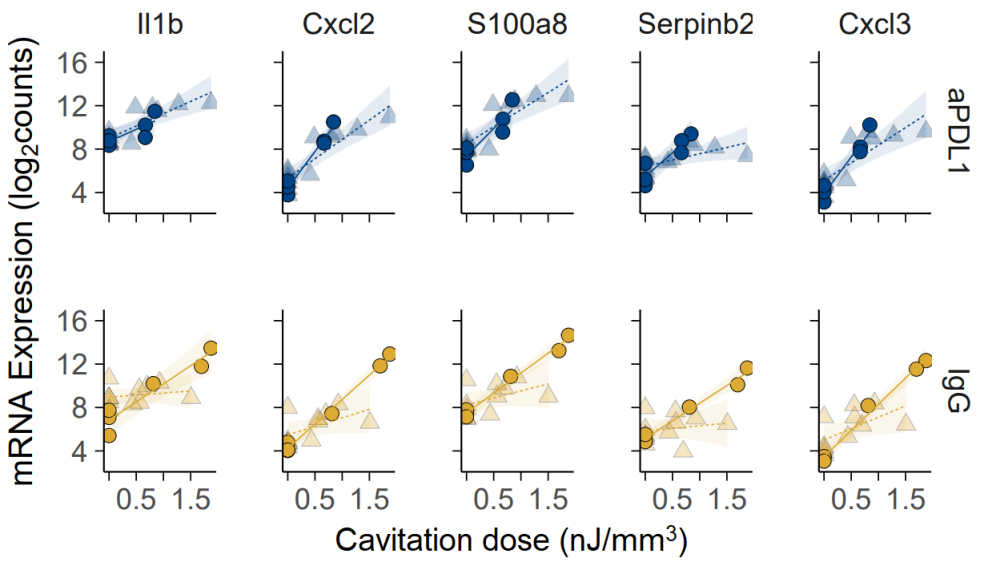

Figure 2.14: Gene expression at 24 hours (circles) and 5 days (diamonds) as a function of cavitation dose.

2.7 Relating cavitation dose to drug delivery

Figure 2.15 shows the levels of Cetuximab delivered to the tumour for the control group (without US) and the two ultrasound groups with high and low concentrations of SPs. The use of cavitation nucleation agents and ultrasound was found to increase the concentration of drug delivered to the tumour in all cases, compared to the non-ultrasound-treated passive delivery controls.

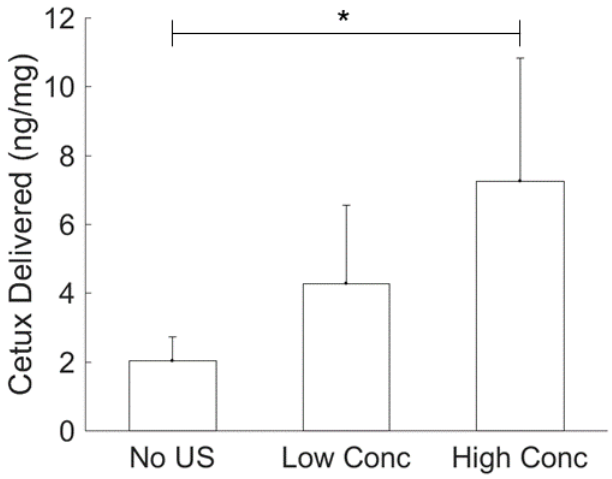

Figure 2.15: Cetuximab (Cetux) delivered between the three groups, no ultrasound (US), low (8.75 mg/ ml), and high (17.5 mg/ concentration (conc) of SonoTran particles). * corresponds to $p < 0.05$ using a two tailed t test.

For each tumour PAM videos were generated showing the cavitation energy that was delivered over the course of the therapy. As expected, the cavitation energy was contained to the mouse (figure 2.16). This cavitation dose metric was then found to be related to the concentration of Cetuximab delivered to each tumour ($p<0.001$) (figure 2.17).

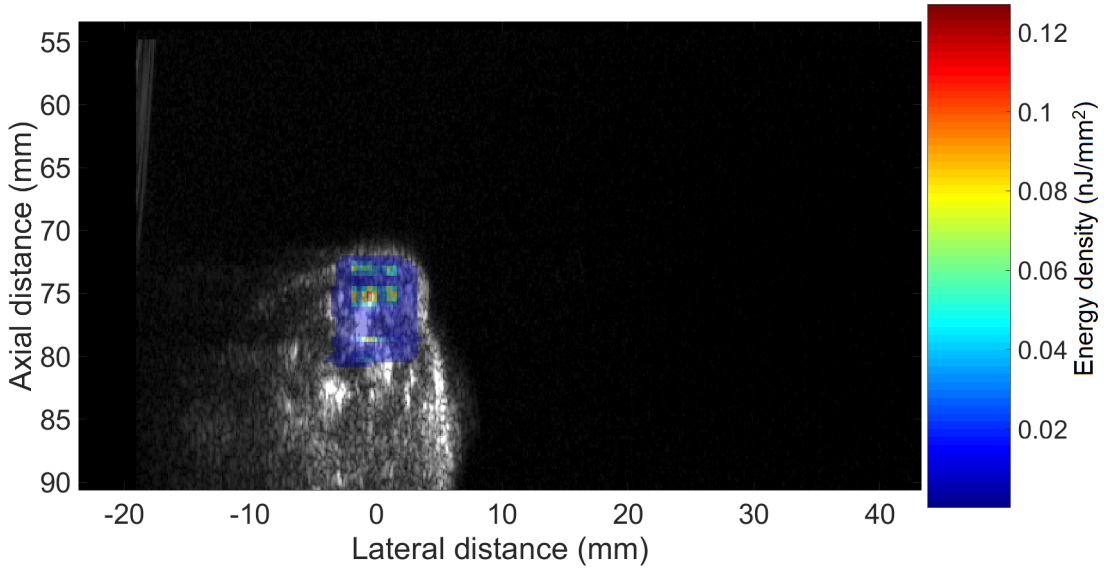

Figure 2.16: Example PAM map overlaid on its corresponding B-mode image.

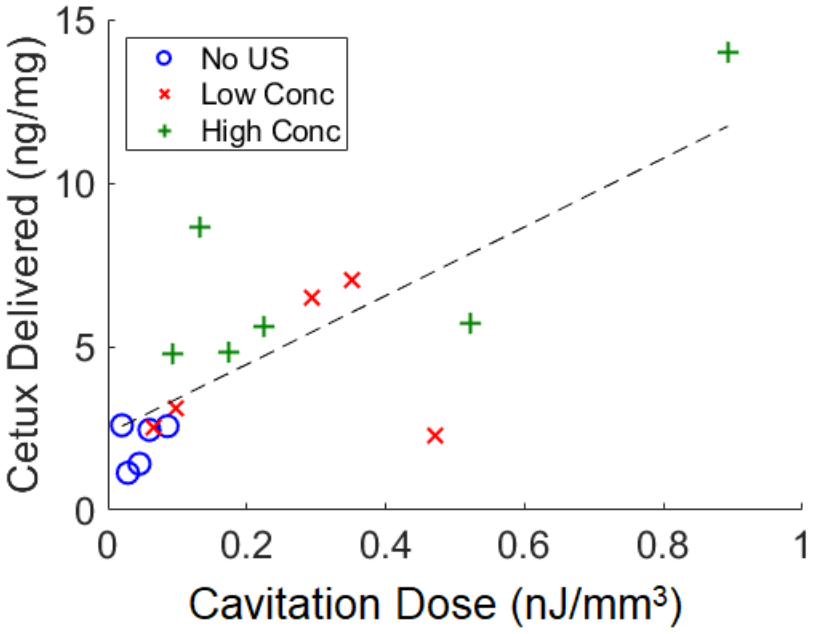

Figure 2.17: Cavitation dose for each tumour against the concentration of Cetuximab (Cetux) delivered to that tumour, with line of best fit plotted on top ($R^2 = 0.5714$).

2.8 Discussion

2.8.1 Survival study

It has previously been shown that ultrasound exposure in the presence of cavitation agents can enhance the delivery of checkpoint inhibitors to CT26 xenograft tumours and improve survival outcomes (Katti 2020). Here, the data was re-analysed using the cavitation dose as a metric of cavitation to investigate the effect of cavitation variability between subjects given the same treatment. Two measures of efficacy, the early tumour response based on RECIST criteria and the hazard ratio of death relative to a low cavitation treatment, were found to be dependent on the effective cavitation dose, with clinically relevant differences between low and high cavitation. Analysis of the cavitation dose dependence also revealed a previously overlooked effect of cavitation on tumour response even in the absence of checkpoint inhibitors.

These results provide a link between the inter-individual variability of the tumour response and the variability of the cavitation generated during treatments. The fact that the cavitation dose metric can partially explain this link supports the

hypothesis that the biological effects of cavitation, in the context of ultrasound-enhanced delivery of checkpoint inhibitors, are correlated with the average energy density deposited on a tumour. It is especially interesting to note that this link also appears to exist even in the case of the delivery of the control IgG molecules, suggesting additional effects beyond the enhancement of drug delivery. This is, to the best of my knowledge, the first time that a relationship has been established between survival and a continuous metric of cavitation. In a context such as immunotherapy where the inter-individual variability of therapeutic outcome is high, implementing a monitoring protocol could have important clinical benefits. While in this study the cavitation analysis was done post treatment, PAM can be implemented in real time (Kamimura et al. 2020) to provide feedback control during treatment. Treatment parameters like pressure or duration could then be adjusted, either manually or automatically (O'Reilly and Hynynen 2012; Arvanitis et al. 2012; Sun et al. 2017) until a therapeutically relevant cavitation dose is delivered. Even in the absence of feedback control, the cavitation dose delivered to each patient could have a prognostic value and help plan personalized treatments.

The previously proposed mechanism for enhanced survival in ultrasound-enhanced delivery of checkpoint inhibitors is that cavitation improves efficacy by increasing the tumour concentration of systemically delivered checkpoint inhibitors (Katti 2020). Reanalysis of the IgG group data, however, revealed an unexpected effect of cavitation alone, in the absence of checkpoint inhibitors, on both tumour response at 7 days post-treatment and survival, which suggests that ultrasound treatment could affect cavitation-enhanced immunotherapy in ways that extend beyond improved delivery. There are a range of potential mechanisms for this effect. Firstly it is possible that cavitation is leading to direct damage of tumour cells ultimately leading to tumour shrinkage similar to effects seen in histotripsy (Khokhlova et al. 2015). Secondly cavitation could potentially be leading to damage to the vasculature feeding the tumour, leading to starvation and death of tumour cells. Thirdly damage to tumour cells could lead to the release of antigens into the bloodstream, stimulating the immune system into recognising and potentially damaging the tumour cells,

which would be in agreement with the findings of (Qu et al. 2020). Further studies will need to be conducted to further investigate these potential mechanisms.

2.8.2 Gene expression study

An exploratory gene expression analysis revealed a strong dependence between cavitation dose and the expression of classic markers of sterile inflammation, with a cavitation-dependent upregulation of pro-inflammatory cytokines and genes involved in myeloid infiltration. This is in agreement with the findings of (Fite et al. 2021), who studied the immune modulation caused by high intensity focused ultrasound in a syngeneic murine breast cancer model. One of their experimental groups was treated with high intensity focused ultrasound at 3 MHz and 16.9 MPa peak negative pressure without cavitation agents. Like in the Nanostring study, a low duty cycle was chosen to minimise thermal effects and the tumours harvested at 24 hours after treatment. They found a very similar transcriptional signature in tumours, which they attributed to an acute inflammatory response, with up-regulation of *Cxcr2*, *Il1b*, *Osm*, *Cxcl2*, *Cxcl5*, *Il1r2*. Importantly, differential gene expression in the mechanically treated group appears to be highly variable between mice, which is consistent with the high variability of cavitation levels that was found in this study and reinforces the need for effective cavitation monitoring.

Although a mechanistic explanation of the role of cavitation-induced inflammation in tumour response is outside the scope of this study, the observation of a cavitation-dependent inflammatory response points to some of the possible ways in which cavitation could affect survival beyond improved delivery of checkpoint inhibitors. The damage associated molecular patterns (DAMPs) that triggered the inflammatory response could have originated from the unanticipated mechanical destruction of either tumour or endothelial cells. Both processes could contribute to tumour regression through direct reduction of tumour mass, release of tumour antigens priming a more effective immune response, or restriction of the vascular supply leading to tumour starvation. The direct role of inflammation on tumour growth is more complex (Greten and Grivennikov 2019). Acute inflammation has

been shown to correlate with immune tolerance and tumour progression in different settings, including surgical resection (Krall et al. 2018; Hiller et al. 2018), and incomplete ablation (Shi et al. 2019). On the other hand, there is evidence of therapy-induced inflammation contributing in some cases to immune-mediated tumour eradication (Ghiringhelli et al. 2009). The observed survival outcomes are probably the result of a complex interplay of cavitation effects, encompassing drug extravasation, biomechanical effects, and innate and adaptive immune processes, potentially acting in opposing directions but balancing out to afford a net outcome of tumour regression.

2.8.3 Drug delivery study

The relationship between cavitation dose and drug delivered to the tumour appears to be linear within the parameter range explored, and the fairly strong correlation indicates both that the amount of cavitation generated within the tumour is critical in determining the levels of drug delivery achieved and indicates the potential for PAM to be used as a real time method of monitoring the efficacy of cavitation-enhanced antibody delivery therapies.

It is worth noting that the linear relationship found appears independent of the initial groups used within the study. As such the PAM derived cavitation dose metric could be used to monitor the efficacy of the treatment regardless of the cavitation agent concentration used.

2.9 Conclusion

These results provide evidence that the PAM derived cavitation dose in tumour models correlates quantitatively with cavitation-enhanced drug delivery. It is therefore not surprising that, when an immune response is mediated by drug delivery, the cavitation dose correlates with that immune response. However, what is surprising is that even in the absence of the drug there remains a correlation with the amount of cavitation activity. This suggests that there is an immunological

effect caused by cavitation activity alone, which agrees with previous findings (Fite et al. 2021).

3

Monitoring the Cellular Safety of Cavitation Based Therapies by Passive Acoustic Mapping *in vitro*

Contents

3.1 Introduction

In the previous chapter, the ability of PAM to enable spatiotemporal quantification of cavitation dose and to serve as a potential predictor of drug delivery, immunological response and enhanced survival were established. A logical extension of this finding

is to investigate whether spatiotemporal quantification of cavitation activity can also be correlated with the safety of ultrasound-mediated drug delivery. The focus of the present chapter is therefore to investigate the relationship between PAM-determined cavitation dose and a chosen safety parameter, namely the integrity of the cellular membrane. As a first step the relationship between PAM measured energy and anuclear cellular safety was investigated to test the principle that PAM derived cavitation dose could relate to a biological metric of safety. In this chapter safety was evaluated by observing cavitation damage to red blood cells using haemolysis measurements. A single sample holder is placed at a single location at the focus of an ultrasound field. Red blood cells are co-suspended with one of two cavitation agents and excited over a range of ultrasound parameters to establish if a correlation exists between cavitation dose and haemolysis levels. Red blood cells were chosen due to the simplicity in assessing cell viability and previous work has shown that when PCDs have been used and the level of broadband emission is quantified as an inertial cavitation dose (Chen et al. 2003a) that this inertial cavitation dose has been shown to correlate with haemolysis (Chen et al. 2003a; Everbach et al. 1997; Chen et al. 2003b). In the second step this idea is then expanded to explore the use of PAM to monitor haemolysis levels in multiple different spatial locations simultaneously, allowing for further evidence to be gathered as to PAM's ability to monitor the effects of cavitation in multiple locations simultaneously. Finally, these *in vitro* experiments a wide range of ultrasound parameters to be explored, this allows for investigation as to whether the PAM derived cavitation dose metric is capable of providing a consistent relationship to cellular safety irrespective of the method by which the cavitation was generated.

3.2 Experimental set-up

3.2.1 Overview of the experimental set-up

The experimental set-up for the single sample holder experiment (figure 3.1) was comprised of an eppendorf tube (Eppendorf LoBind microcentrifuge tubes volume 2 mL, Sigma-Aldrich, Hamburg, Germany) containing 0.5 ml of blood mixed with

one of two cavitation agents. Horse blood of physiological haematocrit (Horse Blood in ACD; TCS Biosciences, Buckingham, UK) was used, which contained acid citrate dextrose (ACD) to prevent clotting, was stored in a 4°C fridge and used within 2 weeks of harvesting to ensure that the red blood cells remained in a healthy state before sonication. 0.5 ml was chosen as the volume of blood to be sonicated as it ensured that the entire focus could be placed within the cylindrical region of the eppendorf tube, without creating large regions of blood which were not exposed to ultrasound. Two different cavitation agents were used, at a range of concentrations. SonoVue (SV) (SonoVue, Bracco, Milan, Italy) was chosen to test as it is one of the few cavitation agents that has been clinically approved as an ultrasound contrast agent (Grayburn 2002), and is seeing increasingly common use across a range of therapeutic ultrasound applications (Stride and Coussios 2019). SonoVue was mixed with horse blood in ACD (TCS Biosciences) at room temperature immediately before sonication.

The other agents were chosen to be gas-stabilizing, cup-shaped sub-micron solid particles, as they cavitate purely inertially and can support sustained cavitation activity for tens of minutes (Kwan et al. 2015b; Kwan et al. 2015a), thereby providing a very different type of cavitation nucleation agent. The SonoTran Particles® (SPs) (OxSonics Therapeutics, Oxford, UK) were manufactured using a seed polymerization technique, producing a cup-shaped population of mean diameter 465.3nm, poly-dispersity index (PDI) of 0.048, and Zeta potential of -37.8 mV as determined by Dynamic Light Scattering (Zetasizer Nano ZS, Malvern Panalytical, Malvern, UK). The mean cavity size on the cups was 213 ± 15 nm as determined by Transmission Electron Microscopy, a dimension which determines the size of the air bubbles trapped on each cup following drying and re-suspension. The SPs were used at standard concentrations (1 mg/ml, 10^{10} particles/ml). An experiment was then constructed to test if this principle could also be applied to monitor haemolysis in multiple locations simultaneously. As such a tissue phantom was designed that would allow for two blood samples to be exposed to therapeutic ultrasound pulses during simultaneous PAM imaging.

3.2.2 Ultrasound set-up

The blood was exposed to therapeutic levels of ultrasound using a spherically focussed 0.5 MHz therapeutic transducer (H-107, Sonic Concepts). The eppendorf tube was aligned and cavitation signals were received using two perpendicular co-planar L7-4 linear arrays (L7-4, Verasonics, Kirkland, Washington, USA) connected to a Verasonics Vantage 256 system (Verasonics, Kirkland, Washington, USA). Two arrays were used to improve the resolution of the generated PAM map by allowing for the use of the improved lateral resolution in both directions, as well as increasing the effective array aperture (section 1.7) which allows the set-up to achieve an experimentally derived PAM resolution of 0.4 mm in both the lateral and axial directions. For this reason, 0.4 mm was chosen as the pixel size for PAM processing. The verasonics was controlled by and sent data to a computer, and at the correct time sent a trigger to a function generator (33220A, Agilent Technologies, Santa Clara, CA) which then sent a signal through a 55 dB amplifier (A300; ENI) to a therapeutic transducer (G107 SN27, Sonic Concepts, Bothell, WA) with active diameter 64 mm, focal length 62.4 mm, with a rectangular cut-out at its centre of size 13x45 mm^2 (0.5 MHz centre frequency, 62.4 mm focal length) which allowed for the coaxial alignment of the linear arrays. All equipment was placed within a large water tank of degassed, filtered water.

The samples were then exposed to peak rarefactional pressures in the range of 0-2 MPa, using pulse durations in the range of 50-50,000 cycles with 5 % duty cycle which have been previously shown to be effective for drug delivery across a broad range of applications ranging from antibody (Kwan et al. 2015b) and virus (Myers et al. 2016) delivery to solid tumours, transdermal drug and vaccine delivery (Bhatnagar et al. 2016), and blood brain barrier opening (Kamimura et al. 2018). The peak rarefactional pressures listed are *in situ* pressures measured by direct hydrophone measurements inside the Eppendorf tube (HNA 400, Onda Corp., Sunnyvale, CA, USA). These measurements closely correspond to the free-field pressures due to the absence of attenuating structures at 0.5 MHz in the

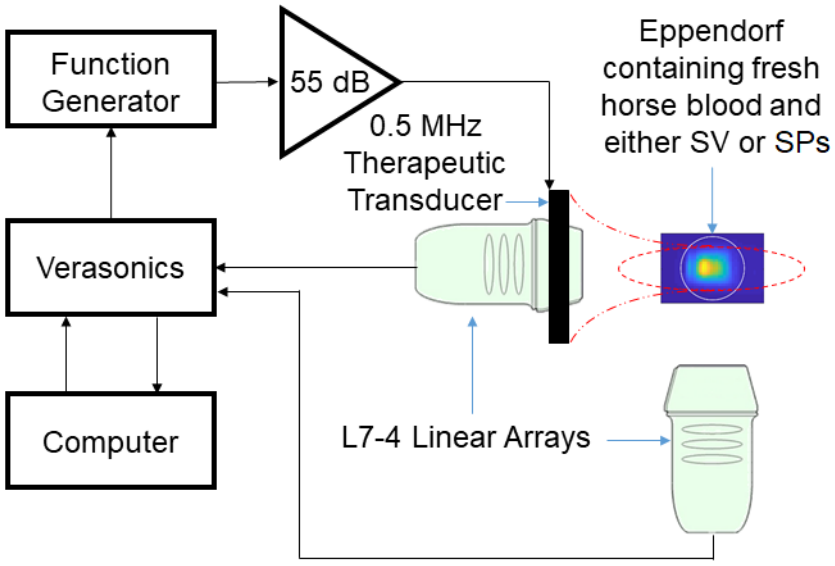

Figure 3.1: Experimental set-up of the single sample blood holder experiment. Two linear arrays at 90 degrees to each other provide improved PAM resolution while an eppendorf containing blood and cavitation agents is exposed to therapeutic ultrasound. Used with permission (Smith and Coussios 2020) (http://creativecommons.org/licenses/by/4.0/)

majority of the acoustic propagation path from the transducer to the 1-cm sample contained within the thin-walled tube.

In order to assess the ability of passive acoustic mapping to monitor haemolysis in multiple locations, it was required that several spatially isolated blood samples could be struck simultaneously with ultrasound. In order to do this a novel *in-vitro* model was developed. The twin sample holder model (figure 3.2 a) consisted of a 50x50x40 mm cuboid of 3% agar gel with two wells. The Perspex cube had four acoustic windows made from Mylar sheets, thereby allowing ultrasound to pass freely both in and out. This ultrasound was generated using two identical therapeutic transducers (Figure 3.2 b). Each well was filled with 0.5 mL of horse blood mixed with SonoTran particles at a concentration of 1×10^{10} cups/mL. Following exposure the blood could be removed from the phantom and measured for haemolysis. A 3 % agar gel was chosen for the phantom as it has enough structural stability to allow for the wells to be structurally stable and resist damage due to cavitation while also having an acoustic impedance similar to soft tissue (table 3.1). After several iterations it was found that cylindrical wells 4.8 mm diameter, 30 mm long,

placed 8 mm apart allowed for a compromise between keeping wells structurally stable, possible to fill and empty, small enough to fit multiple wells within the focus of the therapeutic transducer, and keep the wells far enough apart that they can be easily distinguished within a PAM map.

Material	Velocity (m/s)	Density (kg/m^3)	Attenuation $(dB/cm\,MHz)$	Acoustic Impedance $(MRayl)$	Source
Air	330	1.2	-	0.0004	(Culjat et al. 2010)
Blood	1584	1060	0.2	1.68	(White et al. 1998)
Brain	1560	1040	0.6	1.62	(White et al. 1998)
Breast	1510	1020	0.75	1.54	(White et al. 1998)
Cardiac	1576	1060	0.52	1.67	(White et al. 1998)
Fat	1478	950	0.48	1.40	(Mast 2000)
Liver	1595	1060	0.5	1.69	(White et al. 1998)
Soft Tissue (Average)	1561	1043	0.54	1.63	(Mast 2000)
Water	1480	1000	0.0022	1.48	(Culjat et al. 2010)
3 % Agar	1489	1030	0.0486	1.53	(Collin 2009)

Table 3.1: Summary of the ultrasound properties of various tissues and the tissue phantom material.

The protocol for forming the *in vitro* model was as follows:

1. Agar powder (Sigma-Aldrich) was stirred slowly into PBS (DPBS; Gibco) in a flask until a concentration of 3 % was reached.

2. A magnetic stirrer was placed inside the flask and the mixture was degassed and stirred at 220 RPM for a minimum of 30 minutes.

3. The flask was taken off the degassing system and the magnetic stirrer was removed. A lid was placed loosely on the flask and the flask was microwaved until the solution reached above 85 ℃. Care was taken such that bubbles are not re-introduced in this step, so pauses were necessary during microwaving (usually every 10 seconds).

4. The agar solution was poured into the mould (figure 3.2 b). Care was taken such that no bubbles remain trapped inside the mould during filling.

5. The mould was left to set at 4 ℃ for a minimum of 30 minutes.

6. The top portion of the mould was removed and then replaced with a solid Perspex lid to ensure that the phantom remained watertight.

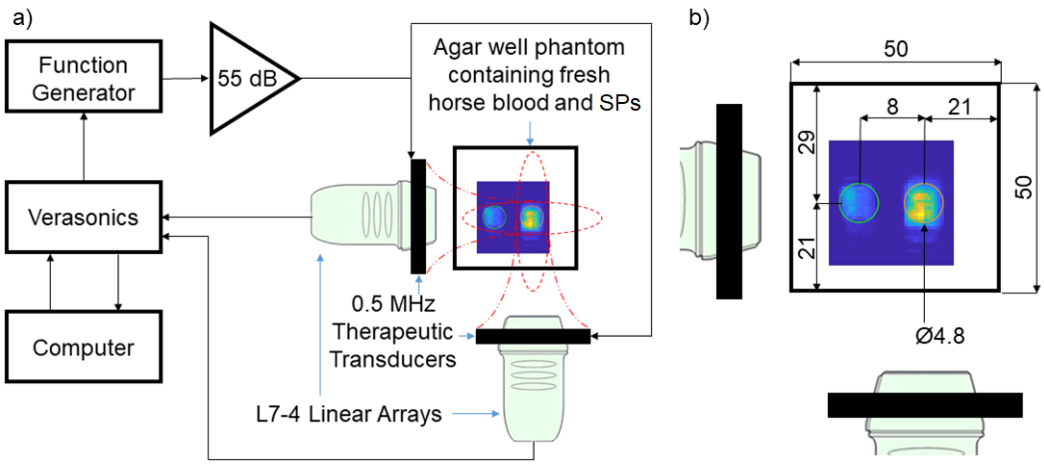

Figure 3.2: Agar phantom experimental set-up. a) The agar phantom was placed with one well in the focus of two perpendicularly co-aligned 0.5 MHz therapeutic transducers, with the other well placed proximally within the full width half maximum of one of the transducers. b) Phantom mould design consisted of a 50x50x40 mm cube of 3% agar gel with two 4.8 mm diameter 30 mm long cylindrical wells placed 8 mm apart. Used with permission (Smith and Coussios 2020) (http://creativecommons.org/licenses/by/4.0/)

3.2.3 Therapeutic transducer calibration

Before the experiment the equipment was carefully characterised. First, the voltage pressure relationship of the therapeutic transducer was found by placing a calibrated hydrophone (HNA-0400, ONDA Corporation, Sunnyville, CA) at the position of maximum intensity within the beam and recording the pressures generated with a range of known input voltages measured using an oscilloscope (HDO4024 Teledyne Lecroy, New York, USA) (figure 3.3 a). Then, the hydrophone was placed at a range of locations within the ultrasound beam. At each location, the root mean square of the signal was calculated and then normalised to the root mean square pressure at the centre of the focus. From this a map could be generated showing the profile of the ultrasound beam (figure 3.3 b). This map could then be used to determine the lateral, elevational, and axial full width half maximum of the beam. Which in this case were 6.4 mm, 3.2 mm, and 38.2 mm respectively.

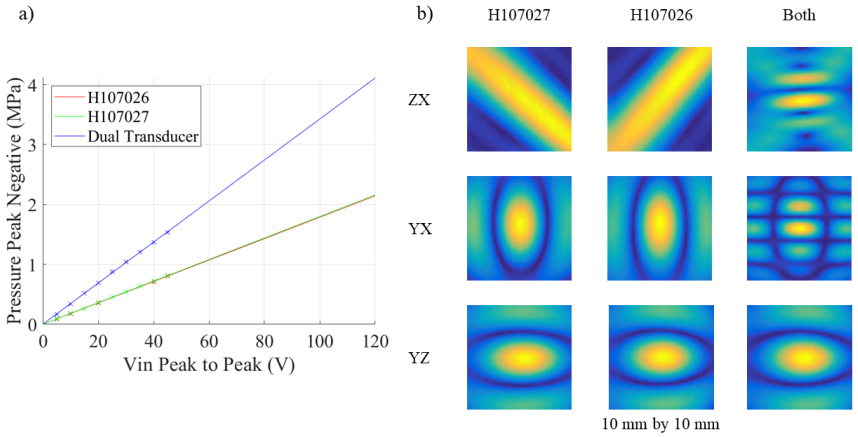

Figure 3.3: a) Pressure voltage relationship of the therapeutic transducer extrapolated to 2 MPa. b) Pressure map showing the pressure distribution around the focus over three planes.

3.2.4 Array calibration

In order to give additional meaning to the results the linear arrays were calibrated on receive mode so that the voltage signal received could be used to estimate the acoustic energy generated during the cavitation event. This allows for the measured cavitation doses to be applied to equivalent set-ups in other labs. To achieve this a substitution calibration is done. A focussed ultrasound transducer emits a short pulse at a wire target, which scatters this pulse evenly in all directions, acting as a point source in 2D. A calibrated needle hydrophone then scans in a plane where the linear array will later be placed. This allows for the pressure field to be characterised (figure 3.4a). A linear array is then placed in the same location (figure 3.4b). This then allows for a pressure-voltage relationship to be found for the linear array, accounting for variation in the signal along the elevational component of the element and accounting for diffraction effects of each element to reach a point source at that location. This calibration can be found at each frequency as the short pulse signal contains enough frequency information that a relationship can be found for each frequency. In order to account for diffraction at all locations this process must be repeated at several locations with calibrations interpolated between spatial locations in order to derive a voltage-pressure relationship for each

element, at each PAM location, at each frequency. In this case as the diffraction effects on the linear array at around 75 mm distance varies slowly data collected for a point source in five locations were used, in the shape of the five points on a dice.

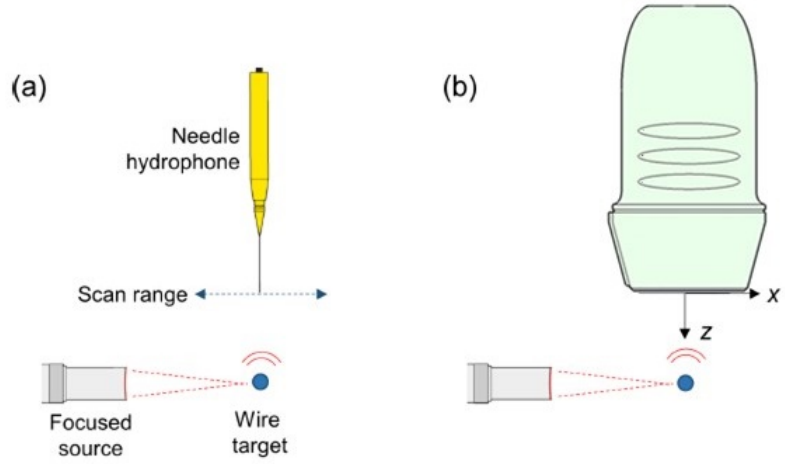

Figure 3.4: Set-up for array calibration by subsitution utilising a wire target as a point source. Figure adapted from (Gray, Lyka, and Coussios 2018).

3.2.5 Alignment

For the first stage of alignment, the relative positions of the therapeutic transducer and the two linear arrays needed to be determined. To achieve this first a hydrophone was placed in the middle of the focal region by moving it to the location which had the maximum amplitude and a time of flight corresponding to the known focal length of the transducer. A B-mode image was then produced using each of the two linear arrays showing the position of the needle tip relative to each of the elements (figure 3.5 a and b). From this and another B-mode of the needle tip in a different location the relative positions of all the elements of the two arrays and the focal region could be determined to an accuracy of ± 0.15 mm. Each eppendorf tube of blood was then aligned using B mode such that the centre of the focus lay in the middle of the eppendorf tube. The vertical alignment was achieved in the case of the nanocup blood mixture by maximising the intensity of the far wall of the eppendorf within the B-mode scan (figure 3.5 c). In the case of the SonoVue blood mixture the back

wall could not be seen due to the acoustic shielding. As such elevational alignment was achieved by moving a known distance above the base of the eppendorf tube.

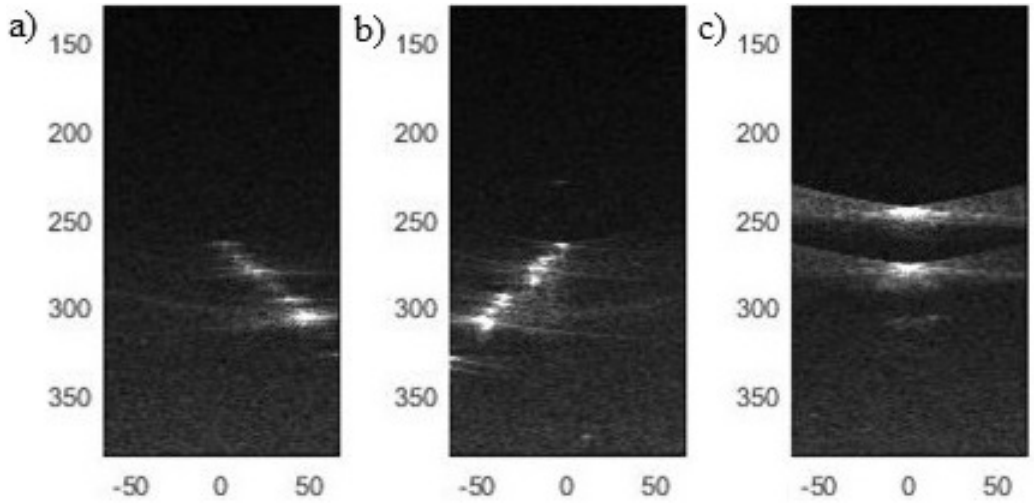

Figure 3.5: B-mode images showing the distance from the linear array in wavelengths on the Y-axis and element number on the X-axis. a-b) B-modes of the needle hydrophone tip in the focal position from the point of view of each of the linear arrays. c) B-mode showing the location of an eppendorf tube filled with SonoTran particles mixed with blood, placed within the centre of the focal region.

3.2.6 Haemolysis measurement protocol

Two 80 µL aliquots of each blood sample were added to 1.12 mL of PBS (DPBS, Gibco, Thermofisher, Massachusetts, United States). One of the diluted aliquots was mixed with 120 µL of 1 % Triton X-100 (Triton™ X-100, Sigma-Aldrich, Hamburg, Germany) in PBS and used as a 100 % reference, while the other one was diluted further with 120 µL of PBS. All samples were centrifuged at 500 g at 4 °C for 5 minutes. The absorbance of the supernatants was measured in triplicate (120 µL per well) in a plate reader (Omega POLARStar, BMG Labtech, Ortenberg, Germany) from 220 to 1000 nm. The processing of this data can be broken down into stages: 1. The average absorbance of three 120 µL wells of PBS was subtracted from all the spectra to remove the effect of the PBS from the blood samples. 2. For each spectra the average absorbance from 750 to 920 nm was subtracted from the total spectra to reduce the effects of scratches on the wells, this was done as no components within the blood absorb light at these wavelengths. 3. The percentage

haemolysis for each blood sample was then calculated as the absorbance at 541 nm divided by the absorbance at 541 nm for that blood sample's positive control, thereby creating an estimate of the percentage haemolysis of that sample.

3.2.7 Signal processing

After the data was received the frequency domain RCB-PAM algorithm in the 3-7 MHz range was applied. An optimum value of $\epsilon = 5$ was found to maximise containment of the energy within the eppendorf tube for this set-up. Previous work by Dr Delphine Elbes (unpublished) estimated experimentally that the resolution of RCB-PAM for this particular acoustic set-up is 0.4 mm in both the axial and lateral directions, as such 0.4 mm was chosen as the pixel size for all PAM maps processed. The algorithm was implemented in the frequency domain as this allowed for easy application of the voltage-pressure calibration and as it marginally improved computation time (Haworth et al. 2017). The cavitation dose is then generated by integrating the RCB-PAM power density maps over the measured area and the duration of the treatment and normalized by total blood volume.

3.3 Haemolysis within a single sample holder

Figure 3.6 illustrates the levels of haemolysis achieved during three parameter sweeps, a pressure sweep, a pulse length sweep (maintaining a 5 % duty cycle) and a concentration sweep with the two different cavitation agents. As was expected, increasing the pressure and concentration increased the levels of haemolysis generated. The levels of haemolysis generated given the intensity of the acoustic field was in line with other experiments done by others previously in the lab, as well as from previous explorations in the literature (Chen et al. 2003a).

For each blood sample, PAM videos were generated so that the cavitation dose could be estimated (figure 3.7). As expected, the cavitation energy was contained within the Eppendorf tube and the focal region. The SPs had sustained cavitation for the duration of the ultrasound exposure, whereas at the higher pressures, most of the SV bubbles were destroyed within the first 5 seconds. The PAM videos when SV

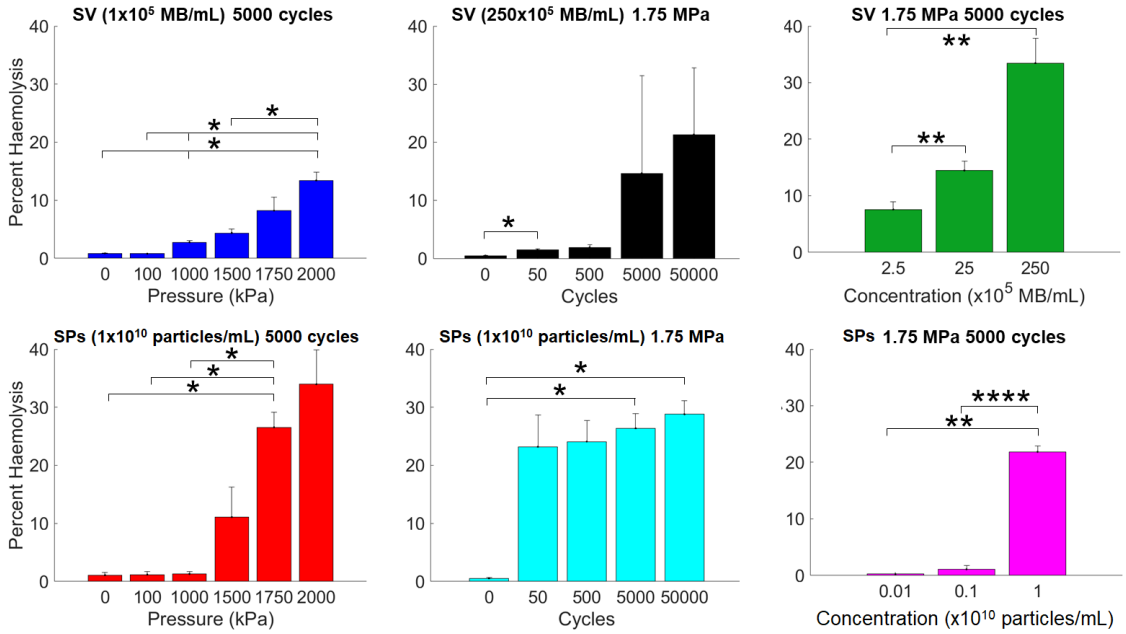

Figure 3.6: Blood mixed with one of two different cavitation agents of varying concentrations and exposed to a range of ultrasound conditions for 30 s, maintaining a 5 % duty cycle (n = 3). Error bars represent one standard deviation. Pairwise comparisons were conducted using Welch's t-test, and the p values were corrected for multiple comparisons using Hommel's method. * $p < 0.05$, ** $p < 0.01$, **** $p < 0.0001$. SPs = SonoTran Particles; SV = SonoVue. Used with permission (Smith and Coussios 2020) (http://creativecommons.org/licenses/by/4.0/)

microbubbles were used revealed an initial increase in cavitation energy over time which then sharply dropped, which is in agreement with the findings by (Hitchcock et al. 2011). One hypothesis as to why this could be the case is that initially the incident pressure field is shielded by bubbles closest to the transducer's surface. Once these bubbles are destroyed or displaced, the incident focus becomes fully formed, able to generate higher pressures in the middle of the Eppendorf tube, accelerating the destruction of microbubbles in that central region. In the case of the SPs, after the destruction of the few air bubbles within the solution, cavitation stabilises, and relatively constant cavitation activity is maintained throughout the treatment. These results match previous findings in the literature (Kwan et al. 2015a).

When the cavitation dose is calculated for each each blood sample it can be found that the relationship for example between cavitation dose and pressure in the case of SV to be as expected, with higher incident pressure creating higher cavitation doses within each sample. It can also be found that the relationship

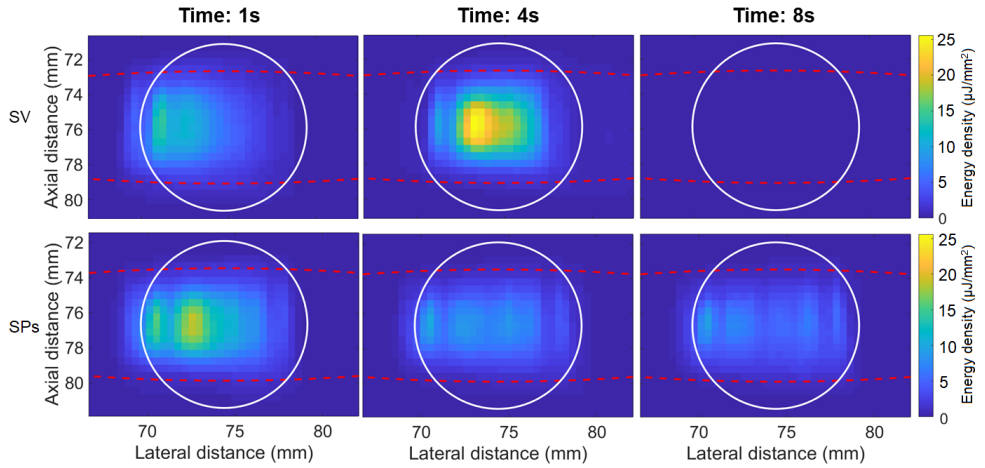

Figure 3.7: Frames from the passive acoustic mapping videos of the treatments. The location of the Eppendorf tube wall was estimated by B-mode, and is marked by a white circle. The location of the full width at half-maximum of the focal pressure was estimated using B-mode of a hydrophone tip placed in the centre of the focus, and is marked by a red dashed oval, with the therapeutic pulse travelling from left to right. Top: SonoVue (SV, 1×10^5 microbubbles [MBs]/mL) mixed with blood. Bottom: SonoTran Particles (SPs, (1×10^{10} particles/mL) mixed with blood. Obtained with 2 MPa, 5000 cycles. Used and modified with permission (Smith and Coussios 2020) (http://creativecommons.org/licenses/by/4.0/)

between pressure and cavitation dose appears to a first approximation to be similar to the relationship between pressure and percent haemolysis (figure 3.8a). If instead percent haemolysis is plotted against cavitation dose (figure 3.8b), a relationship can be found between them, where samples that received a higher cavitation dose also have higher levels of haemolysis.

Another question investigated was whether there was any improved correlation with filtering the cavitation signal to segment the Broadband components which are associated with inertial cavitation signals and the narrowband components which are associated with non-inertial cavitation. In order to investigate this the frequency domain cavitation signal post beamforming was multiplied by a square wave comb style filter, with a 50 kHz bandwidth located at each of the harmonics and ultraharmonics. Then the broadband cavitation energy was divided by the ratio between the size of the broadband filter and the full bandwidth of the signal (between 3 and 7 MHz), this recovered the full broadband energy. This was then subtracted from the total energy to find the narrowband energy. No improvement

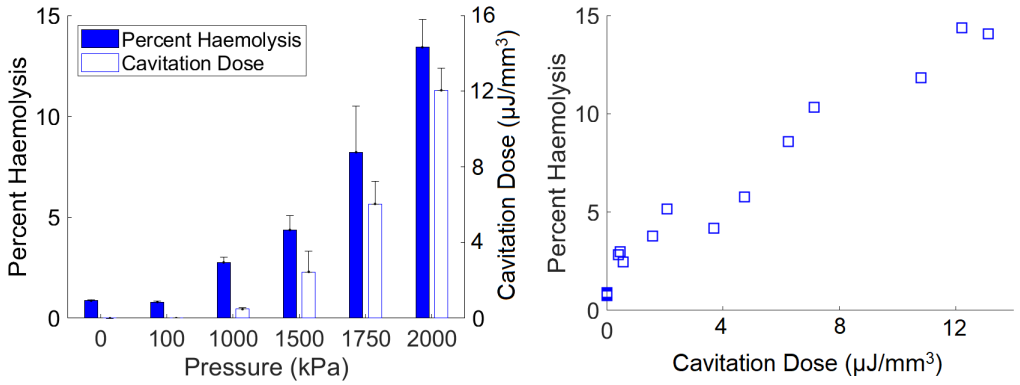

Figure 3.8: Blood mixed with SonoVue (SV, 1×10^5 MBs/mL) exposed to a variety of pressures (5000 cycles, 5% duty cycle). (a) Amount of haemolysis achieved at each pressure level plotted with the total passive acoustic mapping-derived cavitation dose delivered upon exposure to each pressure level (n = 3). (b) Each blood sample can be plotted to find the relationship between the cavitation dose delivered and the level of haemolysis reached. Error bars represent one standard deviation. Used with permission (Smith and Coussios 2020) (http://creativecommons.org/licenses/by/4.0/)

in correlation between percent haemolysis and broadband or narrowband cavitation energy was found over simply using the total cavitation dose. As such the total cavitation dose is used for the remainder of the work.

When the total, broadband, and narrowband cavitation doses were observed over time (figure 3.9) (and validated by looking at the frequency spectra of the signals) it could be seen that within the parameter range being tested almost all of the cavitation dose observed was broadband in nature, which could potentially explain the lack of improved correlation found by segmenting the signals by frequency. It was also found that The SPs had sustained cavitation for the duration of the ultrasound exposure, whereas at the higher pressures, most of the SV bubbles were destroyed within the first 5 seconds.

Once the cavitation dose for each blood sample was calculated, a relationship was found for every parameter sweep exhibiting an increase in haemolysis with increasing cavitation dose. When these plots are superimposed on each other, it was found that a monotonic relationship existed that was comparable regardless of the applied pressure, pulse length, cavitation agent type or concentration used (figure 3.10)

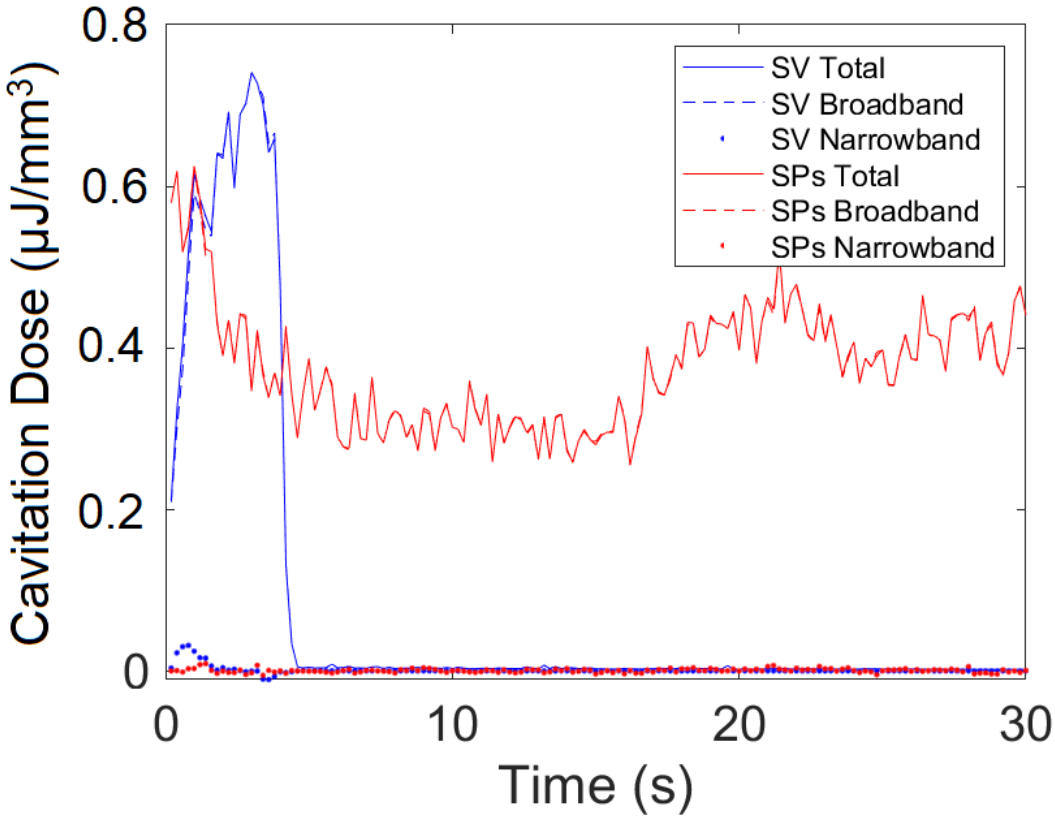

Figure 3.9: Example cavitation dose over time for SV (1×10^5 MBs/mL) and SPs (1×10^{10} particles/mL) mixed with blood. Obtained with 2 MPa, 5000 cycles, split into broadband, narrowband, and total caviation doses. Used and modified with permission (Smith and Coussios 2020) (http://creativecommons.org/licenses/by/4.0/)

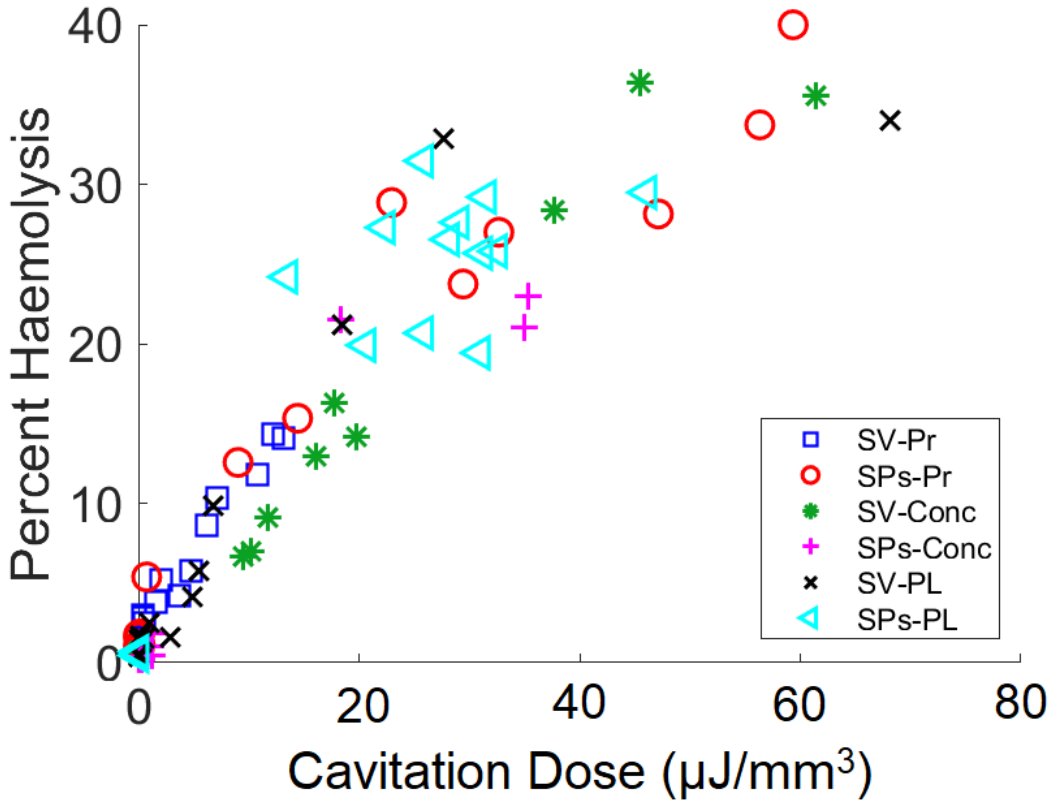

Figure 3.10: A relationship was found between cavitation and haemolysis that was comparable regardless of the cavitation agent type (SonoVue [SV], SonoTran Particles [SPs]), concentration (Conc), applied ultrasound pressure (Pr) or pulse length (PL) used. Used and modified with permission (Smith and Coussios 2020) (http://creativecommons.org/licenses/by/4.0/)

3.4 Haemolysis within a multi sample holder

Blood within the tissue phantom similarly indicated that an increase in the incident pressure led to an increase in the levels of haemolysis, and as expected, the well in the middle of the focus (focal well) experienced higher levels of haemolysis than the non-focal well (figure 3.11a). Cavitation energy was contained within the wells and the focal region (figure 3.11b).

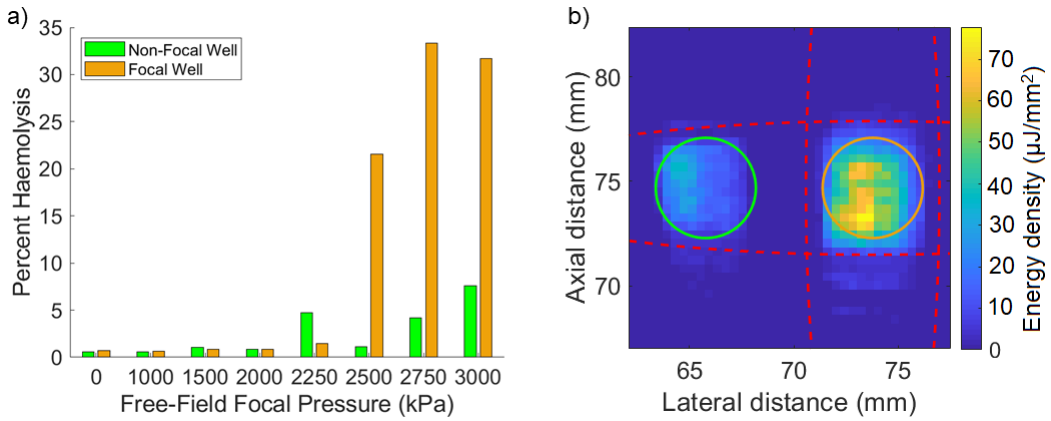

Figure 3.11: Agar phantom results. (a) Levels of haemolysis achieved at each pressure level in each well. (b) Passive acoustic mapping frame from a treatment. The focal and non-focal well locations are estimated by B-mode and marked by orange and green circles, respectively. The locations of the full width at half-maximum of the focal pressures for the two transducers are marked by red dashes. Obtained with (a) SonoTran Particles (1×10^{10} particles/mL) mixed with blood and (b) 3-MPa free-field focal pressure at 5000 cycles. Used with permission (Smith and Coussios 2020) (http://creativecommons.org/licenses/by/4.0/)

When the cavitation doses for each well and exposure were calculated a relationship was found that was comparable between the two wells, and was also comparable to the previously found data gathered using the Eppendorf based set-up (figure 3.12), finding that even a substantial change to the model used still had a limited effect on the relationship between haemolysis and the cavitation dose.

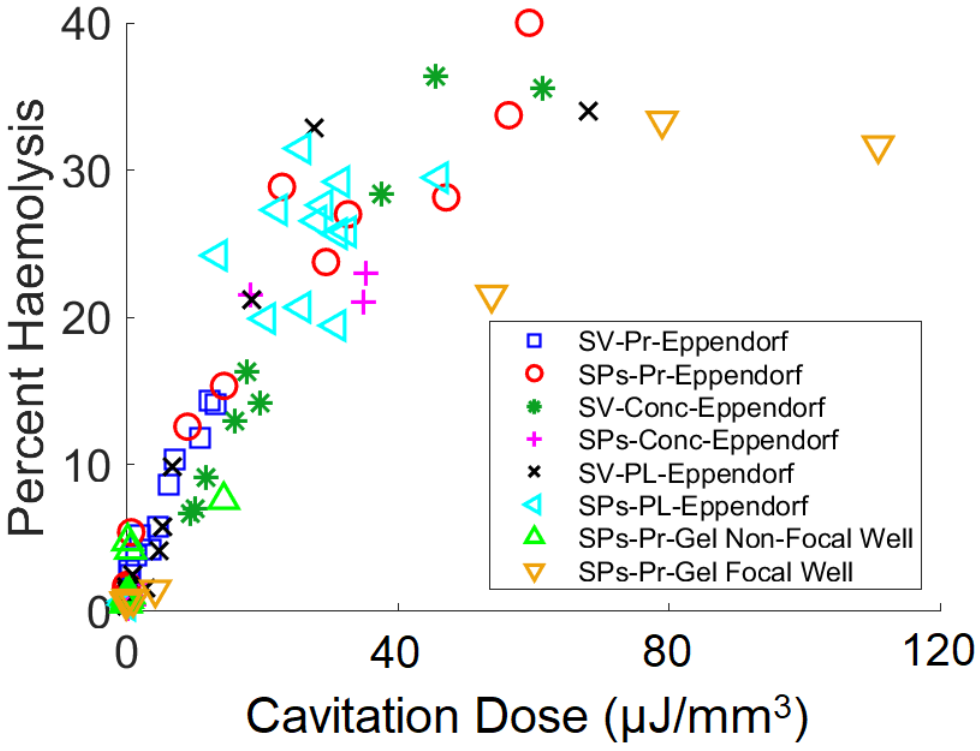

Figure 3.12: A relationship was found between cavitation and haemolysis that was additionaly comparable regardless of the model (Eppendorf tube or two-well gel model) used. Used with permission (Smith and Coussios 2020) (http://creativecommons.org/licenses/by/4.0/)

3.5 Discussion

The results of this study have a range of implications. Firstly, the fact that the extent of cavitation activity localized by PAM with a spatial resolution of 400 microns was confined to within the focal region and to within the boundaries of the Eppendorf tube that enclosed the cavitation nuclei confirms that PAM achieves high spatial specificity as a cavitation mapping tool for the parameters and set-up used.

PAM also allows for the tracking of the evolution of cavitation over time. Within the Eppendorf tube the PAM videos generated when SV microbubbles were used showed an initial increase in cavitation energy over time which then sharply dropped, which is in line with previous work done using PCD's (Hitchcock et al. 2011). One hypothesis as to why this could be the case is that initially the incident pressure field is shielded by bubbles closest to the transducers surface. Once these bubbles are

destroyed the incident focus becomes fully formed, able to generate higher pressures in the middle of the Eppendorf tube, accelerating the destruction of microbubbles in that central region. In the case of the sonotran particles, following the destruction of the few air bubbles within the solution cavitation then stabilises, maintaining exclusively inertial cavitation activity throughout the treatment (figure 3.9). These results match previous findings from the literature (Kwan et al. 2015b).

The relationship between cavitation dose and haemolysis found in this study appears linear at first (Figure 3.12), eventually plateauing in the range 30-40 % haemolysis. Complete, 100 % haemolysis is never achieved for a number of possible reasons. Firstly, given that the focal region of the therapeutic ultrasound only overlaps with a subset of the Eppendorf tube volume, with the – 6 dB ellipsoid of the focus covering approximately 40 % of the blood volume, not all red blood cells are exposed to cavitation simultaneously and there is continuous mixing due to microstreaming between acoustically exposed regions and quiescent regions. The second factor relates to the fact that over time, as red blood cells are gradually lysed, the mean distance between collapsing bubbles and adjacent red blood cells increases, making the destructive interaction between inertial cavitation and lipid membranes increasingly unlikely. Other effects could also be at play, including gradual microstreaming mediated transport of both red blood cells and cavitation nuclei out of the sample sub-volume that overlaps with the ultrasound focus. This is expected to result in a saturation and potential reduction of the haemolysis rate with increasing cavitation dose.

It is worth noting that the cavitation dose is integrated over the measured area and normalised by the total blood volume. In the case of the models studied here most of the total blood volume lies within the measured area i.e. most of the total blood volume is exposed to significant levels of ultrasound. This means that the cavitation dose and levels of haemolysis experienced by the blood is up to 40 %. However, if this experiment had been done in vivo the ratio between the measured area and the total blood volume would be significantly lower, as only a small sub-volume of the animal's blood is subjected to cavitation with every

ultrasonic pulse. As such in an in vivo model it would be expected that the average cavitation dose experienced by the blood (and thus the levels of haemolysis) would be significantly lower than those obtained in the experiments described here.

In the present experiment, red blood cells within the sample holder would have received 1.5 seconds (30 seconds at a 5 % duty cycle) of continuous ultrasound equivalent at a focal pressure in excess of 1 MPa, and 40 % of the total sample volume is exposed to cavitation on any one ultrasound pulse. In vivo, where flow velocities are on the order of cm/s, no single red blood cell is likely to be exposed to cavitation on two consecutive ultrasound pulses, and less than 5 % of the total murine blood volume of 1.5 ml lies within the focal volume on any pulse. For this reason, experiments seeking to measure cavitation-mediated haemolysis over the parameter range used in the present work in vivo have not yielded measurable values of free haemoglobin above background.

It is worth emphasizing that haemolysis in the context of the present work is caused intentionally in order to provide a metric of cellular safety, and the absolute values of haemolysis reported in the presence of microbubbles or other cavitation nuclei should therefore in no way be taken as indicative of the likely haemolysis values when using these agents in vivo.

The key finding of the present study was that the relationship between cavitation dose and haemolysis appears to be independent of the method by which the cavitation dose was generated, whether varying the applied pressure, pulse length, cavitation nucleation agent type or concentration. Unfortunately, it was not possible to reliably investigate the effect of varying the incident frequency over the course of the present study, because changing the frequency would also have changed the focal region size, thereby changing the fractional blood volume being haemolysed. A different experimental set-up would thus be required to accurately investigate the effects of changing the incident frequency alone.

Within the imitations of the present study, the proposed metric of the total energy of acoustic emissions (in Joules) integrated over the sensing volume nevertheless appears to have considerable predictive value and makes a strong case for the need

to acoustically calibrate PAM arrays on receive and adequately compensate for losses in the acoustic propagation path. This implies mechanistically that cavitation energy, as quantified by the energy of acoustic emissions, is what determines the level of haemolysis, regardless of how that energy is generated. The independence of the cavitation dose-haemolysis relationship on pressure, pulse length and local nucleation environment suggests that PAM could be used as a reliable safety monitoring tool in situations when some or all these parameters are unknown.

3.6 Conclusion

This work described in this chapter illustrates that PAM-derived cavitation dose strongly correlates with cellular safety. The relationship between spatiotemporal PAM-derived cavitation dose and haemolysis depended solely on the levels of cavitation energy generated, irrespective of the pressures, pulse lengths, cavitation nucleation agent type or concentration used to achieve a particular cavitation dose level. This potentially allows for a dramatic reduction in the parameter space that needs to be considered when relating cavitation to cellular safety. These results lay the groundwork for PAM-derived cavitation-dose metrics to be applied to other measures of safety, allowing for improved ultrasound monitoring of cavitation-based therapies.

4

Energy-Preserving Cavitation Imaging

Contents

4.1 Introduction

The results from the studies described in the previous chapters demonstrate that relationships can be found between the levels of cavitation as measured by PAM and the safety and efficacy of cavitation based therapies. However for these relationships to be useful it is critically important that the cavitation can be measured in an absolute and universal manner. There are multiple reasons for the importance of absolute cavitation measurement. It allows for the comparison of results between different research groups, and within the same research group across different

experimental set-ups. This could allow for the knowledge and understanding of different relationships between cavitation and therapeutic outcomes to interrelated and allow for a broader understanding of the biological effects of cavitation.

An essential step in absolute and universal measures of cavitation is accurate calibration of the receiving elements. Recent work has allowed for this (Gray, Lyka, and Coussios 2018), as well as for corrections of diffraction (Gray, Lyka, and Coussios 2018), attenuation (Gray and Coussios 2018), and array lens effects (Gray and Coussios 2019). Once all these corrections are taken into account, current PAM algorithms are able to generate accurate estimates of cavitation source strength at a given point. However, as will be demonstrated in the simulations conducted in this work, they generate grossly inaccurate estimates of the total cavitation energy over a treatment volume. In other words, the total cavitation energy present in PAM maps obtained with current algorithms does not accurately reflect the true energy radiated by the cavitation sources represented within it.

In this work a new version of the PAM algorithm is presented, which utilizes the Lucy-Richardson deconvolution technique to provide cavitation maps with reduced tail artefacts and accurate energy estimation over a volume in a computationally efficient way.

4.2 Lucy Richardson Deconvolution Passive Acoustic Mapping

The Lucy Richardson Deconvolution Passive Acoustic Mapping (LRD-PAM) algorithm attempts to resolve these issues in energy estimation and noise caused by the PSF by removing its effect. To do this it is assumed that the PSF of TEA-PAM is constant throughout the region of interest and is taken to be the PSF of the center of that region of interest. Under these assumptions the acquired image from PAM is therefore the convolution of the true source energies with this PSF (figure 4.1), and as such the effect of the PSF can be undone by performing a deconvolution of the acquired TEA-PAM image with the PSF for the set-up used, which can be easily generated through simulation. However, due to the presence of noise in the

acquired image and the fact that the PSF in fact does change if only to a small extent over the region of interest means that applying a conventional deconvolution process can introduce high levels of noise. In order to solve this problem, the Lucy Richardson Deconvolution process can be used (Fish et al. 1995; Lucy 1974; Richardson 1972; Biggs and Andrews 1997). The Lucy Richardson Deconvolution algorithm is an iterative technique derived from Bayes' theorem

$$P(x|y) = \frac{P(y|x)P(x)}{\int P(y|x)P(x)dx} \tag{4.1}$$

Where $P(x|y)$ is the conditional probability of event x given event y, $P(y|x)$ is the conditional probability of event y given event x which can be identified as the PSF centred at $\mathbf{x}$, $g(\mathbf{y}, \mathbf{x})$, $P(x)$ is the probability of event x which can be identified as the source distribution $f(\mathbf{x})$ (the ideal image that we are attempting to recover), and $P(y)$ is the probability of event y which can be identified as the degraded image $h(\mathbf{y})$ (the image that we originally obtain). From this one can derive the iterative algorithm

$$f_{i+1}(\mathbf{x}) = \int \frac{g(\mathbf{y}, \mathbf{x})h(\mathbf{y})}{\int g(\mathbf{y}, \mathbf{z})f_i(\mathbf{z})d\mathbf{z}} d\mathbf{y} f_i(\mathbf{x}) \tag{4.2}$$

Where i is the iteration number. Under isoplanatic conditions, then equation 4.2 can instead be written as

$$f_{i+1}(\mathbf{x}) = \left(\frac{h(\mathbf{x})}{f_i(\mathbf{x}) \otimes g(\mathbf{x})} \otimes g^*(\mathbf{x}) \right) \cdot f_i(\mathbf{x}) \tag{4.3}$$

Where division is element wise, $f_0(\mathbf{x}) = h(\mathbf{x})$, and $g^*(\mathbf{x})$ is the flipped PSF.

The algorithm iteratively generates a correction factor for each pixel, with the aim of converging towards the ideal estimate of the deconvolved image.

Following this deconvolution process the power values for each voxel correspond not to the spatial average power density over the voxel volume, as is the case for TEA and RCB PAM, but instead to the total power experienced by the voxel volume. The power of each voxel is therefore divided by the voxel size to give a final PAM map in terms of power density with units of power/volume.

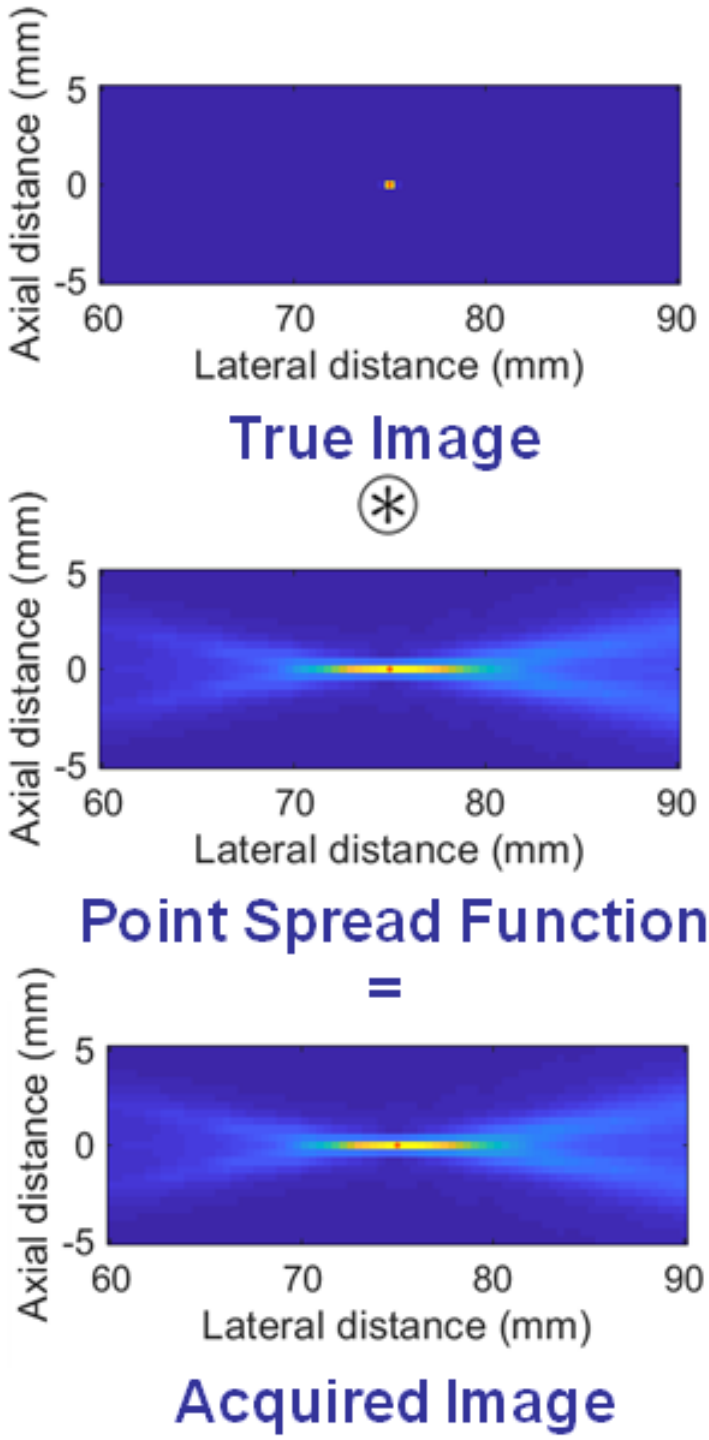

Figure 4.1: The images acquired in Passive Acoustic Mapping (PAM) can be thought of as being generated by convolving the true image containing an acoustic source at a point (in red) by the point spread function. As such by deconvolving the acquired image with the point spread function with the Lucy-Richardson method, one can produce an estimate of the true image.

Ideally, 3D PAM would be implemented to enable full capturing of sources of acoustic emissions throughout the entire treatment volume. In this case in order to generate an estimate of the total cavitation energy occurring within the treatment volume, one would simply need to integrate the power density from the 3D LRD-PAM over the treatment volume and over the duration of the treatment time.

If 3D PAM is not possible, assumptions then need to be made about how representative cavitation activity occurring within the field of view of the 2D PAM map is of cavitation activity outside the field of view. In a well-conditioned experimental setup where the array is positioned so as to overlap with the regions of highest probability of cavitation activity, it is common to assume that no cavitation activity occurs in the portion of the treatment volume outside the array field of view and so the 2D slice is assumed to contain the totality of the cavitation energy and be a 2D projection of the relevant 3D space. In this case, the deconvolution in LRD is 2D, and so then needs to be divided by the pixel area to generate the 2D power density (power/area). Then in order to estimate the total cavitation energy one must integrate over the area of interest and over the treatment duration time.

4.3 Numerical Simulations

In order to evaluate the new algorithm a series of simulations were conducted for a single L7-4 linear array, acquiring signals from bubble(s) located approximately 75 mm away in the center of the array aperture. The bubble signals were generated using the Keller-Miksis equation (Johansen, Song, and Prentice 2017; Keller and Miksis 1980) (equations 1.48 1.49 1.50). The parameters used to generate the signals using the Keller-Miksis equation can be found in table 4.1 and were chosen to be representative of experimental conditions typically used in the context of cavitation-enhanced drug delivery for cancer (Carlisle et al. 2013).

Parameter	Value
R_0	$3\mu m$
f	0.5 MHz
P_{neg}	2 MPa
r	75 mm
SNR	100

Table 4.1: Parameters used as part of the Keller-Miksis simulation to generate bubble signals used during numerical simulations testing the beamforming algorithms.

The original estimate of the PSF of the TEA-PAM algorithm used in the LRD-PAM algorithm was generated by beamforming a 25 μs long signal consisting of a single, one sample long (0.05 μs) spike occurring one sample (0.05 μs) after the beginning of the signal (sampling frequency 20 MHz). This signal was then beamformed using the frequency domain TEA-PAM algorithm (Haworth et al. 2017) in the 3 – 7 MHz range, as this is the usable frequency band of an L7-4 linear array. The image generated is then normalized by the energy of the signal such that the magnitude of the PSF maxima is 1.

The numerical simulations that were run fall broadly into two categories. The first set were conducted in order to determine the number of iterations of the Lucy-Richardson algorithm to be used in the second set of simulations where the strengths and limitations of the algorithm are compared against the two most commonly used alternatives, TEA and RCB PAM.

4.3.1 Number of Iterations Optimisation

In order to optimize the number of iterations used as part of the Lucy-Richardson deconvolution a series of simulations were conducted whereby a single point source was moved axially across a 20.1 mm lateral by 60.4 mm axial area of interest (0.1 by 0.4 mm pixel size) centred in the middle of an L7-4 linear array with the central point of interest occurring 75 mm away. At each location the error in location estimation (where the location estimated by PAM was determined as the location of maximum intensity within the PAM map) was estimated over a variety of iteration numbers. The results of these simulations can be seen in figure 4.2. It was found

that a compromise must be made when choosing the number of iterations. As the number of iterations increases, the FWHM of the LRD-PAM map decreases (figure 4.2a-d). However, due to a combination of the incorrect assumption that the PSF is constant throughout the PAM map and the non-negligible energy values of the PSF found at the edges of the region of interest, an error can be found in the estimation of the location of sources as calculated by LRD-PAM. This is an error that does not exist for TEA or RCB-PAM imaging. The effect of this error is that energy is more likely to be estimated as originating from towards the center of the PAM map. Figure 4.2e describes the relative positional error defined as ((Estimated Location – True Location)/Half the imaging FWHM). As in this example the axial dimension was being explored the axial FWHM was used. The positional error is a function of both the true position of the source within the region of interest and the number of iterations. This error is strongest slightly offset to the center of the PAM map and at high numbers of iterations, as well as being quasi-linearly related to the FWHM of the PSF, leading to the error being substantially worse in the axial than the lateral direction. However, if the number of iterations remains at 10 or below this location error remains below a quarter of the FWHM within the central two thirds of the region of interest (figure 4.2f). For reference in the case of the use of an L7-4 linear array positioned 75 mm away from the center of the region of interest this would correspond to a worst case error of roughly 2 mm axially and 0.12 mm laterally. For most applications where this error corresponds to the PAM pixel size this corresponds to a worst case scenario of an error estimation that remains within one PAM pixel. As such for all simulations described in this work from here on the number of iterations was chosen to be 10.

4.3.2 Performance assessment of the LRD-PAM algorithm

Accuracy of energy estimation

In order to explore the ability of LRD-PAM to generate accurate estimates of cavitation energy a series of simulations were conducted whereby a varying number of simulated bubbles were placed uniformly randomly within a 4 mm square area

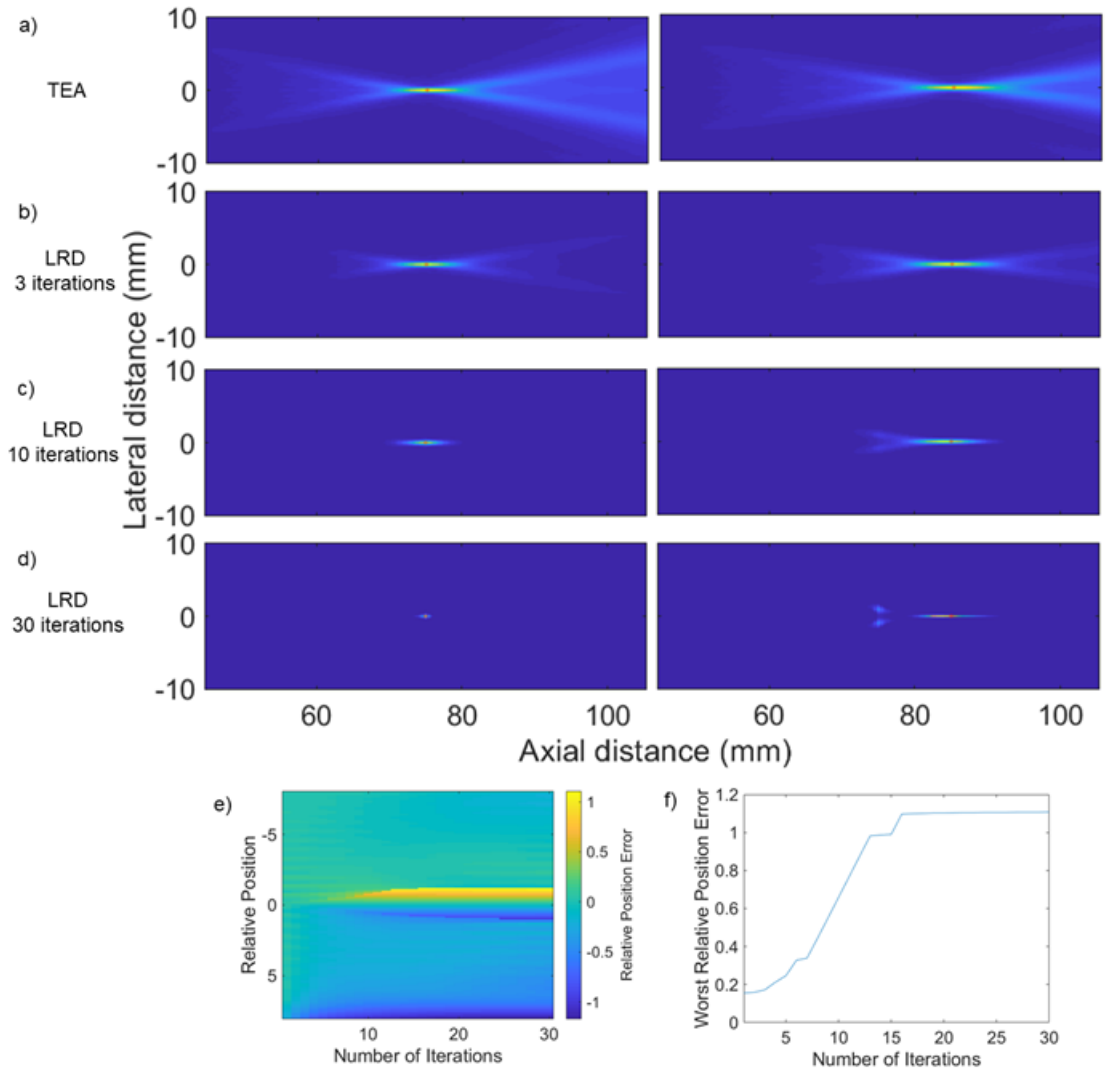

Figure 4.2: a) a map generated by time exposure acoustics (TEA) passive acoustic mapping (PAM) of a single acoustic source placed in the center of the region of interest (Left) or 10 mm axially further (Right). b-d) the same received signals mapped using the Lucy-Richardson Deconvolution (LRD) PAM algorithm using 3, 10, and 30 iterations respectively. e) the dependence of the location estimation error of the LRD-PAM algorithm and how it varies with the position of the acoustic source within the region of interest centered at 0 relative to half of the full width half maximum of the TEA-PAM algorithm at the center of the region of interest. f) the worst relative position error of the LRD-PAM algorithm within the central 2/3rds of the region of interest.

centered in the lateral middle of a L7-4 linear array placed 75 mm away, centered in the same location of the PAM field of view of 10 mm lateral by 30 mm axial size with 0.4 mm square pixel size. Frequency domain TEA-PAM and RCB-PAM (with $\epsilon = 0.0001$) were implemented in the range of 3 to 7 MHz, which was found to be optimal for the simulations conducted. Note that this small value of ϵ can only

be used because the locations and calibrations of the acoustic detectors is perfect due to the simulated nature of the data. The cavitation energy was estimated by integrating the power density maps over space and time to estimate the total energy of acoustic emissions. The results of these simulations can be seen in figure 4.3.

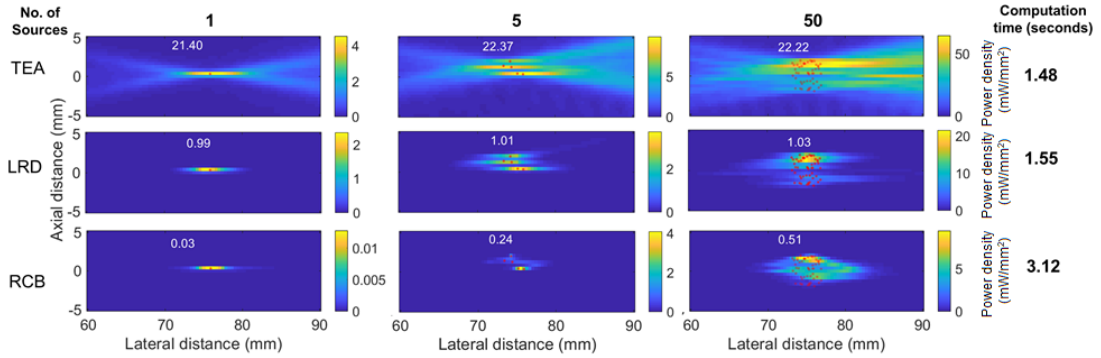

Figure 4.3: Example passive acoustic mapping (PAM) maps generated by the time exposure acoustics (TEA), Lucy-Richardson deconvolution (LRD) and robust Capon beamformer (RCB) algorithms with a varying number of sources (red dots) placed uniformly randomly within a 4 mm square central region. The white text relates to the ratio between the estimated and true total energies in each case, with the average computation times for the three algorithms shown on the far right.

As can be seen, the LRD and RCB PAM algorithms both do significantly better at reducing noise outside of the regions where cavitation is taking place than TEA-PAM and are able to do this consistently with the increasing number of sources. The white numbers correspond to the energy estimates (the estimated total energies divided by the true total energies in each case). TEA-PAM gives a consistent and extreme overestimation of the total energy regardless of the number of sources present. The consistency of the overestimation means that based on the PSF a constant could be applied to correct the for the energy error and bring the energy estimation of TEA to be roughly in line with LRD, however the high noise and large PSF FWHM would still be present in the TEA images, which could lead to energy estimation errors if the energy within a relatively small volume was investigated. RCB-PAM gives an underestimate of the total energy that varies depending on the number of sources, due to the varying ability of the optimization algorithm to reduce noise with different signal complexities. LRD-PAM is capable of consistently generating accurate estimates of the total energy regardless of the

number of sources present within the ranges that have been explored of 1 to 500 sources (only 1 to 50 shown for presentation reasons).

Computational efficiency

The average computation time using code not optimized for computational efficiency written in MATLAB running on a computer with an Intel Xeon W-2145 CPU, and 32 GB 2666 MHz RAM, was found to be 1.48 seconds per frame for TEA, 1.55 seconds per frame for LRD, and 3.12 seconds per frame for RCB. While the absolute computation time varies based on hardware, signal length, pixel size, region of interest size, and many other factors, for all simulations run within this study LRD showed a minor increase in computation time over TEA with RCB taking considerably longer. As such LRD can produce PAM maps of similar noise reduction over TEA to the RCB algorithm and provide improved energy estimation over both TEA and RCB with only a minor increase in computation time over the TEA algorithm.

It has recently been shown that the computational efficiency of TEA can be highly reduced through parallelisation and GPU processing (Kamimura et al. 2020; O'Reilly, Jones, and Hynynen 2014; Jones, O'Reilly, and Hynynen 2015). While these same methods can be applied prior to the deconvolution step in the LRD algorithm, due to the serial iterations used in the Lucy-Richardson algorithm the deconvolution step does not lend itself as easily to parallelisation based computational improvements. However, as the increased computational cost of LRD over TEA was at worst on the order of 100 ms in the simulations conducted even using non optimised code, this is unlikely to lead to significant restrictions in real time implementation.

Effect of pixel size

In order to explore the robustness of LRD-PAM in estimating cavitation energy with varying pixel size a series of simulations were run whereby a single point source placed in the center of a 20 mm lateral by 60.8 mm axial area of interest (0.1 by 0.4 mm standard pixel size) centered in the middle of an L7-4 linear array with the central point of interest occurring 75 mm away. The PAM reconstruction

was repeated with a pixel size multiplier between 27 and 1/27 being applied to investigate how pixel size affected the energy estimate of the algorithm. The results of these simulations can be seen in figure 4.4. As the pixel size decreases the energy estimates of all the algorithms converge, with energy estimates decreasing at larger pixel sizes. Of the three only LRD converges at the true energy, maintaining high levels of accuracy until a point is reached where the pixel size becomes too large and the energy estimated becomes an underestimate.

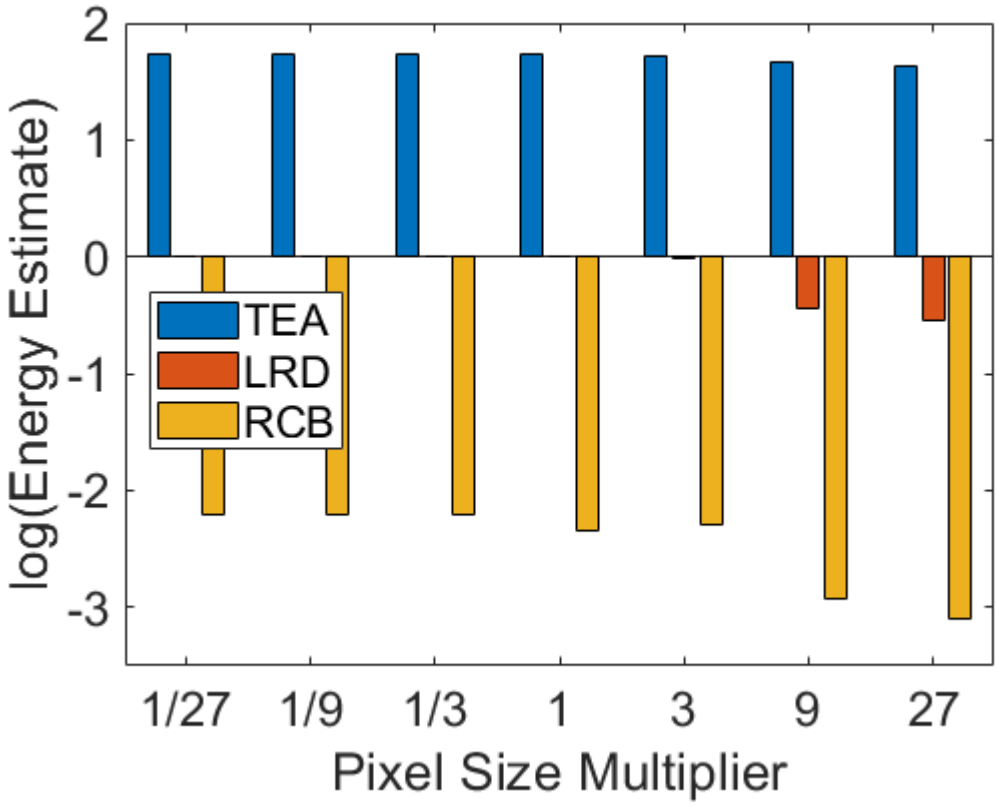

Figure 4.4: The variation in the log of the energy estimate of a single acoustic source, with the pixel sizes being changed by a multiplier for the time exposure acoustics (TEA), Lucy-Richardson deconvolution (LRD), and robust Capon beamformer (RCB) algorithms.

Effect of axial and transverse source position

A series of simulations was additionally run to explore the variation in energy estimation with source location. A single point source was moved axially across the entirety of a 20.1 mm lateral by 60.4 mm axial area of interest (0.1 by 0.4 mm pixel size) centered in the middle of an L7-4 linear array with the central point of

interest occurring 75 mm away. At each location the error in energy estimation is calculated. The results of these simulations can be seen in figure 4.5. As can be seen in the case of all three of the algorithms the estimation in energy varies with source location, with the energy estimate decreasing with distance in the case of TEA and LRD and increasing with distance in the case of RCB. In the case of TEA this change in energy estimation is due to the fact that the energy distal to the point is greater than the energy proximal to the point in the PSF, and therefore the energy estimates are higher the more proximal the point source is, as more proximal sources have more of the higher energy tail within the PAM field of view. This effect bleeds over into the LRD algorithm, as errors due to the false assumption that the PSF does not vary within the field of view leads to the same type of errors as TEA however with a much-reduced effect. It is hypothesised that the reason why this error does not appear to be present in the multiple source simulations conducted (even when the spread of the sources is wide), is that the combination of over and underestimation of the individual source energies cancel each other out when estimating the total energy caused by all the sources, though further work would be required to confirm this. It is important therefore when using the LRD-PAM algorithm to attempt to place the center of the field of view in the center of the cavitation activity, though this is sensible regardless of the presence of this artefact. Additionally, it is worthy of note that the energies estimated by the LRD algorithm are independent of the number of iterations used. In the case of the RCB algorithm it is suspected that the increase in energy with distal sources is due to the increase in PSF size of PAM with axial distance (equation 7), and that this effect outweighs the effect of the tail energy which is suppressed compared to TEA, though further simulations would be needed to validate this theory.

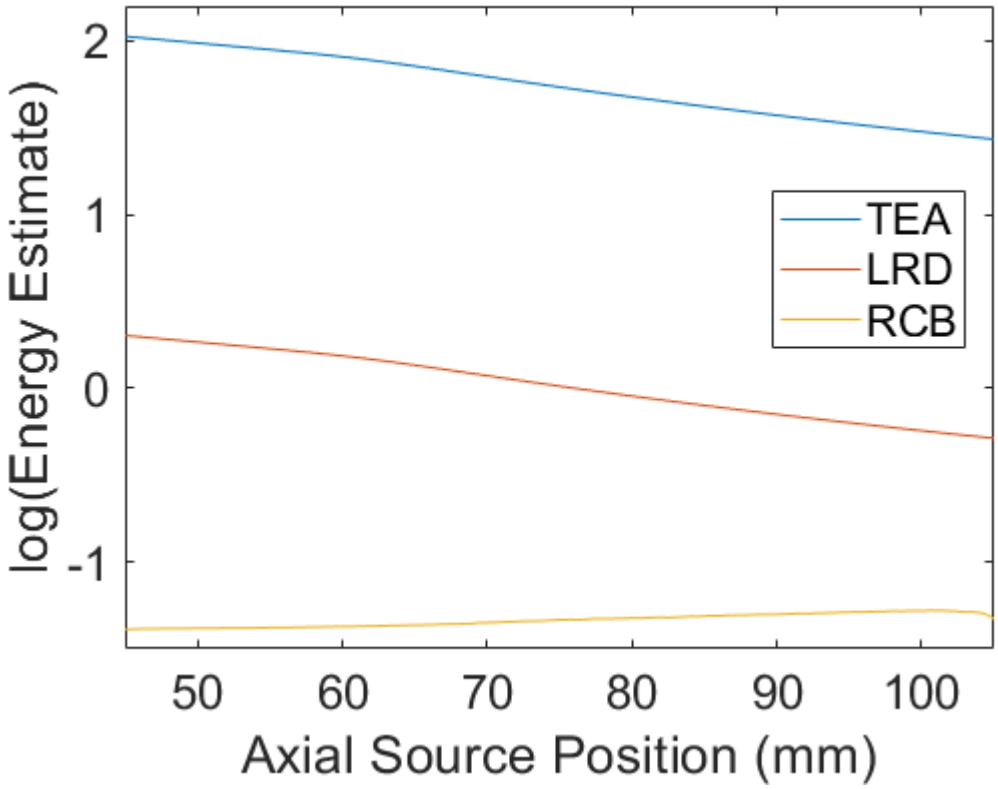

Figure 4.5: The variation in the log of the energy estimate of a single acoustic source, with the pixel sizes being changed by a multiplier for the time exposure acoustics (TEA), Lucy-Richardson deconvolution (LRD), and robust Capon beamformer (RCB) algorithms.

4.4 Experimental Methods

The next step was to experimentally validate the LRD-PAM algorithm. In order to do this, an experiment was conducted whereby two perpendicular and co-planar L7-4 linear arrays (L7-4, Verasonics, Kirkland, WA, USA) were positioned at roughly 75 mm from the center of the focus of a 0.5 MHz center frequency therapeutic transducer (H-107 D SN12; Sonic Concepts, Bothell, WA, USA) with active diameter 64 mm and a focal length of 62.6 mm (figure 4.6a). The set-up was placed in a large tank of de-ionized and partially degassed water. The pressure was then slowly ramped up until a single 50 cycle pulse generated a cavitation event roughly 50 % of the time (this corresponded to 1.75 MPa peak rarefactional pressure). The data was collected using a Verasonics Vantage Research Ultrasound System (Vantage, 256; Verasonics) and saved on a computer for post processing. The

arrays used were calibrated with a substitution calibration using wire scattering (Gray, Lyka, and Coussios 2018), this allowed for the conversion of the received electrical energy into acoustic energy of the source.

PAM maps were generated of the data using the TEA, LRD, and RCB ($\epsilon = 5$) algorithms in a 25 mm square region of interest with pixel size 0.2 mm square. Data was selected where only a single cavitation event took place, as determined by only a single location of cavitation being detectable using TEA, LRD, and RCB PAM. These data were then processed in three ways, firstly with only using data collected using one of the two arrays, secondly with only using data collected using the second array, and thirdly using data collected with both arrays simultaneously. These pieces of equipment have three different PSF's (figures 4.6b-d), and while the true energy of the acoustic sources recorded are unknown, fundamentally the same data processed in three different ways should give the same estimate of source location and energy. As such, the robustness in energy estimation of the TEA, LRD, and RCB algorithms can be explored by observing the similarities and differences between the energies estimated by the three processing techniques.

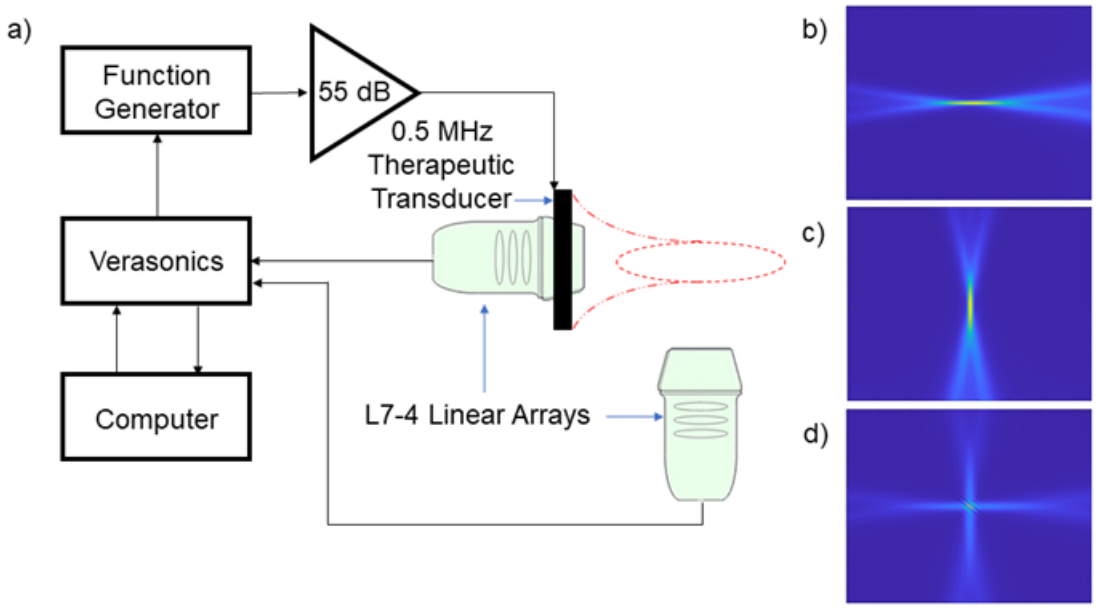

Figure 4.6: a) The experimental set-up with cavitation caused by a ramping pressure in deionized and partially degassed water recorded using two perpendicular and co-planar L7-4 arrays. b-d) the point spread functions of the first, second, and both arrays combined respectively as found by the time exposure acoustic passive acoustic mapping algorithm.

4.5 Experimental Results

A sample set of PAM maps can be seen in figure 4.7 All algorithms showed perfect agreement on all source locations for all three processing methods, as such keeping the number of iterations at 10 removed any perceivable errors in location estimation. It can also be seen qualitatively that the LRD algorithm achieves a similar level of noise reduction as the RCB algorithm.

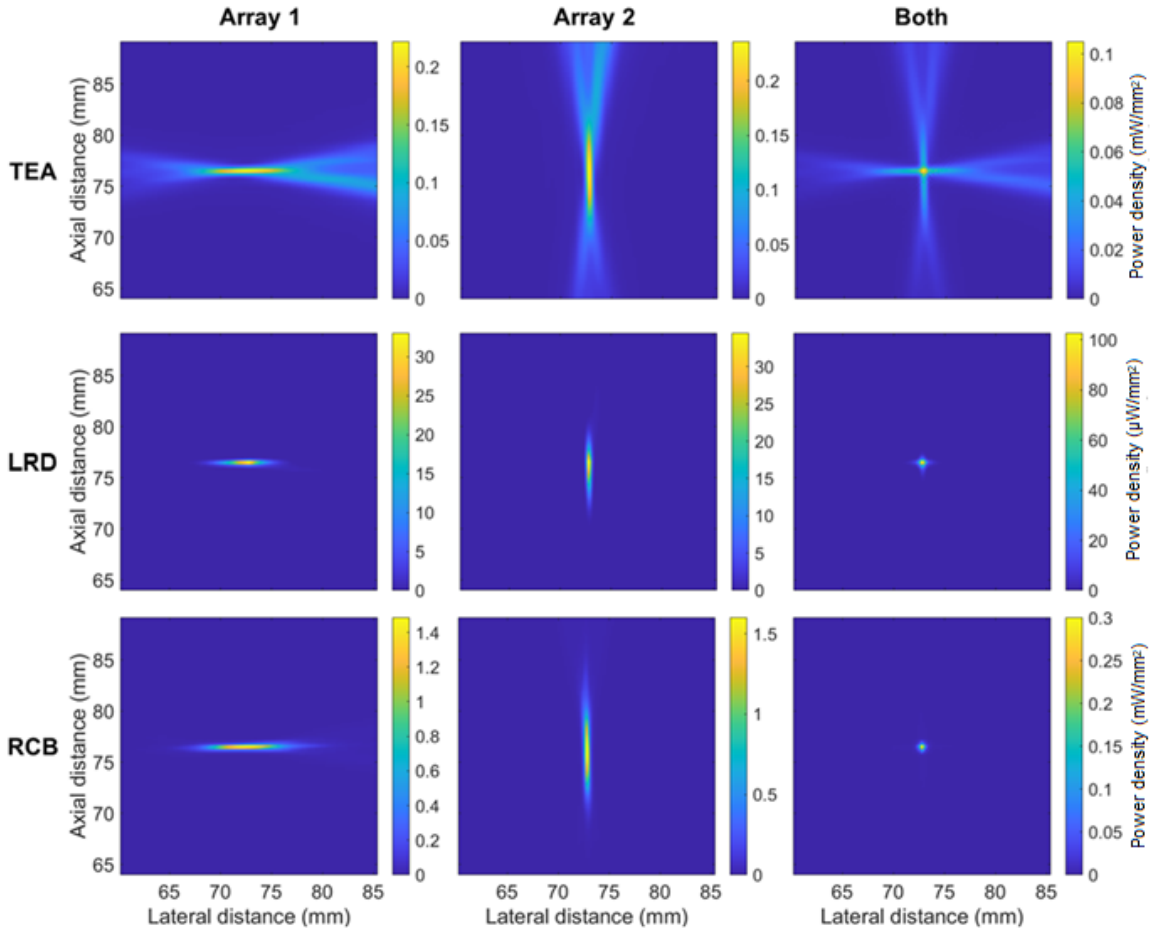

Figure 4.7: Example passive acoustic mapping images generated by the time exposure acoustics (TEA), Lucy-Richardson deconvolution (LRD), and robust Capon beamformer (RCB) algorithms, all maps are of the same acoustic signals using data recorded by one array, the other array, or both arrays.

Unlike the modelling case where the source energy was known, this is not the case for these experiments. In order to assess the robustness of energy estimates, a comparison was therefore performed between the energy estimation for a single receiving array vs a dual receiving array and between the two single arrays for each

of TEA, LRD and RCB. The algorithm that is most energy preserving and set-up independent should tend towards a single to dual-array ratio of 1 (figure 4.8). In the case where the energy estimates are compared between the two individual single arrays with similar but rotated PSFs it is found that all three of the algorithms show similar levels of agreement in energy estimates.

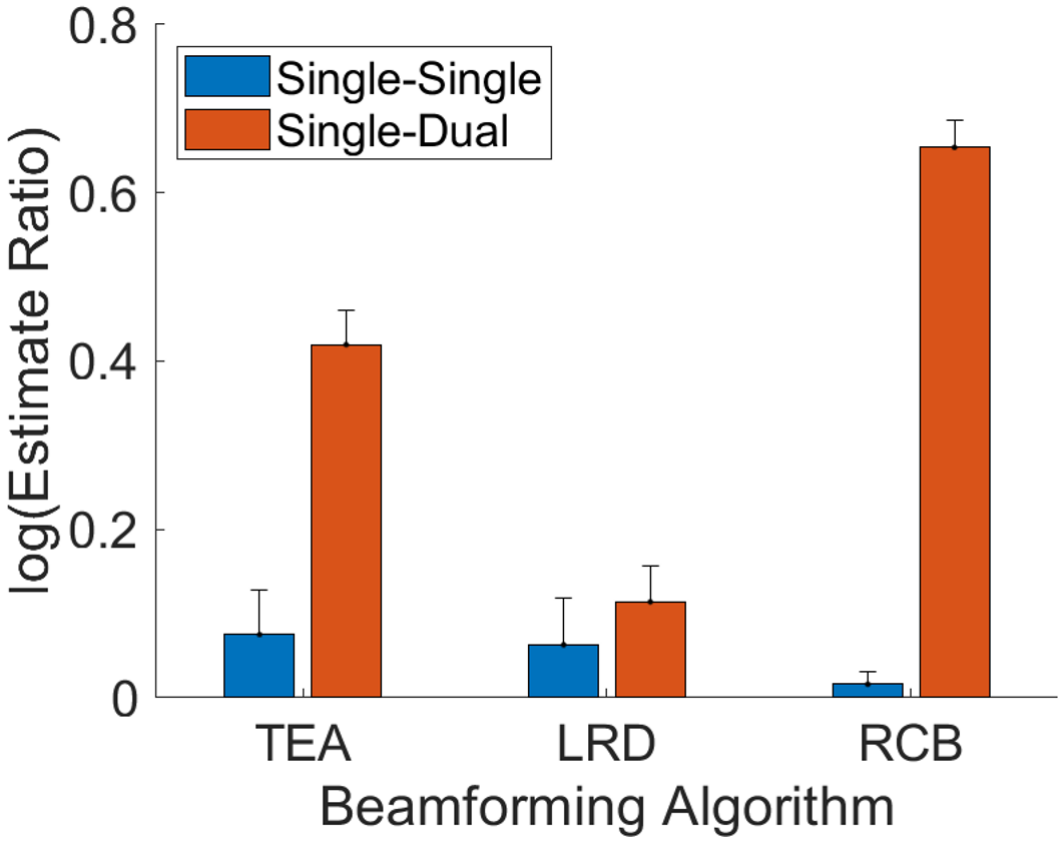

Figure 4.8: The discrepancy in the estimations of the total energy between using data from one array vs data from the other array (blue) or data from one array vs data from both arrays simultaneously (red) for the time exposure acoustics (TEA), Lucy-Richardson deconvolution (LRD), and robust Capon beamformer (RCB) algorithms.

When the energy estimates generated by the single arrays are compared to the energy estimates generated by using the full dataset of both arrays, the substantial change in PSF causes a large discrepancy in energy estimation to occur in the case of both TEA and RCB PAM. This effect is significantly reduced in the case of the LRD-PAM algorithm, therefore allowing for truly set-up independent energy estimates to be gathered even in cases with significantly different array apertures.

4.6 LRD Cellular Safety Analysis

In order to explore the ability of LRD to handle experimental data with multiple acoustic sources, the dataset gathered in chapter 3 was re-processed using the LRD-PAM algorithm. Looking at the PAM maps generated by LRD compared to RCB in figure 4.9, it can be seen that for both algorithms the energy is contained within the eppendorf.

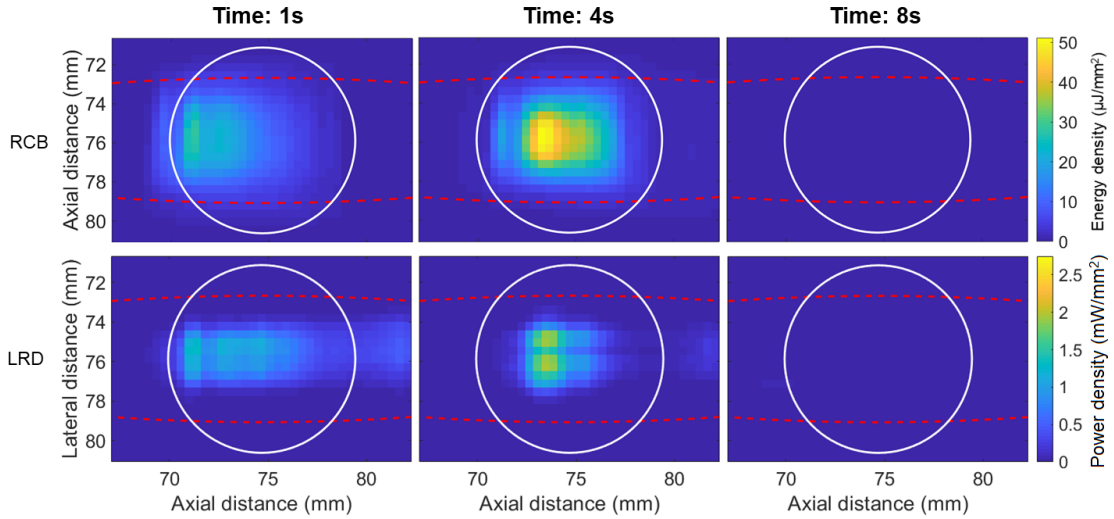

Figure 4.9: Frames from the passive acoustic mapping videos of the treatments. The location of the Eppendorf tube wall was estimated by B-mode, and is marked by a white circle. The location of the full width at half-maximum of the focal pressure was estimated using B-mode of a hydrophone tip placed in the centre of the focus, and is marked by a red dashed oval. Top: Processed with the RCB algorithm. Bottom: Processed with the LRD algorithm. Obtained with SonoVue (SV, 1×10^5 microbubbles/mL) mixed with blood, 2 MPa, 5000 cycles.

When the cavitation doses are calculated a relationship can be found between haemolysis and cavitation dose that is similar to that generated by RCB (figure 4.10). The cavitation dose is defined as the integral of the PAM power density map over the measured area and normalised by the treated volume, and relates to the energy density experienced by the blood. Interestingly however the relationship appears to be remain straighter throughout the distribution when compared to the results as generated by RCB. Further work will be required to investigate which of the two methods produce a more accurate representation of the underlying reality.

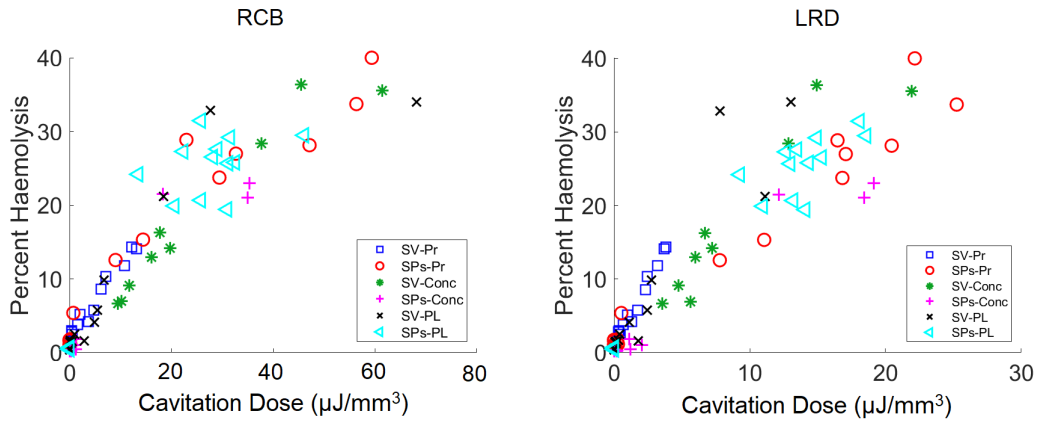

Figure 4.10: Correlation between Cavitational Energy Density and Haemolysis using the Lucy-Richardson Deconvolution Passive Acoustic Mapping Algorithm (right) and the Robust Capon Beamforming Algorithm (left, replicated from chapter 3).

When the two-well data is reprocessed it can be seen again that energy is contained within the well. Additionally cavitation energy that is determined by RCB to occur at the edge of the well inside the agar phantom is determined by LRD to occur inside the well itself (figure 4.11)

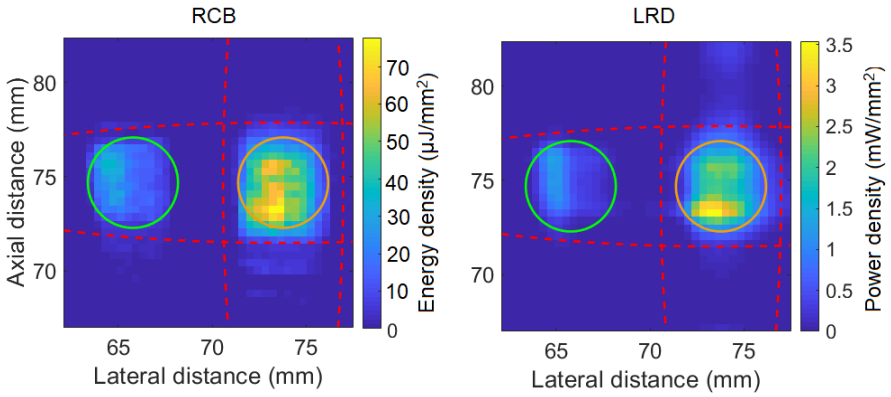

Figure 4.11: Passive acoustic mapping frame from a treatment, processed using RCB and LRD PAM. The focal and non-focal well locations are estimated by B-mode and marked by orange and green circles, respectively. The locations of the full width at half-maximum of the focal pressures for the two transducers are marked by red dashes. Obtained with SonoTran Particles (1×10^{10} particles/mL) mixed with blood and 3-MPa free-field focal pressure at 5000 cycles.

When the cavitation dose are determined for the two-well data a slightly different relationship appears between the cavitation dose and haemolysis in the case of the two-well data and in the case of the eppendorf data (figure 4.12. This distinction does not appear to be as strong in the case of the RCB processed data.

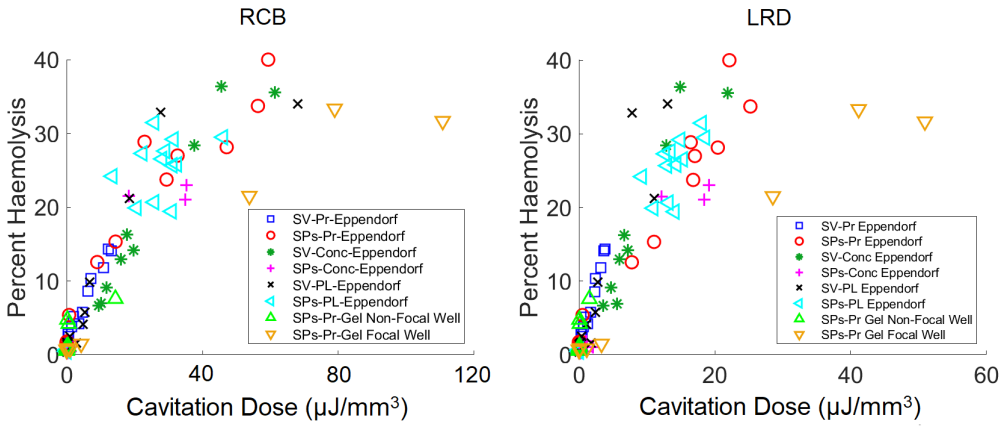

Figure 4.12: A relationship was found between cavitation and haemolysis as determined by Lucy-Richardson Deconvolution (right) and Robust Capon Beamforming (left, replicated from chapter 3).

There are many potential reasons for this difference, one of which is that in the two-well experimental set-up, cavitation occurred within the agar at the edge of the wells. As LRD has a slight bias in localising energy towards the center of the map, it is possible that the LRD incorrectly allocated cavitation energy occurring within the agar as occurring within the blood. Some evidence for this theory exists in the fact that if the RCB data is re-analysed such that the segmentation is more lax, with a 0.4 mm (one pixel) increase in radius taken as part of the cavitation dose calculation, the result can be seen in figure 4.13.

As can be seen, when RCB considers cavitation occurring within the edge of the agar as occurring within the blood, then both LRD and RCB suggest a subtly different relationship between cavitation dose and haemolysis in the case of the Eppendorf and well set-up. This suggests that the discrepancy between the Eppendorf and well data could be due to to cavitation within the agar being incorrectly attributed to the blood.

Another potential reason for this discrepancy between the Eppendorf and agar well data lies with acoustic shielding. Acoustic shielding, especially caused by the cavitation emissions which pass from the focal well through the non-focal well to reach the receiving array, can have a marked effect on the true point spread function of the image. If the point spread function differs greatly from the estimated

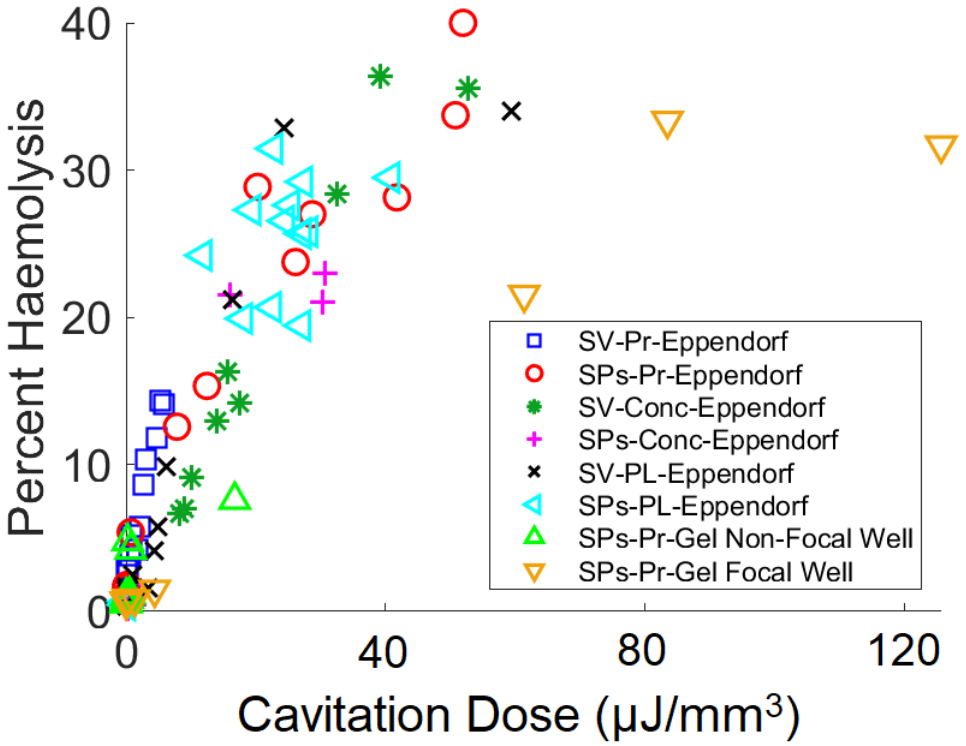

Figure 4.13: A relationship was found between cavitation and haemolysis as determined by RCB, generated by segmenting cavitation occuring both within the eppendorf/well and in the 0.4 mm (one pixel) around.

point spread function given to the LRD algorithm then this could lead to errors in energy estimation and localisation.

Finally, if a subsection of the data is reprocessed using data only from one of the linear arrays and compared to the data as determined by both arrays (figure 4.14) a strong discrepancy can be found between the two different set-ups when processed using RCB, which is significantly reduced when processed using LRD. This demonstrates that even in an experimental case involving a significant amount of cavitation, the cavitation energy estimates as determined by LRD remain far more consistent than those determined by RCB. The remaining discrepancy between the one and two array cases when processed using LRD are likely due to a combination of acoustic shielding and uncertainty in array calibrations.

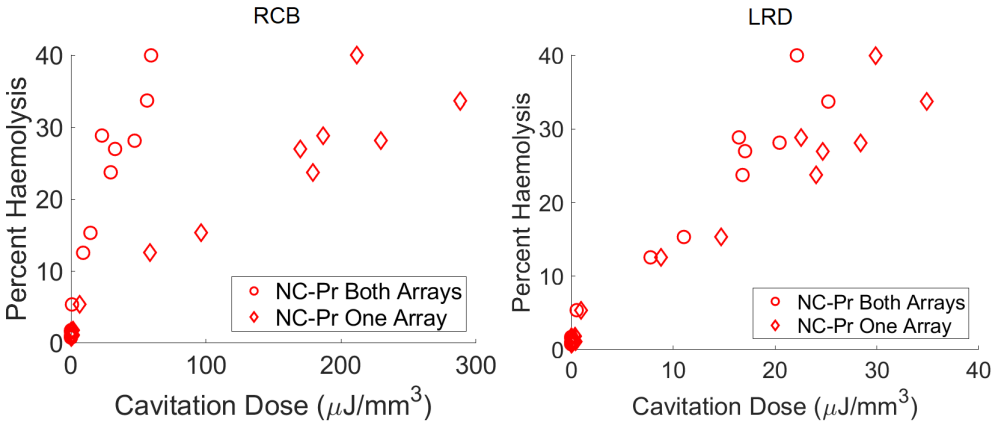

Figure 4.14: A comparison between the relationship found between cavitation and haemolysis as determined by Lucy-Richardson Deconvolution (right) and Robust Capon Beamforming (left) when processed using data from one array or both arrays.

4.7 Conclusion

The LRD-PAM algorithm is able to provide a significant reduction to the noise present in TEA-PAM imaging, achieving similar image quality to RCB-PAM. This is achieved with only a minor increase in computation time over the TEA algorithm, and a significant reduction in computation time compared to the RCB algorithm. As such the LRD-PAM algorithm could be utilised as a way of producing RCB quality images with TEA levels of computation cost. The LRD-PAM algorithm additionally provides volumetric energy estimates that consistently are in far closer agreement to the true energy of simulated acoustic emitters when compared to the TEA or RCB algorithms, as well as providing consistent energy estimates between different set-ups in experimental conditions. Taken together, these results demonstrate the potential of the LRD-PAM algorithm as a computationally fast technique for energy preserving real-time cavitation monitoring.

5 Conclusions and future work

5.1 Initial Overall Aims

The overall aim of this thesis was to develop a quantitative, set-up independent, and computationally efficient means of monitoring cavitation activity during therapeutic ultrasound, and to demonstrate the potential of this technique in monitoring the safety and efficacy of cavitation-mediated therapies. Chapter 2 explores Passive Acoustic Mapping as a quantitative tool for monitoring the efficacy of cavitation-mediated drug delivery. Chapter 3 explores PAM as a means to monitor the safety of cavitation-mediated therapies over a wide range of therapeutic parameters. Finally Chapter 4 shows work on developing a set-up independent, energy-preserving, and computationally efficient version of the PAM algorithm.

5.2 PAM Monitoring of Cavitation-Enhanced Immunotherapy (Chapter 2)

The results of this chapter show evidence in tumour models that cavitation dose correlates quantitatively to drug delivery. It is therefore not surprising that when cavitation is used in an attempt to enhance the delivery of an immunotherapeutic that the cavitation dose also correlates with an improvement in therapeutic outcome, and that the correlation follows through to a relationship between cavitation dose

and an immunological response. What is surprising is that even in the absence of an active immunotherpautic agent a correlation is still found between the cavitation dose, the immunological response, and improved treatment efficacy. This strongly suggests that an immunological and therapeutic effect of cavitation alone is at least in part responsible for these enhanced therapeutic outcomes.

The main limitations of this chapter are due to the retrospective nature of the analysis. Using this retrospective approach provided access to an unprecedented amount of *in vivo* data points, making it possible to perform the analysis over large 'n' numbers. However, the experimental design of the original study involved two groups for each drug, one receiving no ultrasound, one receiving an ultrasound treatment. As a result, the cavitation dose for about half the mice was zero, while the cavitation dose received by the remaining mice was not evenly distributed across the range of cavitation doses encountered. The same limitation also applies to the gene expression and drug delivery analysis. A different study design, where the cavitation dose is deliberately varied, and evenly spaced across the entire range of interest, would make it possible to develop and validate a predictive model as a first step towards clinical translation by allowing for an improved estimate of the relationship between efficacy and cavitation dose with a similar sample size. This would be used to develop and validate a predictive model which would assist in the clinical translation of this work.

Cavitation monitoring is also affected by some limitations. Due to memory limitations only approximately 0.15% of the acoustic signal produced with each pulse could be recorded, which forced us to assume that the average power estimated within this time window is representative of the average power of the entire pulse. While this is reasonable assumption for the cavitation agent used in this study, using a longer sample of each pulse could lead to a more accurate estimation of the levels of cavitation generated. Additionally, due to a lack of recorded B-modes in the survival and gene expression studies we were also forced to assume that all cavitation recorded occurred within the tumour. This is more likely to be a poor assumption given the results of the drug delivery study. Collecting B-modes could have allowed

for the use of exclusion methods which may have revealed a different relationship between the cavitation dose and survival. Another limitation is that the cavitation dose estimate is taken as an average over the entire duration of the treatments and the entire volume of the tumour. The spatiotemporal distribution of cavitation within the tumour may affect the response to the treatment, which is something that this study was not able to explore. It is suspected that a combination of these factors which lead to the size of the confidence intervals in the results, and that with improvements in monitoring this uncertainty could be greatly reduced, improving the therapy modelling and clinical utility. In spite of these limitations, retrospective analysis of PAM data demonstrated considerable potential for predicting both mechanistic effects (enhanced drug delivery) and improved therapeutic responses, therefore adequately motivating the remainder of the thesis.

5.3 Monitoring the Cellular Safety of Cavitation Based Therapies by Passive Acoustic Mapping *in vitro* (Chapter 3)

In line with the original objective of investigating whether PAM can serve as a predictor of treatment safety, Chapter 3 set out to investigate the correlation between PAM-derived cavitation dose and a simple indicator of cellular safety, haemolysis. The relationship between spatiotemporal PAM-derived cavitation dose and haemolysis was found to depend solely on the levels of cavitation energy generated, irrespective of the pressures, pulse lengths, cavitation nucleation agent type or concentration used to achieve a particular cavitation dose level. This potentially allows for a dramatic reduction in the parameter space that needs to be considered when relating cavitation to cellular safety. Future work will be needed to explore whether this parameter independence extends to the relationships between cavitation dose and other bioeffects. These results lay the ground-work for PAM-derived cavitation-dose metrics to be applied to other measures of safety, allowing for improved ultrasound monitoring of cavitation-based therapies.

There are several limitations to this study that would benefit from further exploration. Firstly there are the memory limitations similar to the previous chapter, though in this case care was taken to maximise the available cavitation data, with 5 % of the acoustic signal being recorded.

In this study only anuclear cells were explored. An interesting question to explore would be to what extent (if any) does the relationship between cavitation dose and haemolysis extend to the relationship between cavitation dose and other cell types, and whether the relationship extends to cells embedded within a hydrogel more representative of how cells would behave in soft tissue. Additionally one section of the parameter range that was unable to be explored was the effect of the incident frequency. In changing the incident frequency the focal size would also have been changed, in doing so the proportion of the blood exposed to high pressures would have been dramatically altered. It would be interesting to see what, if any, effect these changes would potentially have on the cellular safety - cavitation dose relationship.

Despite these limitations, the consistency in the relationship between the cavitation dose metric and cellular safety is a promising result which suggests that information about these relationships may be able to be carried between applications utilising different ultrasound parameters. Additionally, this allows for accurate therapy monitoring even if some of the parameters such as pressure in the body, concentration of cavitation agent in the bloodstream, etc, are unknown.

5.4 Energy-Preserving Cavitation Imaging (Chapter 4)

In line with the objective of developing set-up independent cavitation dose metrics, Chapter 4 set out to develop an improved PAM algorithm that would provide adequate spatial resolution and would be computationally efficient whilst being energy-preserving. The LRD-PAM algorithm is able to provide a significant reduction to the noise present in TEA-PAM imaging achieving similar image quality to RCB-PAM. This is achieved with only a minor increase in computation

time over the TEA algorithm. The LRD-PAM algorithm additionally provides more accurate estimates of the cavitation energy being generated than both TEA and RCB algorithms. Taken together, these results demonstrate the potential of the LRD-PAM algorithm as a fast technique for accurate real-time cavitation monitoring which allows for set-up independent PAM derived measures of cavitation activity.

The main limitation in the work presented in this chapter is the limited range of experimental data and applications for which the algorithm has been tested, focus was instead placed on attempting a thorough exploration of the algorithms effectiveness within the applications explored within my thesis' work. Further work will be needed to tell to what extent the limitations in assumption of the point spread function and errors in localisation limit the algorithm's usefulness.

A second major limitation of the work presented in this, and all of the chapters in this thesis is the fact that due to hardware limitations essentially all the cavitation imaging was limited to 2D. This leads to the forcing of assumptions on the distribution of cavitation in the elevational plane which limits PAM's utility and potentially is the source for not insignificant errors. Significant improvements in readily available hardware is required to fix these limitations which will hopefully be developed in the future.

In spite of a number of limitations, the work conducted as part of this thesis has provided compelling evidence that a set-up independent, energy-preserving spatiotemporal metric of cavitation dose is possible using suitably calibrated and corrected passive acoustic mapping techniques. This type of approach has been shown to be potentially predictive of both treatment safety and efficacy in the context of ultrasound-enhanced drug delivery and immunomodulation. It is hoped that the overall approach will inspire future researchers to investigate its applicability across the ever-growing range of therapeutic ultrasound applications ranging from transdermal drug delivery to opening the blood brain barrier.

References

Apfel, Robert E. and Christy K. Holland (1991). "Gauging the likelihood of cavitation from short-pulse, low-duty cycle diagnostic ultrasound". In: *Ultrasound in Medicine and Biology* 17.2, pp. 179–185.

Arvanitis, Costas D. et al. (2011). "Cavitation-Enhanced Extravasation for Drug Delivery". In: *Ultrasound in Medicine and Biology* 37.11, pp. 1838–1852.

Arvanitis, Costas D. et al. (2012). "Controlled Ultrasound-Induced Blood-Brain Barrier Disruption Using Passive Acoustic Emissions Monitoring". In: *PLoS ONE* 7.9.

Arvanitis, Costas D. et al. (2017). "Passive Acoustic Mapping with the Angular Spectrum Method". In: *IEEE Transactions on Medical Imaging* 36.4, pp. 983–993.

Azzi, Sandy, Jagoda K. Hebda, and Julie Gavard (2013). "Vascular Permeability and Drug Delivery in Cancers". In: *Frontiers in Oncology* 3.August, pp. 1–14. URL: `http://journal.frontiersin.org/article/10.3389/fonc.2013.00211/abstract`.

Bader, Kenneth B et al. (2017). "Post hoc analysis of passive cavitation imaging for classification of histotripsy-induced liquefaction in vitro". In: *IEEE transactions on medical imaging* 37.1, pp. 106–115.

Bazan-Peregrino, Miriam et al. (2012). "Ultrasound-induced cavitation enhances the delivery and therapeutic efficacy of an oncolytic virus in an in vitro model". In: *Journal of Controlled Release* 157.2, pp. 235–242. URL: `http://dx.doi.org/10.1016/j.jconrel.2011.09.086`.

Bazan-Peregrino, Miriam et al. (2013). "Cavitation-enhanced delivery of a replicating oncolytic adenovirus to tumors using focused ultrasound". In: *Journal of Controlled Release* 169.1-2, pp. 40–47. URL: `http://dx.doi.org/10.1016/j.jconrel.2013.03.017`.

Benjamin, T Brooke and Ao T Ellis (1966). "The collapse of cavitation bubbles and the pressures thereby produced against solid boundaries". In: *Philosophical Transactions for the Royal Society of London. Series A, Mathematical and Physical Sciences*, pp. 221–240.

Bhatnagar, Sunali et al. (2016). "Exploitation of sub-micron cavitation nuclei to enhance ultrasound-mediated transdermal transport and penetration of vaccines". In: *Journal of Controlled Release* 238, pp. 22–30. URL: `http://dx.doi.org/10.1016/j.jconrel.2016.07.016`.

Biggs, David S. C. and Mark Andrews (1997). "Acceleration Of Iterative Image Restoration Algorithms". In: *Applied Optics* 36.8, pp. 1766–1775.

Bjerknes, Vilhelm (1906). *Fields of force*. General Books.

— (1909). *Die Kraftfelder*. 28. F. Vieweg.

Blackstock, David T (n.d.). *Fundamentals of Physical Acoustics, book, 2000*.

Blake, F. G. (1948). "Onset of Acoustical Cavitation in Fluids". In: *The Journal of the Acoustical Society of America* 20.4, pp. 590–590. URL: `http://asa.scitation.org/doi/10.1121/1.1916981`.

Blake, J. and D. C. Gibson (1987). "Cavitation Bubbles Near Boundaries". In: *Annual Review of Fluid Mechanics* 19.1, pp. 99–123. URL: http://fluid.annualreviews.org/cgi/doi/10.1146/annurev.fluid.19.1.99.

Brujan, Emil-Alexandru (2000). "Dynamics of laser-induced cavitation bubbles near an elastic boundary used as a tissue phantom". In: *AIP Conference Proceedings* 433, pp. 381–384. URL: http://link.aip.org/link/?APC/524/381/1{\&}Agg=doi.

Carey, Michael P. and Thomas G. Burish (1988). "Etiology and Treatment of the Psychological Side Effects Associated With Cancer Chemotherapy: A Critical Review and Discussion". In: *Psychological Bulletin* 104.3, pp. 307–325.

Carlisle, Robert et al. (2013). "Enhanced tumor uptake and penetration of virotherapy using polymer stealthing and focused ultrasound." In: *Journal of the National Cancer Institute* 105.22, pp. 1701–1710.

Caskey, Charles F. et al. (2007). "Direct observations of ultrasound microbubble contrast agent interaction with the microvessel wall". In: *The Journal of the Acoustical Society of America* 122.2, pp. 1191–1200. URL: http://asa.scitation.org/doi/10.1121/1.2747204.

Chaussy, Christian et al. (2017). "First Clinical Experience with Extracorporeally Induced Destruction of Kidney Stones by Shock Waves". In: *Journal of Urology* 197.2, S160–S163.

Chen, Hong et al. (2010). "Blood vessel rupture by cavitation". In: *Urological Research* 38.4, pp. 321–326. arXiv: NIHMS150003.

Chen, Hong et al. (2011a). "Blood vessel deformations on microsecond time scales by ultrasonic cavitation". In: *Physical Review Letters* 106.3, pp. 1–4. arXiv: NIHMS150003.

Chen, Hong et al. (2011b). "Observations of translation and jetting of ultrasound-activated microbubbles in mesenteric microvessels". In: *Ultrasound in Medicine and Biology* 37.12, pp. 2139–2148. arXiv: NIHMS150003.

Chen, W S et al. (2003a). "Inertial cavitation dose and hemolysis produced in vitro with or without Optison". In: *Ultrasound Med Biol* 29.5, pp. 725–737. URL: https://www.ncbi.nlm.nih.gov/pubmed/12754072.

Chen, Wen-Shiang et al. (2003b). "The pulse length-dependence of inertial cavitation dose and hemolysis". In: *Ultrasound in medicine & biology* 29.5, pp. 739–748.

Child, S.Z. et al. (1990). "Lung damage from exposure to pulsed ultrasound". In: *Ultrasound in Medicine & Biology* 16.8, pp. 817–825.

Choi, James J. et al. (2014). "Non-invasive and real-time passive acoustic mapping of ultrasound-mediated drug delivery". In: *Physics in Medicine and Biology* 59.17, pp. 4861–4877. URL: http://iopscience.iop.org/article/10.1088/0031-9155/59/17/4861/pdf.

Church, Charles C. (2002). "Spontaneous homogeneous nucleation, inertial cavitation and the safety of diagnostic ultrasound". In: *Ultrasound in Medicine and Biology* 28.10, pp. 1349–1364.

Church, Charles C and Edwin L Carstensen (2001). ""Stable" inertial cavitation". In: *Ultrasound in medicine & biology* 27.10, pp. 1435–1437.

Clarke, RL and GR Ter Haar (1997). "Temperature rise recorded during lesion formation by high-intensity focused ultrasound". In: *Ultrasound in medicine & biology* 23.2, pp. 299–306.

Collin, James R T (2009). "Detection and Interpretation of Thermally Relevant Cavitation During HIFU Exposure". In.

Collin, Jamie R. T. and Constantin C. Coussios (2011). "Quantitative observations of cavitation activity in a viscoelastic medium". In: *The Journal of the Acoustical Society of America* 130.5, pp. 3289–3296. URL: http://asa.scitation.org/doi/10.1121/1.3626156.

Collis, James et al. (2010). "Cavitation microstreaming and stress fields created by microbubbles". In: *Ultrasonics* 50.2, pp. 273–279. URL: http://dx.doi.org/10.1016/j.ultras.2009.10.002.

Cooper, GM (2000). *The Cell: A Molecular Approach, 2nd edn. The Cell: A Molecular Approach. Sunderland, MA*.

Corry, Peter M. et al. (1982). "Ultrasound-induced hyperthermia for the treatment of human superficial tumors". In: *International Journal of Radiation Oncology, Biology, Physics* 8.7, pp. 1225–1229.

Coussios, C. C. et al. (2007). "Role of acoustic cavitation in the delivery and monitoring of cancer treatment by high-intensity focused ultrasound (HIFU)". In: *International Journal of Hyperthermia* 23.2, pp. 105–120.

Coviello, Christian et al. (2015). "Passive acoustic mapping utilizing optimal beamforming in ultrasound therapy monitoring." In: *The Journal of the Acoustical Society of America* 137.5, p. 2573. URL: http://www.ncbi.nlm.nih.gov/pubmed/25994690.

Cox, D. R. (1972). "Regression Models and Life-Tables". In: *Journal of the Royal Statistical Society: Series B (Methodological)* 34.2, pp. 187–202.

Crake, Calum et al. (2016). "Enhancement and Passive Acoustic Mapping of Cavitation from Fluorescently Tagged Magnetic Resonance-Visible Magnetic Microbubbles In Vivo". In: *Ultrasound in Medicine and Biology* 42.12, pp. 3022–3036.

Crake, Calum et al. (2018). "A dual-mode hemispherical sparse array for 3D passive acoustic mapping and skull localization within a clinical MRI guided focused ultrasound device". In: *Physics in Medicine and Biology* 63.6.

Cui, Shangbin (2006). "Formation of nectrotic cores in the growth of tumors: analytic results". In: *Acta Mathematica Scientia* 26.4, pp. 781–796.

Culjat, Martin O. et al. (2010). "A review of tissue substitutes for ultrasound imaging". In: *Ultrasound in Medicine and Biology* 36.6, pp. 861–873.

Datta, Saurabh et al. (2006). "Correlation of cavitation with ultrasound enhancement of thrombolysis". In: *Ultrasound in Medicine and Biology* 32.8, pp. 1257–1267.

Den Brok, Martijn H.M.G.M. et al. (2004). "In situ tumor ablation creates an antigen source for the generation of antitumor immunity". In: *Cancer Research* 64.11, pp. 4024–4029.

Dimcevski, Georg et al. (2016). "A human clinical trial using ultrasound and microbubbles to enhance gemcitabine treatment of inoperable pancreatic cancer". In: *Journal of Controlled Release* 243, pp. 172–181.

Dvorak, H F et al. (1995). "Vascular permeability factor/vascular endothelial growth factor, microvascular hyperpermeability, and angiogenesis." In: *The American journal of pathology* 146.5, pp. 1029–39. URL: http://www.pubmedcentral.nih.gov/articlerender.fcgi?artid=1869291{\&}tool=pmcentrez{\&}rendertype=abstract.

Eisenhauer, E. A. et al. (2009). "New response evaluation criteria in solid tumours: Revised RECIST guideline (version 1.1)". In: *European Journal of Cancer* 45.2, pp. 228–247. URL: http://dx.doi.org/10.1016/j.ejca.2008.10.026.

Euler, L (1755). "Principes généraux de l'état d'équilibre des fluides; Principes généraux du mouvement des fluides; Continuation des recherches sur la théorie du mouvement des fluides". In: *Histoire de l'Académie de Berlin*.

Everbach, E. Carr et al. (1997). "Correlation of ultrasound-induced hemolysis with cavitation detector output in vitro". In: *Ultrasound in Medicine and Biology* 23.4, pp. 619–624.

Fan, Zhenzhen et al. (2012). "Spatiotemporally controlled single cell sonoporation". In: *Proceedings of the National Academy of Sciences of the United States of America* 109.41, pp. 16486–16491. URL: http://www.pubmedcentral.nih.gov/articlerender.fcgi?artid=3478613{\&}tool=pmcentrez{\&}rendertype=abstract{\%}5Cnhttp://www.pnas.org/content/109/41/16486.short.

Faraday, MICHAEL (1831). "On the forms and states assumed by fluids in contact with vibrating elastic surfaces". In: *Philos. Trans. R. Soc. London* 121, pp. 39–346.

Farny, Caleb H., R. Glynn Holt, and Ronald A. Roy (2010). "The correlation between bubble-enhanced HIFU heating and cavitation power". In: *IEEE Transactions on Biomedical Engineering* 57.1, pp. 175–184.

Fish, D. A. et al. (1995). "Blind deconvolution by means of the Richardson–Lucy algorithm". In: *Journal of the Optical Society of America A* 12.1, p. 58.

Fite, Brett Z. et al. (2021). "Immune modulation resulting from MR-guided high intensity focused ultrasound in a model of murine breast cancer". In: *Scientific Reports* 11.1, pp. 1–15. URL: https://doi.org/10.1038/s41598-020-80135-1.

Ghiringhelli, François et al. (2009). "Activation of the NLRP3 inflammasome in dendritic cells induces IL-1B-dependent adaptive immunity against tumors". In: *Nature Medicine* 15.10, pp. 1170–1178.

Gilmore, Forrest R. (1952). "The growth or collapse of a spherical bubble in a viscous compressible liquid". In: *California Institute of Tech Engineering Report* 26.4, pp. 1–40.

Graham, S M et al. (2014). "Inertial cavitation to non-invasively trigger and monitor intratumoral release of drug from intravenously delivered liposomes". In: *J Control Release* 178, pp. 101–107. URL: https://www.ncbi.nlm.nih.gov/pubmed/24368302.

Gray, Michael D. and Constantin C. Coussios (2018). "Broadband Ultrasonic Attenuation Estimation and Compensation With Passive Acoustic Mapping". In: pp. 497–516.

— (2019). "Compensation of array lens effects for improved co-registration of passive acoustic mapping and B-mode images for cavitation monitoring". In: *The Journal of the Acoustical Society of America* 146.1, EL78–EL84. URL: http://asa.scitation.org/doi/10.1121/1.5118238.

Gray, Michael D, Erasmia Lyka, and Constantin C Coussios (2018). "Diffraction Effects and Compensation in Passive Acoustic Mapping". In: 65.2, pp. 258–268.

Grayburn, Paul a (2002). "Current and future contrast agents." In: *Echocardiography (Mount Kisco, N.Y.)* 19.3, pp. 259–265.

Greten, Florian R. and Sergei I. Grivennikov (2019). "Inflammation and Cancer: Triggers, Mechanisms, and Consequences". In: *Immunity* 51.1, pp. 27–41. URL: https://doi.org/10.1016/j.immuni.2019.06.025.

Guo, Xiasheng et al. (2013). "Investigation on the inertial cavitation threshold and shell properties of commercialized ultrasound contrast agent microbubbles". In: *The Journal of the Acoustical Society of America* 134.2, pp. 1622–1631. URL: http://asa.scitation.org/doi/10.1121/1.4812887.

Gyöngy, M et al. (2008). "Use of passive arrays for characterization and mapping of cavitation activity during hifu exposure". In: *Proceedings - IEEE Ultrasonics Symposium*, pp. 871–874. URL: https://pdfs.semanticscholar.org/ebec/31d1f2e4438f3533d294182a7fcbb61b9288.pdf.

Gyöngy, Miklós and Constantin-C. Coussios (2010a). "Passive cavitation mapping for localization and tracking of bubble dynamics". In: *The Journal of the Acoustical Society of America* 128.4, EL175–EL180. URL: http://scitation.aip.org/content/asa/journal/jasa/128/4/10.1121/1.3467491.

— (2010b). "Passive spatial mapping of inertial cavitation during HIFU exposure". In: *IEEE Transactions on Biomedical Engineering* 57.1, pp. 48–56.

Hamilton, Mark F, David T Blackstock, et al. (1998). *Nonlinear acoustics*. Vol. 237. Academic press San Diego.

Harvey, E Newton et al. (1944). "Bubble formation in animals. I. Physical factors". In: *Journal of Cellular and Comparative Physiology* 24.1, pp. 1–22.

Haworth, Kevin J. et al. (2017). "Quantitative frequency-domain passive cavitation imaging". In: *IEEE Transactions on Ultrasonics, Ferroelectrics, and Frequency Control* 64.1, pp. 177–191.

Hendley, Samuel A et al. (2021). "Clot degradation under the action of histotripsy bubble activity and a lytic drug". In: *IEEE transactions on ultrasonics, ferroelectrics, and frequency control* 68.9, pp. 2942–2952.

Hersh, David S. et al. (2016). "Pulsed ultrasound expands the extracellular and perivascular spaces of the brain". In: *Brain Research* 1646, pp. 543–550. URL: http://dx.doi.org/10.1016/j.brainres.2016.06.040.

Hiller, Jonathan G. et al. (2018). "Perioperative events influence cancer recurrence risk after surgery". In: *Nature Reviews Clinical Oncology* 15.4, pp. 205–218.

Hitchcock, Kathryn E et al. (2011). "Ultrasound-enhanced rt-PA thrombolysis in an ex vivo porcine carotid artery model". In: *Ultrasound in medicine & biology* 37.8, pp. 1240–1251.

Holt, R. Glynn and Lawrence A. Crum (1992). "Acoustically forced oscillations of air bubbles in water: Experimental results". In: *The Journal of the Acoustical Society of America* 91.4, pp. 1924–1932. URL: http://asa.scitation.org/doi/10.1121/1.403703.

Holt, R Glynn and Ronald A Roy (2001). "Measurements of bubble-enhanced heating from focused, MHz-frequency ultrasound in a tissue-mimicking material". In: *Ultrasound in medicine & biology* 27.10, pp. 1399–1412.

Hwang, Joo Ha et al. (2005). "Vascular effects induced by combined 1-MHz ultrasound and microbubble contrast agent treatments in vivo". In: *Ultrasound in medicine & biology* 31.4, pp. 553–564.

Hwang, Joo Ha et al. (2006). "Correlation between inertial cavitation dose and endothelial cell damage in vivo". In: *Ultrasound in medicine & biology* 32.10, pp. 1611–1619.

Hynynen, Kullervo (1991). "The threshold for thermally significant cavitation in dog's thigh muscle in vivo". In: *Ultrasound in medicine & biology* 17.2, pp. 157–169.

Hynynen, Kullervo et al. (2001). "Noninvasive MR Imaging–guided Focal Opening of the Blood-Brain Barrier in Rabbits". In: *Radiology* 220.3, pp. 640–646. URL: https://pubs.rsna.org/doi/pdf/10.1148/radiol.2202001804http://pubs.rsna.org/doi/10.1148/radiol.2202001804.

J. Capon (1969). "High-Resolution Frequency-Wavenumber Spectrum Analysis". In: 57.8, pp. 1408–1418.

Jahanpanah, Newsha et al. (2019). "Hemolysis resulting from acoustic droplet vaporization and inertial cavitation". In: *Proceedings of Meetings on Acoustics 177ASA*. Vol. 36. 1. Acoustical Society of America, p. 020001.

Jain, Rakesh K. (2009). "Delivery of molecular and cellular medicine to solid tumors". In: *Cancer Research* 42.1, pp. 115–125. arXiv: NIHMS150003.

Jain, Rakesh K and Kimberly Ward-Hartley (1984). "Tumor Blood Flow - Characterization, Modifications, and Role in Hyperthermia". In: *IEEE transactions on sonics and ultrasonics* SU-31.5, pp. 504–526. URL: http://www.scopus.com/inward/record.url?partnerID=yv4JPVwI{\&}eid=2-s2.0-0021494998{\&}md5=fb9364fcdb7c9e28acab67533fdeba54{\%}5Cnpapers3://publication/uuid/7AA990B7-2A1D-427C-A326-3E74545B37CB.

Jiang, Xue et al. (2014). "Robust beamforming by linear programming". In: *IEEE Transactions on Signal Processing* 62.7, pp. 1834–1849.

Johansen, Kristoffer, Jae Hee Song, and Paul Prentice (2017). "Validity of the Keller-Miksis equation for 'non-stable' cavitation and the acoustic emissions generated". In: *IEEE International Ultrasonics Symposium, IUS* September.

Jones, Ryan M, Dallan McMahon, and Kullervo Hynynen (2020). "Ultrafast three-dimensional microbubble imaging in vivo predicts tissue damage volume distributions during nonthermal brain ablation". In: *Theranostics* 10.16, p. 7211.

Jones, Ryan M., Meaghan A. O'Reilly, and Kullervo Hynynen (2013). "Transcranial passive acoustic mapping with hemispherical sparse arrays using CT-based skull-specific aberration corrections: A simulation study". In: *Physics in Medicine and Biology* 58.14, pp. 4981–5005. arXiv: NIHMS150003.

Jones, Ryan M, Meaghan A O'Reilly, and Kullervo Hynynen (2015). "Experimental demonstration of passive acoustic imaging in the human skull cavity using CT-based aberration corrections". In: *Medical physics* 42.7, pp. 4385–4400.

Kamimura, Hermes A S et al. (2020). "Real-time passive acoustic mapping using sparse matrix multiplication". In.

Katti, Prateek S (2020). "Drug-Device Development : Cancer Immunotherapy with Therapeutic , Ultrasound-Mediated Delivery". In: January.

Keller, Joseph B. and Michael Miksis (1980). "Bubble oscillations of large amplitude". In: *The Journal of the Acoustical Society of America* 68.2, pp. 628–633. URL: http://asa.scitation.org/doi/10.1121/1.384720.

Kennedy, James E. (2005). "High-intensity focused ultrasound in the treatment of solid tumours". In: *Nature Reviews Cancer* 5.4, pp. 321–327. URL: http://www.nature.com/articles/nrc1591.

Khaibullina, A. et al. (2008). "Pulsed High-Intensity Focused Ultrasound Enhances Uptake of Radiolabeled Monoclonal Antibody to Human Epidermoid Tumor in Nude Mice". In: *Journal of Nuclear Medicine* 49.2, pp. 295–302. URL: http://jnm.snmjournals.org/cgi/doi/10.2967/jnumed.107.046888.

Khokhlova, Vera A et al. (2015). "Histotripsy methods in mechanical disintegration of tissue: Towards clinical applications". In: *International journal of hyperthermia* 31.2, pp. 145–162.

Kong, G., R. D. Braun, and M. W. Dewhirst (2001). "Characterization of the effect of hyperthermia on nanoparticle extravasation from tumor vasculature". In: *Cancer Research* 61.7, pp. 3027–3032.

Krall, Jordan A. et al. (2018). "The systemic response to surgery triggers the outgrowth of distant immune-controlled tumors in mouse models of dormancy". In: *Science Translational Medicine* 10.436, pp. 1–12.

Kwan, J J et al. (2015a). "Ultrasound-induced inertial cavitation from gas-stabilizing nanoparticles". In: *Physical Review E* 92.2, p. 23019.

Kwan, James J et al. (2015b). "Ultrasound-Propelled Nanocups for Drug Delivery". In: *Small* 11.39, pp. 5305–5314.

Lacoss, R T. (1971). *Data adaptive spectral analysis methods.*

Lagrange, Joseph Louis (1761). *Essai d'une nouvelle methode pour de'terminer les maxima, et les minima des formules integrales indefinies.*

Landau, LD and EM Lifshitz (1959). *Course of theoretical physics. vol. 6: Fluid mechanics.* London.

Lauterborn, Werner (1976). "Numerical investigation of nonlinear oscillations of gas bubbles in liquids". In: *The Journal of the Acoustical Society of America* 59.2, pp. 283–293. URL: http://asa.scitation.org/doi/10.1121/1.380884.

Lazarus, Carole et al. (2017). "Clustering dynamics of microbubbles exposed to low-pressure 1-MHz ultrasound". In: 3135.

Lea-Banks, Harriet et al. (2016). "The effect of particle density on ultrasound-mediated transport of nanoparticles". In: *Physics in Medicine and Biology* 61.22, pp. 7906–7918.

Leighton, TG (n.d.). "The Acoustic Bubble (Academic, London, 1994)". In: *Google Scholar* (), pp. 1–613.

Leu, Anders J et al. (2000). "Absence of Functional Lymphatics within a Murine Sarcoma : A Molecular and Functional Evaluation Advances in Brief Absence of Functional Lymphatics within a Murine Sarcoma : A Molecular and Functional Evaluation 1". In: pp. 4324–4327.

Lighthill, Michael J and James Lighthill (2001). *Waves in fluids.* Cambridge university press.

Lucy, L. B. (1974). "An iterative technique for the rectification of observed distributions". In: *The Astronomical Journal* 79.6, p. 745.

Lyka, Erasmia et al. (2018). *Passive Acoustic Mapping using Data-Adaptive Beamforming Based on Higher-Order Statistics.*

Madanshetty, Sameer I, Ronald A Roy, and Robert E Apfel (1991). "Acoustic microcavitation: Its active and passive acoustic detection". In: *The Journal of the Acoustical Society of America* 90.3, pp. 1515–1526.

Marmottant, Philippe et al. (2005). "A model for large amplitude oscillations of coated bubbles accounting for buckling and rupture". In: *The Journal of the Acoustical Society of America* 118.6, pp. 3499–3505.

Marzetta, Thomas L. (1983). "A New Interpretation for Capon's Maximum Likelihood Method of Frequency-Wavenumber Spectral Estimation". In: *IEEE Transactions on Acoustics, Speech, and Signal Processing* 31.2, pp. 445–449.

Mast, T. Douglas (2000). "Empirical relationships between acoustic parameters in human soft tissues". In: *Acoustics Research Letters Online* 1.2, pp. 37–42. URL: http://asa.scitation.org/doi/10.1121/1.1336896.

Maxwell, Adam D. et al. (2013). "Probability of Cavitation for Single Ultrasound Pulses Applied to Tissues and Tissue-Mimicking Materials". In: *Ultrasound in Medicine and Biology* 39.3, pp. 449–465. arXiv: NIHMS150003.

Mettin, R. et al. (1997). "Bjerknes forces between small cavitation bubbles in a strong acoustic field". In: *Physical Review E - Statistical Physics, Plasmas, Fluids, and Related Interdisciplinary Topics* 56.3, pp. 2924–2931.

Miller, Douglas L. (2007). "Overview of experimental studies of biological effects of medical ultrasound caused by gas body activation and inertial cavitation". In: *Progress in Biophysics and Molecular Biology* 93.1-3, pp. 314–330.

Mo, Steven et al. (2015). "Increasing the density of nanomedicines improves their ultrasound-mediated delivery to tumours". In: *Journal of Controlled Release* 210, pp. 10–18. URL: http://dx.doi.org/10.1016/j.jconrel.2015.05.265.

Myers, Rachel et al. (2016). "Polymeric cups for cavitation-mediated delivery of oncolytic vaccinia virus". In: *Molecular Therapy* 24.9, pp. 1627–1633. URL: http://dx.doi.org/10.1038/mt.2016.139.

National Statistics, Office for (2018). *Deaths registered in England and Wales: 2017*. URL: https://www.ons.gov.uk/peoplepopulationandcommunity/birthsdeathsandmarriages/deaths/bulletins/deathsregistrationsummarytables/2017 (visited on 08/06/2018).

Neppiras, E. A. (1969). "Subharmonic and Other Low-Frequency Emission from Bubbles in Sound-Irradiated Liquids". In: *The Journal of the Acoustical Society of America* 46.3B, pp. 587–601.

— (1980a). "Acoustic cavitation thresholds and cyclic processes". In: *Ultrasonics* 18.5, pp. 201–209.

Neppiras, E. A. and B. E. Noltingk (1951). "Cavitation produced by ultrasonics: Theoretical conditions for the onset of cavitation". In: *Proceedings of the Physical Society. Section B* 64.12, pp. 1032–1038.

Neppiras, E.a. (1980b). "Acoustic cavitation". In: *Physics Reports* 61.3, pp. 159–251.

Noltingk, B. E. and E. A. Neppiras (1950). "Cavitation produced by ultrasonics". In: *Proceedings of the Physical Society. Section B* 63.9, pp. 674–685.

Norton, Stephen J. (2000). "Time exposure acoustics". In: *IEEE Transactions on Geoscience and Remote Sensing* 38.3, pp. 1337–1343.

O'Reilly, Meaghan A. and Kullervo Hynynen (2012). "Blood-Brain Barrier: Real-time Feedback-controlled Focused Ultrasound Disruption by Using an Acoustic Emissions–based Controller". In: *Radiology* 263.1, pp. 96–106. arXiv: NIHMS150003. URL: http://pubs.rsna.org/doi/10.1148/radiol.11111417.

O'Reilly, Meaghan A, Ryan M Jones, and Kullervo Hynynen (2014). "Three-dimensional transcranial ultrasound imaging of microbubble clouds using a sparse hemispherical array". In: *IEEE Transactions on Biomedical Engineering* 61.4, pp. 1285–1294.

Palesh, Oxana et al. (2018). "Management of side effects during and post-treatment in breast cancer survivors". In: *The breast journal* 24.2, pp. 167–175.

Patel, Arpit, Scott J. Schoen Jr, and Costas D. Arvanitis (2018). "Closed Loop Spatial and Temporal Control of Cavitation Activity with Passive Acoustic Mapping". In: *IEEE Transactions on Biomedical Engineering* 016971.April, pp. 1–1. URL: https://ieeexplore.ieee.org/document/8540931/.

Pereno, V. et al. (2018). "Layered acoustofluidic resonators for the simultaneous optical and acoustic characterisation of cavitation dynamics, microstreaming, and biological effects". In: *Biomicrofluidics* 12.3, p. 034109. URL: http://aip.scitation.org/doi/10.1063/1.5023729.

Plesset, Milton S. (1949). "The Dynamics of Cavitation Bubbles". In: *Journal of Applied Mechanics*.

Plesset, Milton S. and Andrea Prosperetti (1977). "Bubble Dynamics and Cavitation". In: *Annual Review of Fluid Mechanics*, pp. 145–185.

Poritsky, H (1951). "The collapse or growth of a spherical bubble or cavity in a viscous fluid". In: *JOURNAL OF APPLIED MECHANICS-TRANSACTIONS OF THE ASME*. Vol. 18. 3. ASME-AMER SOC MECHANICAL ENG 345 E 47TH ST, NEW YORK, NY 10017, pp. 332–333.

Qu, Shibin et al. (2020). "Non-thermal histotripsy tumor ablation promotes abscopal immune responses that enhance cancer immunotherapy". In: *Journal for immunotherapy of cancer* 8.1.

Rayleigh, Lord (1917). "VIII. On the pressure developed in a liquid during the collapse of a spherical cavity". In: *Philosophical Magazine Series 6* 34.200, pp. 94–98. URL: http://www.tandfonline.com/doi/abs/10.1080/14786440808635681.

Rich, Kyle T and T Douglas Mast (2015a). "Accuracy of a bistatic scattering substitution technique for calibration of focused receivers". In: *The Journal of the Acoustical Society of America* 138.5, EL469–EL473.

Rich, Kyle T. and T. Douglas Mast (2015b). "Methods to calibrate the absolute receive sensitivity of single-element, focused transducers". In: *The Journal of the Acoustical Society of America* 138.3, EL193–EL198. URL: http://asa.scitation.org/doi/10.1121/1.4929620.

Richardson, William Hadley (1972). "Bayesian-Based Iterative Method of Image Restoration*". In: *Journal of the Optical Society of America* 62.1, p. 55.

Roberts, William W et al. (2006). "Pulsed cavitational ultrasound: A noninvasive technology for controlled tissue ablation (histotripsy) in the rabbit kidney". In: *Journal of Urology* 175.2, pp. 734–738. URL: https://ac.els-cdn.com/S0022534705001412/1-s2.0-S0022534705001412-main.pdf?{_}tid=634f6df7-441c-4b21-9433-0ac439e2f438{\&}acdnat=1533472051{_}fcb308313337d1616f2eb7a7b0ab6e3d.

Samiotaki, Gesthimani et al. (2012). "Pressure and microbubble size dependence study of focused ultrasound-induced blood-brain barrier opening reversibility in vivo". In: *AIP Conference Proceedings* 1481, pp. 300–306. arXiv: NIHMS150003.

Samuel, Stanley et al. (2009). "An ex vivo Study of the Correlation Between Acoustic Emission and Microvascular Damage". In: *Ultrasound in Medicine and Biology* 35.9, pp. 1574–1586.

Schoen, Scott and Costas D. Arvanitis (2019). "Heterogeneous Angular Spectrum Method for Trans-skull Imaging and Focusing". In: *IEEE Transactions on Medical Imaging*, pp. 1–1. arXiv: 1906.08156.

— (2020). "Acoustic Source Localization With the Angular Spectrum Approach in Continuously Stratified Media". In: *arXiv* 333. arXiv: 2007.01133.

Shi, Liangrong et al. (2019). "Inflammation induced by incomplete radiofrequency ablation accelerates tumor progression and hinders PD-1 immunotherapy". In: *Nature Communications* 10.1. URL: http://dx.doi.org/10.1038/s41467-019-13204-3.

Smith, Cameron and Constantin Coussios (2019). "Spatiotemporal assessment of the cellular safety of cavitation-based therapies by passive acoustic mapping". In: *The 24th European Symposium on Ultrasound Contrast Imaging*, pp. 194–195.

Smith, Cameron AB and Constantin C Coussios (2020). "Spatiotemporal assessment of the cellular safety of cavitation-based therapies by passive acoustic mapping". In: *Ultrasound in medicine & biology* 46.5, pp. 1235–1243.

Sorg, Brian S. et al. (2008). "Spectral imaging facilitates visualization and measurements of unstable and abnormal microvascular oxygen transport in tumors". In: *Journal of Biomedical Optics* 13.1, p. 014026. URL: http://biomedicaloptics.spiedigitallibrary.org/article.aspx?doi=10.1117/1.2837439.

Stieger, Susanne M. et al. (2007). "Enhancement of Vascular Permeability with Low-Frequency Contrast-enhanced Ultrasound in the Chorioallantoic Membrane Model". In: *Radiology* 243.1, pp. 112–121. URL: http://pubs.rsna.org/doi/10.1148/radiol.2431060167.

Stoica, Petre, Zhisong Wang, and Jian Li (2003). "Robust Capon beamforming". In: *IEEE Signal Processing Letters* 10.6, pp. 172–175. URL: https://pdfs.semanticscholar.org/d02c/595bd55b9802c64b6c16455bc90e53557d9e.pdf.

Stokes, George Gabriel (1880). "On the theories of the internal friction of fluids in motion, and of the equilibrium and motion of elastic solids". In: *Transactions of the Cambridge Philosophical Society* 8.

Stride, ER and C Coussios (2019). "Nucleation, Mapping and Control of Cavitation for Drug Delivery". In: *Nature Reviews Physics*. URL: https://ora.ox.ac.uk/objects/uuid:99f60a2a-bdd6-43d6-94bf-142df0ad7d15.

Sun, Tao et al. (2017). "Closed-loop control of targeted ultrasound drug delivery across the blood-brain/tumor barriers in a rat glioma model". In: *Pnas*. URL: http://feedproxy.google.com/{~}r/Pnas-RssFeedOfEarlyEditionArticles/{~}3/BvUB7GXdXt0/1713328114.short.

ter Haar, G. R. (2002). "Ultrasonic contrast agents: Safety considerations reviewed". In: *European Journal of Radiology* 41.3, pp. 217–221.

Tho, Paul, Richard Manasseh, and Andrew Ioo (2007). "Cavitation microstreaming patterns in single and multiple bubble systems". In: *Journal of Fluid Mechanics* 576, pp. 191–233. URL: https://www.cambridge.org/core/services/aop-cambridge-core/content/view/617EE8D1FB28FBF494B37FF99355FA35/S0022112006004393a.pdf/cavitation{_}microstreaming{_}patterns{_}in{_}single{_}and{_}multiple{_}bubble{_}systems.pdf.

Trédan, Olivier et al. (2007). "Drug resistance and the solid tumor microenvironment". In: *Journal of the National Cancer Institute* 99.19, pp. 1441–1454.

Tsai, Chih Hung et al. (2016). "Real-time monitoring of focused ultrasound blood-brain barrier opening via subharmonic acoustic emission detection: Implementation of confocal dual-frequency piezoelectric transducers". In: *Physics in Medicine and Biology* 61.7, pp. 2926–2946.

UK, Cancer Research (2018). *Cancer Statistics for the UK*. URL: https://www.cancerresearchuk.org/health-professional/cancer-statistics-for-the-uk (visited on 08/06/2018).

White, DR et al. (1998). "Tissue substitutes, phantoms and computational modelling in medical ultrasound". In: *ICRU Report*.

Williams, A. R. et al. (1991). "The Effects of the Microbubble Suspension SH U 454 (Echovist®) on Ultrasound-Induced Cell Lysis In a Rotating Tube Exposure System". In: *Echocardiography* 8.4, pp. 423–433. URL: http://doi.wiley.com/10.1111/j.1540-8175.1991.tb01003.x.

Wood, R.W. and Alfred L. Loomis (1927). "The physical and biological effects of high-frequency sound-waves of great intensity". In: *The London, Edinburgh, and Dublin Philosophical Magazine and Journal of Science* 4.22, pp. 417–436. URL: http://www.tandfonline.com/doi/abs/10.1080/14786440908564348.

Wood, Simon N (2017). *Generalized additive models: an introduction with R*. CRC press.

Wu, Feng et al. (2004). "Extracorporeal focused ultrasound surgery for treatment of human solid carcinomas: early Chinese clinical experience". In: *Ultrasound in Medicine & Biology* 30.2, pp. 245–260. URL: http://www.umbjournal.org/article/S0301-5629(03)01144-X/pdfhttp://linkinghub.elsevier.com/retrieve/pii/S030156290301144X.

Wu, Min et al. (2014). "The effect of interstitial pressure on therapeutic agent transport: Coupling with the tumor blood and lymphatic vascular systems". In: *Journal of Theoretical Biology* 355, pp. 194–207. arXiv: NIHMS150003. URL: http://dx.doi.org/10.1016/j.jtbi.2012.11.031.

Zhang, Lian and Zhi-Biao Wang (2010). "High-intensity focused ultrasound tumor ablation: Review of ten years of clinical experience". In: *Frontiers of Medicine in China* 4.3, pp. 294–302. URL: http://link.springer.com/10.1007/s11684-010-0092-8.

Zhou, Yu-Feng, Ali Syed Arbab, and Ronald Xiaorong Xu (2011). "High intensity focused ultrasound in clinical tumor ablation." In: *World journal of clinical oncology* 2.1, pp. 8–27. URL: http://dx.doi.org/10.5306/wjco.v2.i1.8http://www.pubmedcentral.nih.gov/articlerender.fcgi?artid=3095464{\&}tool=pmcentrez{\&}rendertype=abstract{\%}5Cnhttp://www.wjgnet.com/2218-4333/full/v2/i1/8.htm{\%}5Cnhttp://www.ncbi.nlm.nih.gov/pubmed/21603311{\%}5Cnhttp://www.pu.